UCLA
UCLA Electronic Theses and Dissertations

Title

Surface and Interface Engineering of Platinum Nanostructures for Effective Electrochemical Energy Conversion and Storage

Permalink

https://escholarship.org/uc/item/2qg2v8kx

Author

Wan, Chengzhang

Publication Date

2020

Peer reviewed|Thesis/dissertation

UNIVERSITY OF CALIFORNIA

Los Angeles

Surface and Interface Engineering of Platinum Nanostructures for

Effective Electrochemical Energy Conversion and Storage

A dissertation submitted

in partial satisfaction of the requirements for the degree

Doctor of Philosophy in Chemistry

by

Chengzhang Wan

2020

ABSTRACT OF THE DISSERTATION

Surface and Interface Engineering of Platinum Nanostructures for

Effective Electrochemical Energy Conversion and Storage

by

Chengzhang Wan

Doctor of Philosophy in Chemistry

University of California, Los Angeles, 2020

Professor Xiangfeng Duan, Chair

Electrochemical processes play a central role in clean energy generation, storage, and utilization. The rapid development of fuel cells that can efficiently convert chemical fuels to electricity will significantly reduce fossil fuel combustion to enable a sustainable future. Besides, water electrolysis is an essential environmentally friendly technique for the future hydrogen economy and vehicle market. The efficiency of these electrochemical processes relies on the rational design of high-performing electrocatalysts, which requires an atomic-level understanding of the charge/mass transfer and chemical transformation at the surface and interface of the electrocatalysts. The extent to which nanostructuring produces high performing surface and

interface for efficient energy transformation is likely to cover a wide range of metal/metal alloys, transition metal oxides, sulfides, and nitrides, and is currently the focus of intensive research. To date, noble metal platinum (Pt) has been proved to be the most active element to catalyze most of the electrochemical reactions required in the fuel cells and water electrolyzers. Due to the high cost of Pt and the high energy consumption resulted from the inevitable overpotential of those electrochemical reactions, optimizing the specific activity (SA), mass activity (MA), and the overpotential presents the key challenges for the design of commercial electrochemical catalysts. This requires the *systematic and controllable surface/interface engineering of the Pt catalysts for the rapid electron and mass transfer.*

The first part of my dissertation presents how the single-atom nickel-modified Pt nanowires (SANi-PtNWs) with abundant activated Pt sites next to the SANi and minimal blockage of the surface Pt sites can be synthesized using a partial electrochemical dealloying approach. This single atom tailoring strategy ensures the optimal combination of SA and ECSA to deliver the highest mass activity and durability for diverse electrochemical reactions. In the second part of the dissertation, we will introduce the direct synthesis of single-atom Rh tailored Pt nanowires (SARh-PtNWs) with optimum surface oxophilicity for the hydrogen oxidation reaction. The optimal surface oxophilicity on the SARh Pt nanowires surface ensures the optimum $OH_{ads}/H_2O\downarrow$ adsorption on the single-atom Rh sites at 0 V vs. RHE, which facilitates the removal of H_{ads} and hence accelerates the total hydrogen oxidation rate by over one magnitude compared to that of Pt. Apart from the single-atom tailoring strategy, in the third part, we will discuss a unique surface decoration of the Pt-tetrapod framework with water-permeable amorphous $Ni(OH)_2$ shell. Such decoration will keep the Pt sites covered from accessing the reactant such as water, proton, and hydroxyl, and thus can boost the MA and SA simultaneously.

The dissertation of Chengzhang Wan is approved.

Alexander Michael Spokoyny

Jeffrey I. Zink

William M. Gelbart

Xiangfeng Duan, Committee Chair

University of California, Los Angeles

2020

Dedicated to my family and friends near and far

for their unconditional love and support.

TABLE OF CONTENTS

LIST OF FIGURES

normalized HER Tafel-slope. (**E**) Comparison of ECSA (black arrow to the left), specific activities (normalized by ECSA, green arrow to the right) and mass activities (normalized by Pt mass, purple arrow to the right) for HER at -70 mV vs. RHE for all tested materials. (**F**) Comparison of HER mass activity of the SANi-PtNWs at -70 mV vs. RHE with the state-of-art values reported previously. * The material in Ref. 3 was tested in 0.1 M KOH. Error bars in e and f indicate the standard deviation of ten independent samples.

Figure 2.7. HER performance of the SANi-PtNWs and Pt/C under harsher conditions. (A) ECSA normalized HER LSVs for Pt/C and SANi-PtNWs in 4 M KOH with 95% iR-compensation at the scan rate of 5 mV/s. (B) ECSA normalized HER LSVs for Pt/C and SANi-PtNWs at 313 K and 333 K, respectively. The measurements were conducted in 1 M KOH with 95% iR-compensation at the scan rate of 5 mV/s.

Figure 2.8. HER chronopotentiometry test of SANi-PtNWs, in 1 M KOH at a constant current density of 5 A/mg$_{Pt}$.

Figure 2.9. Density functional theory (DFT) calculations of the active sites. (A) Cavity defect on the Pt (111) surface (Model A). The unit cell is 4×4, and the figure shows 2 unit cells. The locally stable adsorption sites for the H atom are labeled on the top view model. (B) Exchange current i$_0$ for HER as a function of *H adsorption free energy for the locally stable adsorption sites in Models A, B and C. (C) Adsorption free energy of hydrogen on model A Pt surface as a function of the applied potential U$_{RHE}$ at various coverage in pH=14 solution. (D) Model D for SANi decorated Pt (111) surface, Ni atom being in the surface layer. The unit cell is 3×3, and the figure shows 2 unit cells. (E) Volcano curve for adsorption sites on model D at low coverage (LC) and high coverage (HC) conditions. (F) Adsorption free energy of hydrogen on model D as a function of U$_{RHE}$ at various coverage at pH=14.

Figure 2.10. DFT models for HER activity calculation. To better distinguish the sites in Models A, C, E, and F, we use two letters to label the adsorption sites. The first letter indicates whether the site is top (T), bridge (B), FCC hollow (F) or HCP hollow (H), the second letter indicates whether the site is in a cavity (C), on the step (S), or on the terrace (T). For the adsorption sites in Models B, D and G, there are no cavities so we use simple labels to represent whether the site is top (T), bridge (B), FCC hollow (F) or HCP hollow

(H). The local minima sites are in red color. The adsorption free energies ($\Delta G_H - \Delta G_H^{Pt\ (111)}$) for all the adsorption sites are shown in Supplementary Table 3. Besides that, we also directly write the adsorption free energies on the adsorption sites. The local minima sites are in red color. (A) Model A with 4×4 unit cell and 5 layers. BS1 and BS2 are the most stable adsorption sites. By symmetry, there are 3 BS1 and 6 BS2 sites in one unit cell. Since they will be occupied first and they will block TS1, TS2 and FT1 sites, FT3 and TT1 sites will become the local minima sites. The TC site in the cavity is another local minimum. (B) Model B with 5×5 unit cell and 5 layers. Model C has a larger cavity than Model A, but there are many similarities. The BS sites are still the most stable sites. The TS sites have lower energies than TT3, FT2 and FT3, but they are blocked by the BS sites, so the local minima sites on the terrace are TT3, FT2, FT3 and FT4. The TC site in the cavity is still a local minimum site. (C) Model C of Pt (553) stepped surface. (D) Bond lengths (Å) in model C. The Pt-Pt distance in bulk is 2.81 Å. Model C is Pt (553) surface and it's a model for the step defect. We find the fcc hollow sites, such as F1, F2 and F3 are destabilized compared to Pt (111), which could be explained by the strain effect. In this figure, we can see that the bond lengths between the terrace atoms are about 3.5% less than the normal distance in the Pt bulk. (E) Model D with 3×3 unit cell and 5 layers. Model D is the (OH) bounded Ni single atoms decorated Pt (111) surface. B1 is the most preferred site, then T3, T2 and T1 sites will be covered if more H is adsorbed. Since all the other sites are blocked, T4 will be covered if one more H atom comes in although it's not a local minimum. If higher coverage is reached, the fcc sites and B2 site rather than the top sites will be covered. (F) SANi/Pt model with 3×3 unit cell and 5 layers. This model has no OH groups binding to the Ni, the fcc hollow sites F1 and F2 are the locally stable sites, and they are less active than Pt (111). (G) Model E with 4×4 unit cell and 5 layers. This is another model of Pt (111) with a cavity. (H) Model F with 5×5 unit cell and 5 layers. This is another model of Pt (111) with a cavity. (I) Model G with 3×3 unit cell and 5 layers. Model G is an isomer of model D, which is also (OH) bounded SANi decorated Pt (111) surface, it's 0.027 eV higher in energy. All the sites on this model are also more active than Pt (111).

LIST OF TABLES

ACKNOWLEDGMENTS

I would like to take the opportunity to appreciate those who have helped me go through this hard time during my graduate student career. Getting a Ph.D. is probably the hardest thing I will ever have to do. This journey is like a box of chocolate and you never know what is the next taste you are gonna get. This memory is full of happiness, frustration, pride, self-doubt, confidence, and all the emotions in-between. First of all, I would like to thank my advisor, Prof. Xiangfeng Duan, for his continuous guidance throughout the entirety of my Ph.D. career. I was impressed by his enthusiasm and curiosity in scientific research. His abundant knowledge and keen insight can always give me inspiration which eventually leads to the correct direction and the success of the projects. He will never overlook any details in the experiments. We have even benefited from the experimental details of the failure trials and developed a novel synthetic approach. Under his guidance, I have gradually built up my own philosophy of scientific research, and he will always be my academic role model. I would also thank Prof. Yu Huang for her guidance on my experiments. Although she is not my PI, she is always willing to share her knowledge with me when I encounter problems that are beyond my ability.

Moreover, I would like to express my appreciation to my fellows, other graduate and undergraduate students. Dr. Huilong Fei, who is now the Professor at Hunan University, used to be a postdoctoral when I attended this group. He is kind, patient, and knowledgeable, and always willing to share his valuable skills and knowledge with me. Dr. Zipeng Zhao and Dr. Mufan Li teach me the basic knowledge of material synthesis, characterization, and electrochemistry tests. Dr. Zhaoyang Lin teaches me how to do troubleshooting on many characterization techniques. I would also thank other fellows, Daniel Baumann, Jin Huang, Haotian Liu, Wang Xue, Boris Volosskiy, Yiliu Wang, Xinyao Lu, Yi Shen who are willing to listen to my questions and discuss

them with me no matter how busy they are. I would like to appreciate the valuable efforts of all the collaborators. I would specifically thank Dr. Kaining Duanmu from Prof. Philippe Sautet's group for their theory and computation works. Also, I would thank Dr. Mingjie Xu from Prof. Xiangqing Pan's group for all the characterizations of scanning transmission electron microscopy and thank Prof. Qingying Jia's group for their great efforts on *in-situ* X-ray absorption spectroscopy characterization.

I would greatly thank my best friend, Kaiyin Feng, for her encouragement and unconditional help when I was at the bottom of my life. I cannot go through those difficulties without her supports, especially when I do not want to let my parents realize that their son is struggling with his life thousands of miles away from home. Kaiying teaches me how to do the top-roping, in which I realize everyone in this world cannot always fight alone with themselves. In top-roping we need a belayer to ensure our safety, and we also need such a belayer in our life to support each other.

After fives years way from home, my parents are the people I miss most. I appreciate the advanced instant messaging technology which shrinks the distance between me and my family to a simple screen. I appreciate my parents' love and supports in the past five years. I wish they will stay happy healthy forever.

The distance between my hometown and Los Angeles is over 6500 miles, and the day when I will come home with my Doctoral degree is getting closer and closer. Thanks again to all the people I have met in this city, Los Angeles.

Previous Publications and Contributions of Co-Authors

Chapter 2 is a version of "single-atom tailoring of platinum nanocatalysts for high-performance multifunctional electrocatalysis". Prof. Xingfeng Duan, Prof. Yu Huang, and Prof. Phillippe Sautet supervised the project and designed the research. Dr. Mufan Li and I performed the synthesis, electrochemical tests, and characterizations. Dr. Kaining Duanmu performed the DFT calculations. Dr. Tao Cheng and Prof. William A. Goddard III performed the model simulations. Liang Zhang. and Wenxin Chen. performed XAS measurements and analysis. Prof. Jinghua Guo and Wenxin Chen provided expertise for XAS analysis. Dr. Sheng Dai and Prof. Xiaoqing Pan performed the EELS and HAADF-STEM measurements. Dr. Mufan Li and I co-wrote the paper. All authors discussed the results and commented on the manuscript. Published.

Nat Catal **2,** 495–503 (2019). https://doi.org/10.1038/s41929-019-0279-6

Author list: Mufan Li, Kaining Duanmu, **Chengzhang Wan**, Tao Cheng, Liang Zhang, Sheng Dai, Wenxin Chen, Zipeng Zhao, Peng Li, Huilong Fei, Yuanming Zhu, Rong Yu, Jun Luo, Ketao Zang, Zhaoyang Lin, Mengning Ding, Jin Huang, Hongtao Sun, Jinghua Guo, Xiaoqing Pan, William A. Goddard III, Philippe Sautet*, Yu Huang* & Xiangfeng Duan*

These authors contributed equally: Mufan Li, Kaining Duanmu, **Chengzhang Wan**, Tao Cheng.

Chapter 3 is a version of "Tailoring the Pt surface oxophilicity via single-atom Rh doping for boosting hydrogen oxidation reaction in alkaline electrolyte". Prof. Xiangfeng Duan and Yu Huang supervised the project. I designed the experiment and did the material synthesis, structure characterization, and electrochemistry evaluation. Prof. Xiaoqing Pan and Dr. Mingjie Xu did the STEM and EDS characterization. Prof. Qingying Jia did the XAS characterization. The manuscript

is in preparation. I wrote the manuscript. All authors discussed the results and commented on the manuscript.

Current author list: **Chengzhang Wan**, Mingjie Xu, Xiaoqing Pan, Qingying Jia, Yu Huang, Xiangfeng Duan.

Chapter 4 is a version of "Platinum Tetrapod with Proton Permeable Ni(OH)$_2$ Shell as Highly Active Hydrogen Evolution Electrocatalysts". Prof. Xiangfeng Duan and Yu Huang supervised the project. I designed the experiment and did material synthesis, structure characterization, and electrochemistry evaluation. Prof. Jun Luo, Prof. Xiaoqing Pan, and Dr. Mingjie Xu did the STEM and EDS characterization. The manuscript is in preparation. I wrote the manuscript. All authors discussed the results and commented on the manuscript.

Current author list: **Chengzhang Wan**, Mingjie Xu, Jun Luo, Xiaoqing Pan, Yu Huang, Xiangfeng Duan

Chapter 5 is a version of "Kinetic Control of the Anisotropic Growth of Pt nanocrystals". Prof. Xiangfeng Duan and Yu Huang supervised the project. I designed the experiment and did material synthesis, structure characterization, and electrochemistry evaluation. Prof. Jun Luo, Prof. Xiaoqing Pan, and Dr. Mingjie Xu did the STEM and EDS characterization. The manuscript is in preparation. I wrote the manuscript. All authors discussed the results and commented on the manuscript.

The manuscript is in preparation

Current author list: **Chengzhang Wan**, Mingjie Xu, Jun Luo, Xiaoqing Pan, Yu Huang, Xiangfeng Duan

VITA

2015	B.S. in Chemistry, Nanjing University, Nanjing
2017	Advancement to Candidacy, UCLA
2019	Dissertation Year Fellowship
2020	Jim and Barbara Tsay Dissertation Award

CHAPTER 1. INTRODUCTION AND BACKGROUND

1.1 A Broad View of Surface and Interface Engineering of Electrochemical Nano-Catalysts

Satisfying the increasing energy demand of our society while simultaneously fighting global environment pollution requires the technologies development of renewable energy generation, conversion, and storage. For example, as an alternative technology to enable the proposed sustainable clean energy future, fuel cells and water electrolytic cells that can efficiently conduct electrochemical reactions for electricity generation and energy storage with zero-emission are attracting increasing attention. However, the worldwide adoption and commercialization of these promising green technologies require the development of low cost, highly active, and durable electro-catalysts. However, the current state-of-the-art electrocatalysts are suffered from the low catalytic efficiency or the high cost of the device, because of the huge energy consumption on the large overpotential of these electrochemical reactions and the inevitable utilization of expensive noble metals. To address these challenges, considerable efforts have been devoted to investigating the reaction mechanisms and the fundamental structure-activity relationships, as well as the design and synthesis strategies to achieve high-performance electrocatalysts on both laboratory and industry production scale.

Typically, an electrochemical reaction is a heterogeneous process in which the charge transfer and chemical conversion take place at the surface and interface of the catalysts layer. At the nanoscale, the surfaces and interfaces of a material structure strongly influence its physical and chemical properties. For a given electrochemical reaction, according to the Sabatier principle, the surface of the optimized catalyst should provide optimum adsorption strength for all the reactants and intermediates that is neither too strong nor too weak.[1-3] Therefore, what is the origin of the

catalysts-adsorbate interaction strength and how to effectively tune the strength to the optimal level remain to be the most critical questions for the whole community. There are mainly two strategies to tune the binding strength of the adsorbate at the surface and interface, including 1) tuning the electronic structure of the catalysts and 2) changing the surface geometry and composition.[4-10] The effects of the two strategies are difficult to be distinguished because the change of surface geometry is always coupled with the change of electronic structure under nanoscale. Studies have shown that creating unique surface composition and topologies in nanostructures offer unprecedented performance in electrocatalysts.[11-13]
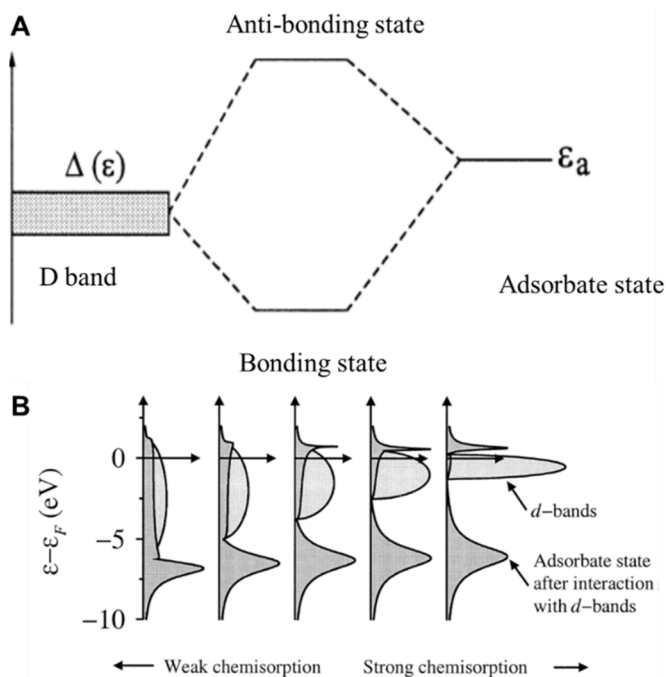
Figure 1.1. (A) Interaction between the D band of the metal and the adsorbate state results in the formation of a bonding state and an antibonding state. The discrepancy of electron filling in the two states determines the bonding strength. (B) Higher D band center leads to strong chemisorption and vice versa. Adapted from Ref 4.

For the first strategy, according to the D band theory, the adsorbates states will hybridize with the D band of the metal catalysts to form new bonding states (d-σ) and antibonding states (d-σ)*.[4] The strength of metal-adsorbate interaction depends on the difference in the filling of the bonding and antibonding states (**Figure 1.1A**). Usually, for the considered metal, the bonding states (d-σ) states are all full, thus, with more electrons in the antibonding states (d-σ)* the metal-adsorbate interaction will be weaker.[4]

d–DOS at surface site in unstrained surface

d–DOS at site in surface under tensile strain

$\varepsilon - \varepsilon_F$

ε_d

$\delta\varepsilon_d$

Rigid band model:

Band narrowing + shift to preserve the degree of *d*–filling
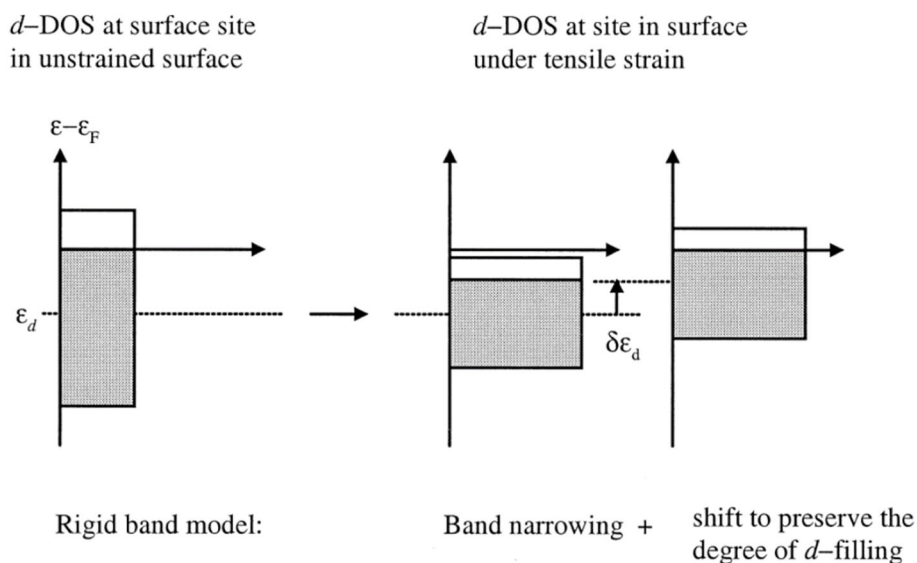
Figure 1.2. Illustration of the effect of tensile strain on the d band center. Increasing the lattice constant shrinks the bandwidth, and, to keep the number of d electrons fixed, the d states have to move up in energy. Adapted from Ref 4.

It has been revealed that the filling status of (d-σ)* is related to the position of the D band center of the metal catalysts. When the D band center moves up, due to the invariance of electrons in the D band, the D band will shrink and lift the antibonding state to a position higher than the Fermi level.[4] Thus, a higher D band center will cause a strong binding of the adsorbate and a lower D band center will cause a weaker binding of the adsorbate (**Figure 1.1B**). Studies have shown that by enhancing the compress strain of the Pt nanostructures, Pt-OH interaction can be weakened

to accelerate the whole oxygen reduction rate (**Figure 1.2**).[11,14,15] Detail of the strain effect and the application will be discussed in **Chapter 1.1**. It has been noticed that the position of the D band center on different Pt facets is also different, which partially explains the activity discrepancy of the identical electrochemical reactions under different Pt facets.[5]
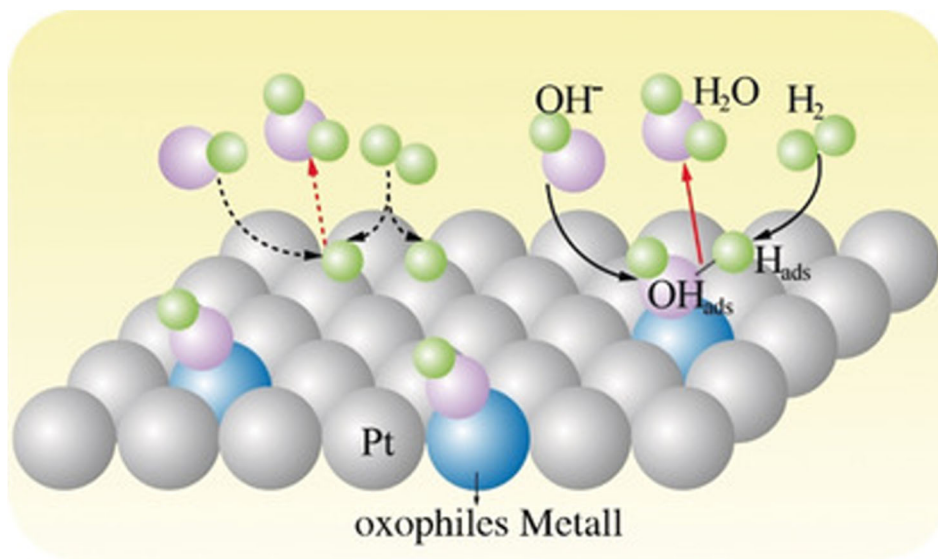
Figure 1.3. Illustration of the bifunctional mechanism where Pt is responsible for dissociative adsorption of the H_2 and oxophiles metal is responsible for adsorption of OH that can assist the further removal of H_{ads}. Adapted from Ref 16.

The composition tuning of the metal surface is based on the dual-site bifunctional mechanism, in which the major sites (Pt sites) work together with secondary promotor sites (oxophiles metal) to catalyze the whole reaction (**Figure 1.3**).[16] Such a strategy is effective in the case that the inappropriate adsorption strength of certain critical intermediates of the rate-determining step (rds) on the major catalytic sites dampers the whole reaction rate. Introducing the surface dopants helps to build up the sites/dopants interface to facilitate the adsorption/desorption of some key intermediates of the rds. This results in a boost of reaction activity and lower onset overpotential.[17-19]

Despite the extensive efforts and exciting developments on the surface and interface study, our poor understanding of the fundamental correlation between materials structure and electrochemical activities limits our ability to design, let alone predict, a new generation of high performing materials that can offer a paradigm shift in electrochemical technologies. My dissertation will center on the surface and interface engineering of Pt nanostructures to maximize its specific activity (SA) and mass activity (MA) for the desired reactions such as oxygen reduction reaction (ORR), hydrogen evolution reaction (HER), hydrogen oxidation reaction (HOR), alcohol oxidation reaction (AOR) in fuel cells and water electrolyzers.

1.2 Surface Engineering of Pt Nanocrystals

As a face-centered cubic (fcc) noble metal, Pt has three basic low index facets, including Pt(111), Pt(100), and Pt(110), together with high index surface Pt(hkl) (h $\geq$ k $\geq$ l $\geq$0) facets which should be consist of the three basic Pt crystal facets. It has been noticed for decades that the activity of the same reaction on different Pt facets is largely different, mainly due to the different electronic structure, coordination number, and surface energy.[20,21 22] The catalytic activity of different Pt facts has been extensively studied based on both single crystal electrode and nanoparticles with different shapes. In 1 M HClO$_4$, the ORR activity of Pt single-crystal electrode follows the trend Pt(110) $\geq$ Pt(111) $\geq$ Pt(100).[5] A similar trend is also observed on the pure Pt octahedra enclosed with {111} facets and Pt nanocubes enclosed with {100} facets. Activity for HOR/HER increases as Pt(111) < Pt(100) < Pt(110) according to Marković's reports.[20-22] The onset overpotential of methanol oxidation on Pt electrode increase in the order of Pt(100) < Pt(110) < Pt(111).[23] Besides the flat Pt surface, high index Pt facets with more step sites and low coordination number are found to be more active toward electrochemical reactions, compared with the low index surface.[12,24-26]

Therefore, the fabrication of Pt nanostructures with a rough surface is an efficient surface engineering strategy for enhancing the catalytic activity.
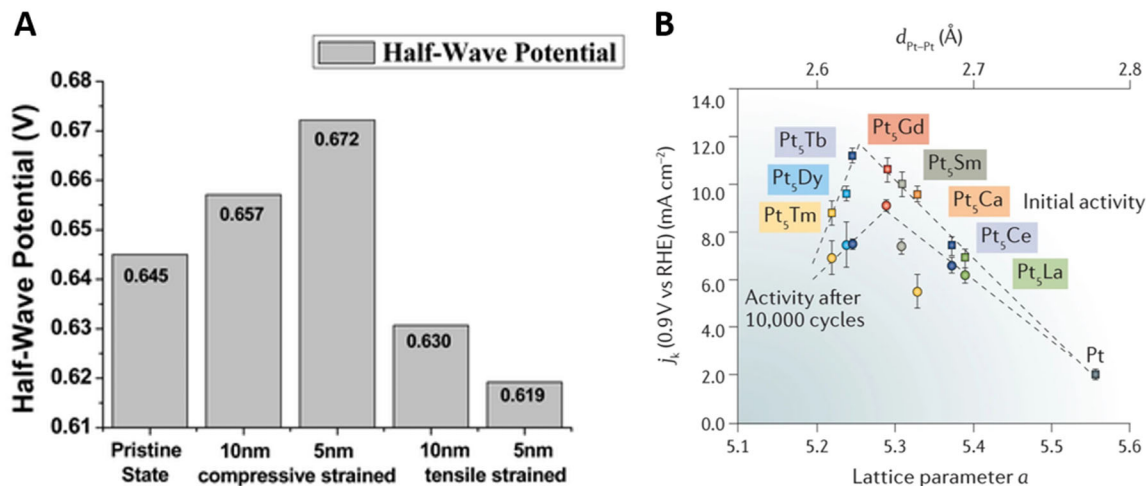
Figure 1.4. (A) Comparison of the ORR half-wave potential of 10 and 5 nm Pt nanofilm under different strain states. Compressively strained Pt exhibit higher ORR activity while tensilely strained Pt exhibit lower ORR activity compared with pristine state Pt. Adapted from Ref 27. (B) Volcano plot of ORR kinetics current vs. the lattice parameter. The ORR kinetic current reaches the top of the volcano plot with a lattice parameter and Pt-Pt distance between 5.2-5.3 Å and 2.6-2.65 Å, respectively. Adapted from Ref 28.

Moreover, the adsorption strength of the intermediate highly depends on the D band center of the Pt. It has been found that the compress strain of Pt lattice can lead to the more sufficient overlap of the D orbitals between the adjacent surface Pt sites and hence narrow the bandwidth and downshift the d-band center, while the tensile strain results in the upward shift of the D band center.[4] This provides a general strategy to finely tune the Pt D band center to achieve the desired metal-adsorbate interaction strength. Du *et al.* systemically investigated the structure-activity relationship for strained Pt nanofilms for ORR and exclusively concluded that the compress strain help to enhance the activity while the tensile strain decreases the activity (**Figure 1.4A**).[27] Chorkendorff *et al.* tuned the lattice parameter of Pt alloy using the lanthanide contraction and

found that the optimal lattice parameter of Pt alloy ORR catalyst falls into the range between 5.2-5.3 Å (**Figure 1.4B**).[28] It has also been reported that several atomic layers of Pt skin on top of the Pt$_3$Ni and PtPb sublayer have compress strain due to the existence of heteroatoms, leading to significantly enhanced ORR activity.[14,29]

1.3 Interface Engineering of Pt Crystals

In a heterogeneous electrochemical process, three interfaces have to be addressed, including the electrocatalysts-electrolyte interface, the inner boundary between the different components in the catalysts, the catalysts-substrate interface.[1] Rational engineering of these three interfaces can effectively enhance the catalytic activity by increasing the electrochemically active surface area (ECSA), facilitating the mass and the charge transfer efficiency throughout the catalyst layer, manipulating the alignment of surface electrolyte molecules, and introducing heteroatoms on the surface for syngenetic effect.[30-34] Typically, interface engineering of Pt-based catalysts including manipulating the interface between the Pt-metal, Pt-metal oxide (hydroxides) interface, Pt-carbon, Pt-dichalcogenide, and Pt-organic ligand (**Figure 1.5**).[1]
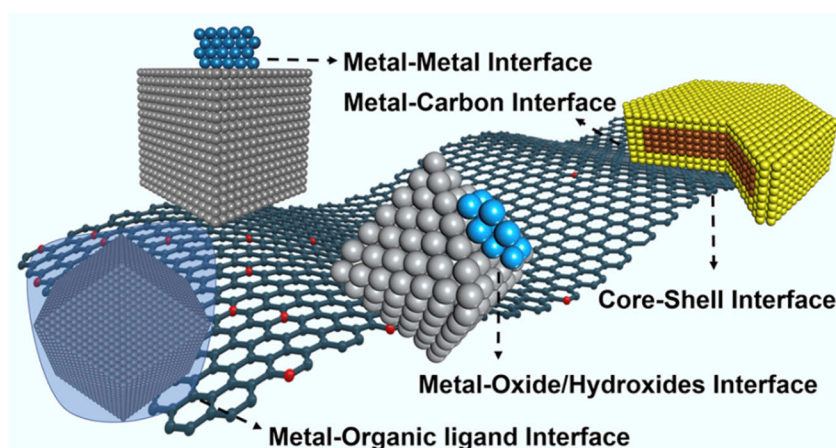
Figure 1.5. Illustration of different types of interface. Adapted from Ref 1.

1.3.1 Pt-Metal Interface Engineering

To date, tremendous multimetallic Pt-based electrocatalysts with a variety of dimensions, morphology, size, structures, and compositions have been developed. The interface between the Pt and other components is proved to have a vital role in increasing the catalytic activity towards multiple electrochemical reactions. The hetero-metal that interact with Pt has three functions, including 1) ligand effect that tuning the surface strain and electronic structure of Pt for intermediate adsorption/desorption, and 2) bifunctional mechanism in which the heteroatoms serve as the anchor sites for the adsorption/desorption of some specific intermediates, but the electronic structure of Pt is intact, and 3) sacrificial agent that dissolves faster and alleviate the dissolution of Pt during the reaction. To save the utilization of Pt, M@Pt core-shell structures with atomic Pt skin on the top of the heteroatom core have also attracted interest. Because of the lattice mismatch between the Pt and another metal at the interface, the surface strain on the Pt could be tuned to either tensile strain or compress strain by appropriately selecting the core element.[29,35-37] Another strategy to reduce the cost of Pt is to disperse Pt atoms in another metal is to prepare single-atom Pt dispersed metal surface.[38-40] The electronic structure of Pt atoms at the interface will be effectively influenced by the substrate atoms and thus the corresponding catalytic activity could be tuned.[40]

1.3.2 Pt-Metal Oxide(hydroxide) and Pt-Dichalcogenide Interface Engineering

Fabricating the Pt-metal oxide (hydroxides) interface is another efficient way to promote the activity of electrochemical catalysts, especially in the alkaline electrolyte where the transition metal oxides/hydroxides can survive, and the synergetic effect can last for a long duration. Pt nanostructures coupled with transition metal oxides/hydroxides could significantly improve the activity of HER/HOR in the alkaline condition due to the enhancement of the oxophilicity at the

interface of the Pt-metal oxides for a more efficient water dissociation step. [3,19,41] Nanostructures with Pt-metal oxides interface such as Pt-CeO$_2$, Pt-SnO$_2$, Pt-WO$_3$ composites, Pt nanowires physically mixed with Ni(OH)$_2$ flakes, Pt particles decorated on the Ni foam, NiO decorated Pt octahedra, have been successfully synthesized and applied to water splitting and alcohol oxidations. [8,18,42-45] Moreover, Pt single atoms were successfully immobilized on the metal oxides substrate to get single-atom Pt catalysts with 100% Pt utilization efficiency. [46,47] The strong Pt-O-metal interaction not only stabilized the single Pt atoms but also induce the charge transfer from Pt to the substrate to manipulate the electronic structure of center Pt atoms. Moreover, the Pt-dichalcogenide interface can further improve the catalytic activity. [47] Compared with PtNi nanowires, partially sulfurized Pt$_3$Ni/NiS nanowires possess abundant Pt-NiS interface where the NiS sites facilitate the HO-H dissociation faster than the Ni sites, and hence further enhance the HER activity. [48] Density functional theory (DFT) calculation suggested that single Pt atoms can stay on top of the S sites of the MoS$_2$ to form Pt-S interface which significantly improves the CO oxidation activity and the CO tolerance of Pt. [49] The existence of such interaction has then been confirmed by experimental chemists using aberration-corrected high-angle annular dark-field scanning transmission electron microscopy (AC-HAADF-STEM) and together with DFT calculation. [49,50]

1.3.3 Pt-Carbon Interface

The application of the electrocatalysts relies on the conductive carbon-based substrate to ensure efficient charge transfer and mass transfer at the surface and interface. Compared with Pt nanospheres, cubes, and octahedrons, the Pt nanowires have multi-contact point between themselves and the carbon black surface, thus has a higher resistance to the aggregation during the long-term tests. [12] Modifying carbon surface or functional groups can effectively change the

hydrophilicity of the carbon surface and hence affect the ion/gaseous transfer and charge transfer rate at the Pt-electrolyte-gas triple-phase.[51,52] The performance of Pt ORR catalysts is reported to be highly dependent on the type of the used carbon substrate.[53] It has been also reported that the nitrogen dopants in the reduced graphene oxides (rGO) interact with the Pt nanostructures to stabilize the catalysts.[54] Also, the carbon substrate can involve in the reaction process and have a synergetic effect. Fabricating PtCo-CoN$_4$C$_x$ interface help to achieve the highest ORR mass activity and high durability. The Pt sites can rapidly reduce the hydrogen peroxide generated by CoN$_4$C$_x$ sites, and hence activating the CoN$_4$C$_x$ sites which are intrinsically a 4 electrons pathway inhibited.[55]

1.3.4 Pt-Ligand Interaction

The electronic structure of the Pt surface can also be modified by simply decorating the surface with organic compounds. Pt ultrathin nanowires chelated with ethylenediamine (EDA) molecules have been reported to have high selectivity and activity for the production of N-hydroxylanilines.[56] Moreover, building up the Pt-ionic liquid interface can enhance the electrocatalytic activity due to the high gaseous solubility and high ion/charge transfer rate at the interface.[57]

1.4 Application of Pt Surface and Interface Engineering in the Electrocatalysis

Fuel cells and electrolytic cells that can efficiently conduct electrochemical reactions for energy conversion and storage with zero-emission are attracting increasing attention as an alternative technology to enable a sustainable clean energy future. Most of the commercialized fuel cells and electrolytic cells are based on proton exchange membrane (PEM), due to the well-developed PEM with high stability and its relatively low cost compared with the anion exchange membrane (AEM). However, PEM features a highly acidic solid electrolyte that challenges the stability of even the precious-metals-based electrocatalysts (*e.g.,* Pt), which requires the development of the anion exchange membrane and alkaline electrocatalysts. To date, Pt is still the best selection of the electrocatalysts toward anode reaction (HOR, AOR) and cathode reaction (ORR) in fuel cells and water electrolyzers in the aspect of activity and durability. However, the current state-of-art commercial Pt/C cannot stratify the DOE target for the commercialization of these techniques, and the surface/interface engineering is recognized as the most significant and effective strategy for developing electrocatalysts that far supersede the DOE target.1.4.1 Hydrogen Oxidation Reaction/Hydrogen Evolution Reaction.

The HER and HOR are the most fundamental and most important reactions in the water electrolyzer and fuel cell. The efficiency of HER has directly correlated with the competition between hydrogen fuel and fossil in the aspect of the price. And the overpotential of HOR is closely related to the output power of the fuel cells. The HER/HOR is a pair of reversible redox reactions. In acid, the reaction pathway of HER includes the following elementary steps: Volmer-Tafel or Volmer-Heyrovsky (**Figure 1.6**) and HOR follow the reverse reactions.[58] In the alkaline condition, because of the low abundance of H^+, the kinetic barrier for water dissociation has to be taken into consideration. The reaction pathway can be rewritten as (**Figure 1.6**).[58] Depends on which

elementary is the rds, HER/HOR has highly different Tafel slopes and kinetics expression.[58] In the acidic condition, due to the high abundance of H^+, the rate of the Volmer step is much higher than the rate of the Tafel step and hence the Tafel becomes the rds. The Tafel slope of HER/HOR that follows the Volmer-Tafel (rds) pathway in acid is calculated to be 30 mV/dec, which matches most of the experimentally observed Tafel slopes.[59,60] Therefore the reaction mechanism of HER of Pt in the acidic electrolyte is usually believed to be the Volmer-Tafel pathway. However, the HER/HOR that follow different pathways but are all under diffusion control usually shows the same Tafel slope. In the acidic conditions, because the HER/HOR reaction rate is rapid and the reaction is partially limited by the concentration and the mass transfer of H_2, therefore the HER/HOR polarization curve is highly overlapped with the diffusion-controlled polarization curve and hence it is difficult to distinguish whether the measured HER/HOR process is under Volmer-Tafel (rds) pathway or diffusion control. In the alkaline condition, the Volmer step is believed to be the rds due to the high kinetic barrier for HO-H dissociation.[61] Thus, the possible pathway in the alkaline condition is the Volmer (rds)-Tafel process with a Tafel slope of 118 mV/ dec. This matched perfectly with the experimental Tafel slope test on the single crystal crystalline Pt electrode.[20,58]

In acid

Volmer $\quad H^+ + e^- + * = H_{ad}$ $\qquad$ (1)

Tafel $\quad H_{ad} + H_{ad} = H_2 + 2*$ $\qquad$ (2)

Heyrovsky $\quad H_{ad} + H^+ + e^- = H_2 + *$ $\qquad$ (3)

In base

Volmer $\quad H_2O + e^- + * = H_{ad} + OH^-$ $\qquad$ (4)

Tafel $\quad H_{ad} + H_{ad} = H_2 + 2*$ $\qquad$ (5)

Heyrovsky $\quad H_{ad} + H_2O + e^- = H_2 + OH^- + *$ (6)
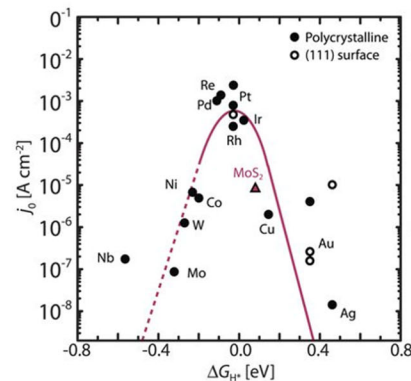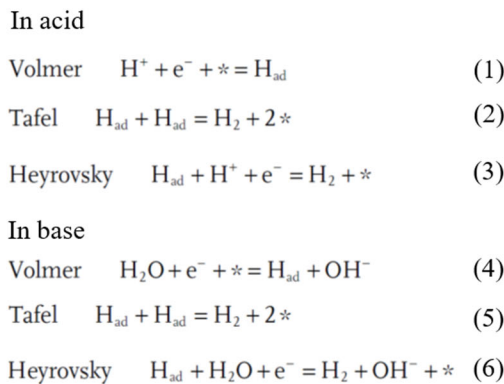
Figure 1.6. Reaction pathways of HER/HOR in acid and base. Adapted from Ref 58 (Left) and Volcano

plot of HOR/HER exchange current density vs. ΔG_{H*}. Pt exhibit the optimal adsorption energy of H^* Adapted from Ref 3.

To date, Pt is still the best HER/HOR active element in the natural world because of the optimal adsorption energy of H^* on its surface (**Figure 1.6**).[3] Both the adsorption and desorption of the key intermediate H^* are ultrafast on the Pt surface, especially in the acidic condition where protons are abundant. Nonetheless, in the acidic condition, precious metals are the only reliable catalysts for and ORR in fuel cells and OER in the water electrolyzer, yet still with significant overpotential. On the other hand, ORR and OER in the alkaline condition are much more favored even with non-precious metal (Ni, Fe, Co, etc.) and single-atom Fe-NC catalysts, which significantly saves the cost of catalysts from the oxygen side.[62,63] Moreover, the low-cost and durable anion exchange membrane (AEM) technique has also been rapidly developed in recent years, providing solid technical support for developing efficient AEM assembles.[64,65] Therefore, there is more motivation to conduct water electrolysis in the alkaline condition from ORR/OER and membrane perspective. However, the HER/HOR activity of Pt is highly pH-dependent and decreases over two orders of magnitude when pH increases from 1 to 14.[66] Thus, the sluggish HER/HOR reaction in the alkaline electrolyte becomes the most critical issue in developing AEMFCs and alkaline water electrolytic devices.
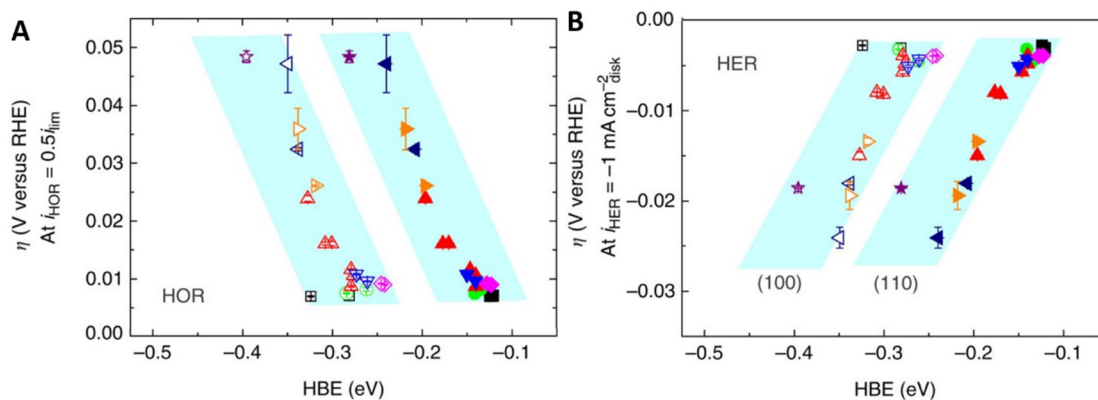
Figure 1.7. Correlating the hydrogen oxidation/evolution activity to the hydrogen binding energy renders a monotonic decreasing hydrogen oxidation/evolution activity with the hydrogen binding energy. Adapted from Ref 67.

The reasons for the discrepancy of HER/HOR activity in the acid and alkaline electrolyte are still under debate. Hydrogen binding energy (HBE) theory focuses on the surface binding energy of hydrogen. The monotonic correlation between the positive shift of the hydrogen desorption peaks and the increased pH, as well as between the decreased HER/HOR rate and the increased pH indicates that the HBE is the only parameter for governing the HER/HOR in full pH range (**Figure 1.7**).[67,68] Hence, the HBE of Pt in alkaline condition deviates from its optimal position, which results in a decreased HER/HOR activity. Durst *et al.* concluded that the reaction mechanism in both acid and base should be identical except in the base the Heyroveky and Volmer steps are followed by a rapid neutralization.[66,68] However, HBE theory fails to explain the questions that the HBE of Pt (111) does not shift as pH increases but still possesses a similar HER/HOR activity trend.[69] Also, the statement that high HBE slows down the oxidative desorption of H* to water on the HOR branch is reasonable. But on the HER branch, based on the energy diagram, it should mainly slow down the Tafel step and thus cannot explain that the Tafel slope changes from 30 mv/dec to 120 mv/dec from pH 1 to 13. It has been reported that fabricating the Ru@Pt and Ni@Pt core-shell structure with a clean Pt surface leads to the negative shift of the Hupd peak potential and the enhancement of the HER and HOR activity because of the compress strain formed at the interface weaken the Pt-H binding strength.[70,71] These results were used to be considered as the exclusive evidence for the HBE theory. However, some following studies suggested that the clean Pt surface may be doped with a trace amount of Ru during the atom rearrangement during the electrochemical CV test, thus these results cannot exclude the possibility

of a bifunctional mechanism in which the HBE is not the key descriptor that accounts for the activity drop.[72]
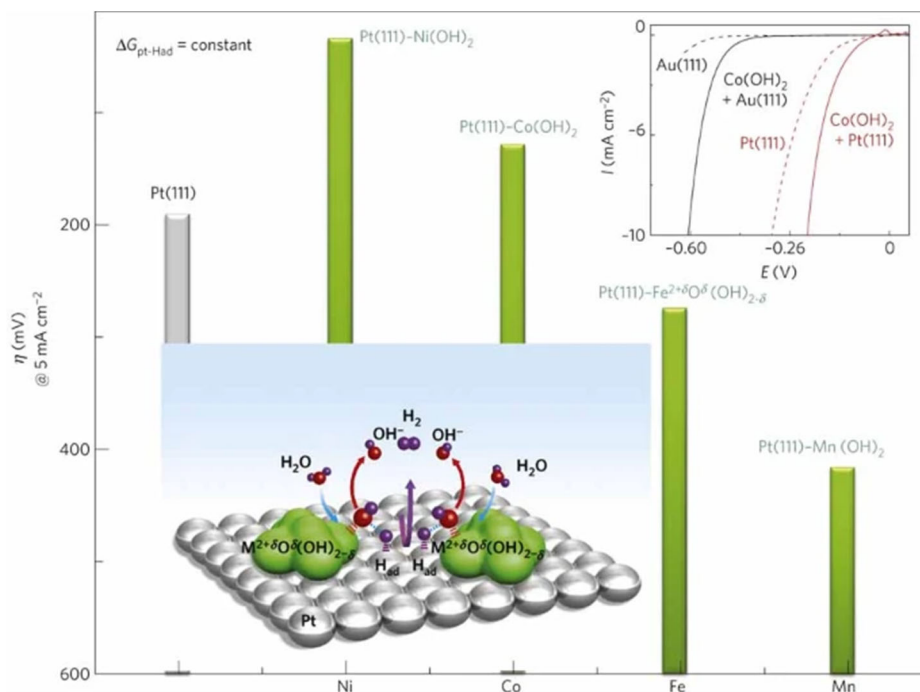
Figure 1.8. The trend of HER activity trend as a function of transitional metals. Adapted from Ref 25.

On the other hand, the bifunctional theory proposed that it is the activation barrier of water dissociation that accounts for the activity decrease. In the alkaline condition, the H_2O is required to dissociate to generate H^+ for H_{ads} in HER (Volmer step) and the OH^- for removal of H_{ads} from the Pt surface. Markovic reported a pioneer work that fabricates the Pt-transition metal hydroxides ($Ni(OH)_2$, $Co(OH)_2$, and $Fe(OH)_2$) interface on the Pt (111) polycrystalline electrode (**Figure 1.8**).[25] Pt electrode with $Ni(OH)_2$ on the surface enhances the HER activity by a factor of 7. They proposed that the water dissociation is significantly promoted at the interface where Ni sites are responsible for the adsorption of OH and Pt is responsible for the adsorption of H. Markov further explore the structure-activity relationship between the bonding strength of OH_{ad}-$M^{2+\delta}$ and concludes that only with optimal OH_{ad}-$M^{2+\delta}$ bonding strength will the HER reach the maximum

activity and the OH_{ad}-$M^{2+\delta}$ binding strength should be the universal descriptor for HER (**Figure 1.8**).[19] A similar conclusion was made by Jia's group on the HOR branch as well.[73] The existence of early existed OH_{ads} is also proved by a recent study by Jia's group.[74]
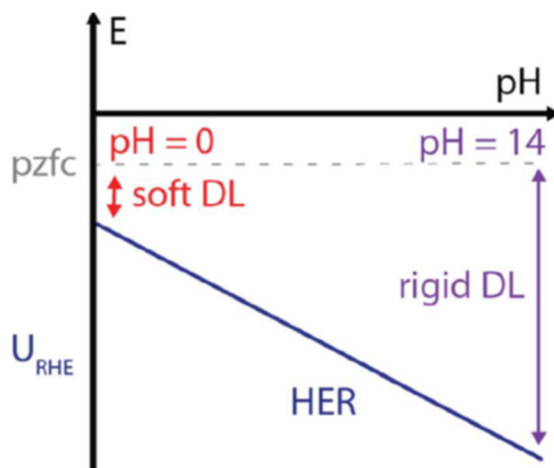
Figure 1.9. The PFZC moves to more positive potential vs. RHE leaving a more negative charged surface and a more rigid double layer. Adapted from Ref 75.

Another theory to explain the activity discrepancy is based on the potential of zero free charges (PZFC). The PZFC positively shifts by 59 mv/pH vs. RHE while increasing the pH value of electrolyte(**Figure 1.9**).[69,73,75] As PZFC shifts to a more positive value, the electrode surface is slightly negatively it becomes more difficult for OH_{ads}/$H_2O_\downarrow$ to adsorb on the Pt surface, which hinders H_2O dissociation in HER or the removal of H_{ads} in HOR.[73] With enhanced surface oxophilicity, the interaction between the O atoms in the OH/$H_2O_\downarrow$ and H_{ads} on the Pt surface facilitates the removal of the H_{ads} and thus accelerates the HOR rate. In the case of HER, the water dissociation is the rds in the alkaline condition. With higher surface oxophilicity, the OH/$H_2O_\downarrow$ will get readily adsorbed on the surface with the configuration that the O atom stays on the transition metal site and one H atom stays on the neighboring Pt site.[73] Such configuration weakens the H-OH bond and thus facilitates the water dissociation step and enhances the HER activity. Therefore,

the surface oxophilicity enhancement resulted from the surface decoration is vital for tuning the HER/HOR activity in the alkaline condition.[41]
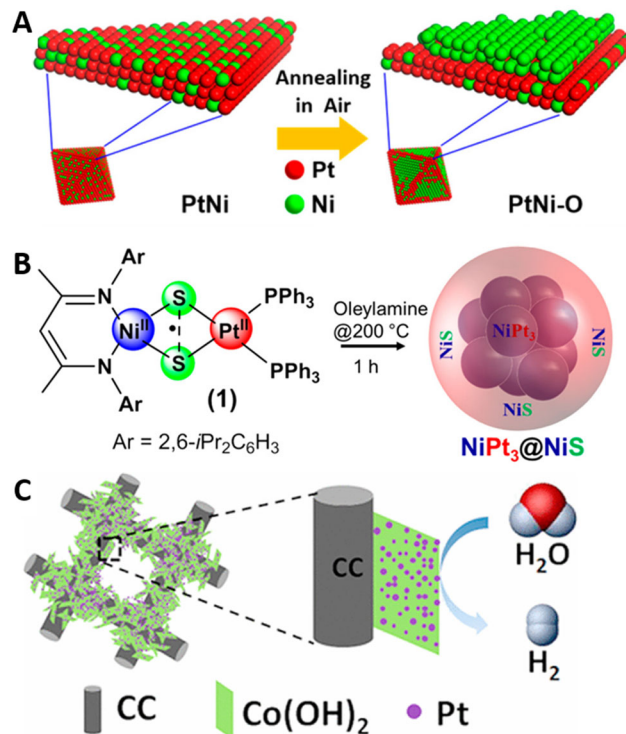
Figure 1.10. (A) Pt-NiO interface. Adapted from Ref 8. (B) NiPt-NiS interface. Adapted from Ref 80. (C) Pt-Co(OH)$_2$ interface. Adapted from Ref 81.

Based on the above theory, although some mechanisms details are under debate, it is well recognized that Pt surface and interface engineering is an effective strategy to enhance the HER/HOR activity. Pt (111) with Pt nanoisland decoration exhibit significantly higher HER/HOR activity compared with pristine Pt (111) because the step sites and edge sites preferred to adsorb OH compared with the flat surface.[76,77] PtNiO octahedra after annealing the PtNi octahedra in the air possesses higher HER than the PtNi (**Figure 1.10A**), further indicating that it is the Ni^{2+} rather than Ni that has the synergetic effect.[8] Highly strained Pt island on branched Ni nanoparticles exhibit weaker H bonding strength and thus boost the HER activity.[78] Pt nanostructures, such as

PtNi-S nanowires,[79] Pt$_3$Ni-NiS nanowires,[48] NiPt$_3$@NiS hetero-nanostructures (**Figure 1.10B**),[80] with Pt-NiS interface also shows enhanced HER activity compared with that of Pt and PtNi. Co(OH)$_2$@ Pt further enhances the activity and durability (**Figure 1.10C**).[81] Our group has developed a unique single-atom tailoring strategy to maximize the abundance of the Pt-Ni interface and achieve the highest HER activity so far.[82] In a step further, we developed Pt@Ni(OH)$_2$ core-shell structure with thick water/ion-permeable Ni(OH)$_2$ layer on the Pt tetrapods. Besides, we have developed single-atom Rh tailored Pt nanowires for efficient HOR. and we will discuss these projects in detail in **Chapter 2**.

1.4.2 Alcohol Oxidation

In addition to the alkaline HER/HOR, the activity of Pt catalysts for methanol oxidation reaction (MOR), which is the anode reaction in direct methanol fuel cells (DMFCs), is also found to be surface oxohilicity dependent. Using liquid methanol as the fuel, the DMFCs have attracted considerable attention due to the high-volume energy density of methanol (15.6 MJ/L) compared with hydrogen gas (5-5.6 MJ/L) and the ease in handling and storage.[83-86] However, MOR is significantly more difficult than HOR in hydrogen FCs.[31,87] Despite considerable efforts since the 1970s, the adoption of DMFC is still seriously limited by large overpotential (0.6 V vs. RHE) for MOR on the anode and the extremely low catalytic activity stability due to the poisoning by various intermediates such as CO.[88,89] To address the challenges, a better fundamental mechanistic understanding is necessary to identify the intermediates, products, rate-determining steps, and poisoning species during MOR on Pt surface;[89-97] and to develop catalysts by modifying Pt surface to achieve lower overpotential, higher activity, and better durability.[18,31,98-104]

$$Pt + H_2O \longrightarrow Pt\text{-}(OH)_{ads} + H_{aq}^+ + e^-$$

$$Pt + (CH_3OH)_{soln} \longrightarrow Pt\text{-}(CH_3OH)_{ads}$$

Indirect

$$Pt\text{-}(CH_3OH)_{ads} \longrightarrow Pt\text{-}(CO)_{ads} + H_{aq}^+ + e^-$$

$$Pt\text{-}(CO)_{ads} + Pt\text{-}(OH)_{ads} \longrightarrow Pt + Pt\text{-}(COOH)_{ads}$$

$$Pt + H_2O \longrightarrow Pt\text{-}(OH)_{ads} + H_{aq}^+ + e^-$$

Direct

$$Pt\text{-}(CH_3OH)_{ads} + Pt\text{-}(OH)_{ads} \longrightarrow Pt + CO_2 + H_{aq}^+ + e^-$$
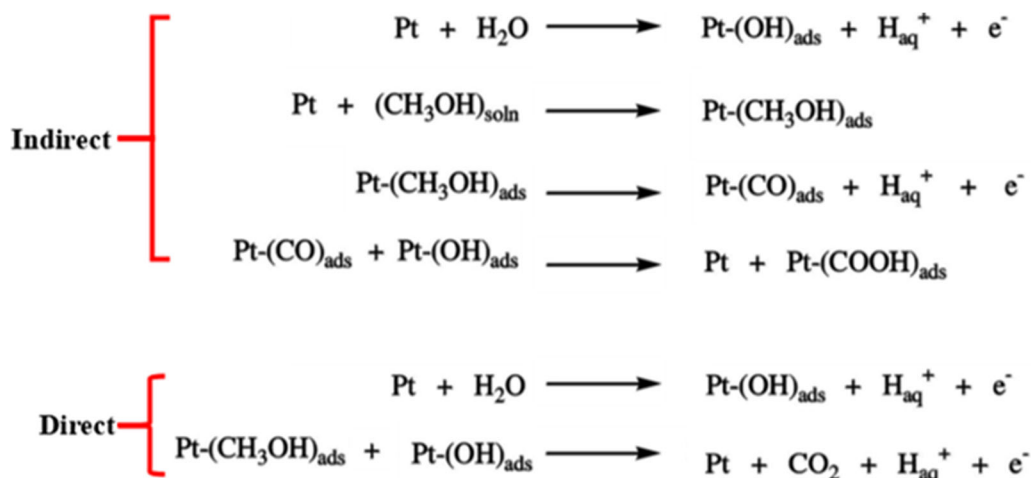
Figure 1.11. The two reaction pathways of MOR on the Pt surface, including the direct pathway and the indirect pathway. Both pathways require the Pt-OH to trigger on. Adapted from Ref 108.

Several reaction pathways have been proposed for MOR on Pt surface, owing to the recent development of in situ technologies (*e.g. in-situ* infrared spectroscopy (IR)[94,96,97,105,106] and differential electrochemical mass spectrometry technique (DEMS).[107] The proposed MOR pathways include **1)** the direct pathway in which the methanol is directly oxidized to formic acid and CO_2 under the help of Pt-OH,[87,108] and **2)** the indirect pathway in which the methanol is first dehydrogenated on Pt to be Pt-CO which then is further oxidized with the existence of Pt-OH (**Figure 1.11**).[87,108] **It is proposed that the oxophilicity of the Pt surface sets a limit on the minimum methanol oxidation overpotential and the activity.** Intrinsically Pt only starts to adsorb OH at potentials higher than 0.6 V vs RHE[5], therefore MOR will only be triggered after 0.6V.[87] Additionally, the resistance to CO poisoning in MOR also relies on the oxophilicity of the Pt catalyst surface.[109,110] ***Thus, modifying the oxophilicity of Pt surface to initiate the MOR at low overpotential offers a plausible pathway to overcoming the challenges of MOR.***
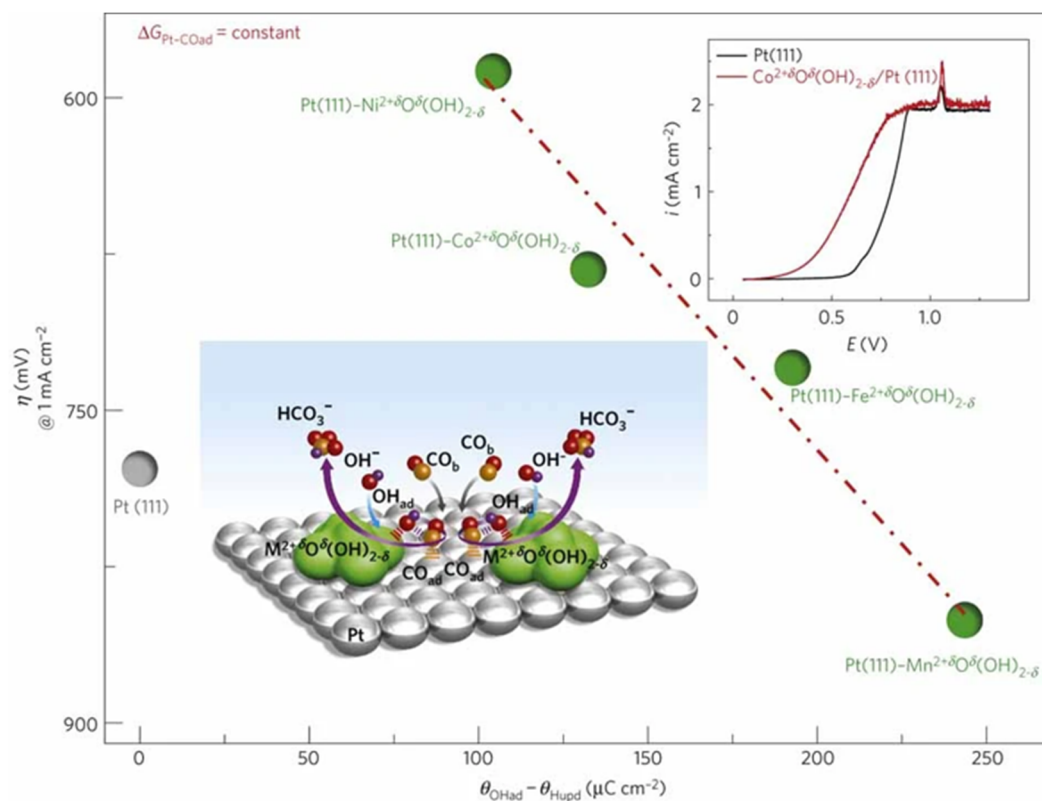
Figure 1.12. The trend in overpotential for CO oxidation is shown as a function of the 3d transition elements. Top inset: a comparison of the CO oxidation onset overpotential for Pt (111) and Co decorated Pt (111). Bottom inset: A schematic showing the L-H mechanism for CO oxidation. Adapted from Ref. 25.

For example, modifying Pt(111) electrode with transition metal hydroxides (*e.g.,* $Ni(OH)_2$ and $Co(OH)_2$) have been shown to greatly modify the OH adsorption/desorption and can **lower the overpotential** of CO oxidation by **more than 300 mV** (**Figure. 1.12**) when compared to undecorated Pt(111).[25] As illustrated in **Figure 1.12**, the adsorbed CO on Pt interacts with the transition metal hydroxide and get readily oxidized with the help of the OH adsorbed by transition metal with positive charge (OH_{ad}-$M^{2+\delta}$).[19] Inspired by this study, Pt/transition metal interfaces have been explored for MOR.[31,111-113] Huang *et al.* developed Pt-$Ni(OH)_2$-graphene ternary hybrid for highly durable MOR in alkaline conditions.[18] The $Ni(OH)_2$ facilitates the oxidative removal of the

carbonaceous poison on the adjacent Pt sites and the graphene ensures the efficient charge transfer. Sung *et al.* have designed and synthesis Pt-SnO$_2$-Rh ternary EOR catalysts with Pt for Ethanol adsorption and oxidation, Rh for C-C bond cleavage, and SnO$_2$ for oxidative removal of carbonaceous poison.[43] Apart from the interface of the Pt-metal oxide, Pt-metal interface in which the oxophilicity of the metal (usually precious metal) is higher than Pt can also enhance both the activity. PtRu, PtAg, and PtCu alloy possess much higher MOR activity and CO tolerance compared with Pt and can survive in the acidic condition.[89,98,112] Adding Cu to the PtNi has been reported to be an effective method to alleviate the dissolution of Ni and improve the stability of catalysts.[114,115]

Single crystal electrode studies have confirmed that the MOR performances in alkaline media follow the order of (100) < (110) < (111) on Pt and Pt (111) facet also has much less deactivation due to much less CO poisoning as demonstrated from in-situ FTIR.[23] {111} terminated PtRu nanowires exhibit much higher than the {100} terminated PtRu nanocubes.[116] For EOR on Pt single crystal electrode, Pt (111) also demonstrates optimized performance compared with Pt (110) and (111) single crystal electrodes as well as much higher selectivity for C1 pathway from in-situ FTIR.[117,118] This trend is further convinced for the Pt-based nanomaterials and Hu *et al.* reported ultrasmall Pt nanoparticles with precise control for the sizes and dominant-facets.

1.5 Overview of the Dissertation

In this dissertation, I will mainly focus on the surface/interface engineering of Pt nanocatalysts for three typical reactions, HER/HOR and MOR.

In **chapter 2**, I will introduce the single atom tailoring strategy for the synthesis of single-atom Ni tailored Pt nanowires (SANi-PtNWs). We use the electrochemical dealloying approach to

gradually remove the second metal (e.g. Ni) atoms from PtM alloy nanowires to produce SANi-nanowires. Characterizations such as high-resolution transmission electron microscopy (HRTEM), HAADF-STEM, Electron energy loss spectroscopy (EELs) inductively coupled plasma (ICP), extended X-ray absorption fine structure (EXAFS), *etc*. were used to determine the shape, surface morphology, composition, and atomic structure of the catalysts. Electrochemical tests combined with DFT calculations were performed to evaluate its HER and MOR activity and study the reaction mechanism behind.

In **chapter 3**, we will discuss our developed bottom-up direct synthesis methods that can control the coordination structure of surface heteroatom and prepared SARu-Pt NWs. Apart from the previous *ex-situ* characterization methods used in SANi nanowires, we use *in-situ* XAS to characterize the adsorbed OH or H_2O under the HOR regime to unravel the mechanism of exceptional high HOR activity of SARh-PtNWs, compared with both pure Pt surface, Rh-rich PtRh surface, and pure Rh surface.

In **chapter 4**. We will discuss the fabrication and application of the core-shell type Pt@Ni(OH)$_2$ framework for HER. The Ni(OH)$_2$ shell is found to be water and ion-permeable and will not block the Pt sites underneath the thick Ni(OH)$_2$ layer from accessing the electrolyte, thus this structure combines the high ECSA and high specific activity to deliver the highest mass activity that even surpass the SANi-Pt NWs. During the synthesis of this core-shell structure, We further developed a synthesis protocol that can tune the final shape of the product to be tetrahedra or octahedra via kinetic control.

1.5 Reference

1   Yang, Y., Luo, M., Zhang, W., Sun, Y., Chen, X. & Guo, S. Metal Surface and Interface Energy Electrocatalysis: Fundamentals, Performance Engineering, and Opportunities. *Chem* **4**, 2054-2083 (2018).

2   Nørskov, J. K., Bligaard, T., Rossmeisl, J. & Christensen, C. H. Towards the computational design of solid catalysts. *Nature Chemistry* **1**, 37-46 (2009).

3   Seh, Z. W., Kibsgaard, J., Dickens, C. F., Chorkendorff, I., Nørskov, J. K. & Jaramillo, T. F. Combining theory and experiment in electrocatalysis: Insights into materials design. *Science* **355**, eaad4998 (2017).

4   Hammer, B. & Nørskov, J. K. in *Advances in Catalysis* Vol. 45   71-129 (Academic Press, 2000).

5   Stamenkovic, V. R., Fowler, B., Mun, B. S., Wang, G., Ross, P. N., Lucas, C. A. & Marković, N. M. Improved oxygen reduction activity on Pt3Ni (111) via increased surface site availability. *Science* **315**, 493-497 (2007).

6   Jia, Q., Zhao, Z., Cao, L., Li, J., Ghoshal, S., Davies, V., Stavitski, E., Attenkofer, K., Liu, Z., Li, M., Duan, X., Mukerjee, S., Mueller, T. & Huang, Y. Roles of Mo Surface Dopants in Enhancing the ORR Performance of Octahedral PtNi Nanoparticles. *Nano Letters* **18**, 798-804 (2018).

7   Cui, C., Gan, L., Li, H.-H., Yu, S.-H., Heggen, M. & Strasser, P. Octahedral PtNi nanoparticle catalysts: exceptional oxygen reduction activity by tuning the alloy particle surface composition. *Nano letters* **12**, 5885-5889 (2012).

8   Zhao, Z., Liu, H., Gao, W., Xue, W., Liu, Z., Huang, J., Pan, X. & Huang, Y. Surface-engineered PtNi-O nanostructure with record-high performance for electrocatalytic hydrogen evolution reaction. *Journal of the American Chemical Society* **140**, 9046-9050 (2018).

9   Chattot, R. l., Asset, T., Bordet, P., Drnec, J., Dubau, L. & Maillard, F. d. r. Beyond Strain and Ligand Effects: Microstrain-Induced Enhancement of the Oxygen Reduction Reaction Kinetics on Various PtNi/C Nanostructures. *ACS Catalysis* **7**, 398-408 (2016).

10   Strasser, P., Koh, S., Anniyev, T., Greeley, J., More, K., Yu, C., Liu, Z., Kaya, S., Nordlund, D. & Ogasawara, H. Lattice-strain control of the activity in dealloyed core–shell fuel cell catalysts. *Nature chemistry* **2**, 454 (2010).

11   Huang, X., Zhao, Z., Cao, L., Chen, Y., Zhu, E., Lin, Z., Li, M., Yan, A., Zettl, A. & Wang, Y. M. High-performance transition metal–doped Pt3Ni octahedra for oxygen reduction reaction. *Science* **348**, 1230-1234 (2015).

12   Li, M., Zhao, Z., Cheng, T., Fortunelli, A., Chen, C.-Y., Yu, R., Zhang, Q., Gu, L., Merinov, B. V. & Lin, Z. Ultrafine jagged platinum nanowires enable ultrahigh mass activity for the oxygen reduction reaction. *Science* **354**, 1414-1419 (2016).

13   Mistry, H., Varela, A. S., Kühl, S., Strasser, P. & Cuenya, B. R. Nanostructured electrocatalysts with tunable activity and selectivity. *Nature Reviews Materials* **1**, 16009 (2016).

14   Bu, L., Zhang, N., Guo, S., Zhang, X., Li, J., Yao, J., Wu, T., Lu, G., Ma, J.-Y., Su, D. & Huang, X. Biaxially strained PtPb/Pt core/shell nanoplate boosts oxygen reduction catalysis. *Science* **354**, 1410 (2016).

15   Li, M., Zhao, Z., Cheng, T., Fortunelli, A., Chen, C.-Y., Yu, R., Zhang, Q., Gu, L., Merinov, B. V., Lin, Z., Zhu, E., Yu, T., Jia, Q., Guo, J., Zhang, L., Goddard III, W. A., Huang, Y. & Duan, X. Ultrafine jagged platinum nanowires enable ultrahigh mass activity for the oxygen reduction reaction. *Science* **354**, 1414-1419 (2016).

16   Li, J., Ghoshal, S., Bates, M. K., Miller, T. E., Davies, V., Stavitski, E., Attenkofer, K., Mukerjee, S., Ma, Z.-F. & Jia, Q. Experimental Proof of the Bifunctional Mechanism for the Hydrogen Oxidation in Alkaline Media. *Angewandte Chemie International Edition* **56**, 15594-15598 (2017).

17   Rebollar, L., Intikhab, S., Snyder, J. D. & Tang, M. H. Determining the Viability of Hydroxide-Mediated Bifunctional HER/HOR Mechanisms through Single-Crystal Voltammetry and Microkinetic Modeling. *Journal of The Electrochemical Society* **165**, J3209-J3221 (2018).

18   Huang, W., Wang, H., Zhou, J., Wang, J., Duchesne, P. N., Muir, D., Zhang, P., Han, N., Zhao, F., Zeng, M., Zhong, J., Jin, C., Li, Y., Lee, S.-T. & Dai, H. Highly active and durable methanol oxidation electrocatalyst based on the synergy of platinum–nickel hydroxide–graphene. *Nature communications* **6**, 10035 (2015).

19   Subbaraman, R., Tripkovic, D., Chang, K.-C., Strmcnik, D., Paulikas, A. P., Hirunsit, P., Chan, M., Greeley, J., Stamenkovic, V. & Markovic, N. M. Trends in activity for the water electrolyser reactions on 3d M(Ni,Co,Fe,Mn) hydr(oxy)oxide catalysts. *Nature Materials* **11**, 550 (2012).

20   Marković, N. M., Sarraf, S. T., Gasteiger, H. A. & Ross, P. N. Hydrogen electrochemistry on platinum low-index single-crystal surfaces in alkaline solution. *Journal of the Chemical Society, Faraday Transactions* **92**, 3719-3725 (1996).

21   Marković, N. M., Grgur, B. N. & Ross, P. N. Temperature-Dependent Hydrogen Electrochemistry on Platinum Low-Index Single-Crystal Surfaces in Acid Solutions. *The Journal of Physical Chemistry B* **101**, 5405-5413 (1997).

22   Hoshi, N., Asaumi, Y., Nakamura, M., Mikita, K. & Kajiwara, R. Structural Effects on the Hydrogen Oxidation Reaction on n(111)−(111) Surfaces of Platinum. *The Journal of Physical Chemistry C* **113**, 16843-16846 (2009).

23   Morallón, E., Rodes, A., Vázquez, J. L. & Pérez, J. M. Voltammetric and in-situ FTIR spectroscopic study of the oxidation of methanol on Pt(hkl) in alkaline media. *Journal of Electroanalytical Chemistry* **391**, 149-157 (1995).

24   Luo, M., Sun, Y., Zhang, X., Qin, Y., Li, M., Li, Y., Li, C., Yang, Y., Wang, L., Gao, P., Lu, G. & Guo, S. Stable High-Index Faceted Pt Skin on Zigzag-Like PtFe Nanowires Enhances Oxygen Reduction Catalysis. *Advanced Materials* **30**, 1705515 (2018).

25   Tian, N., Zhou, Z.-Y., Sun, S.-G., Ding, Y. & Wang, Z. L. Synthesis of Tetrahexahedral Platinum Nanocrystals with High-Index Facets and High Electro-Oxidation Activity. *Science* **316**, 732 (2007).

26   Xu, X., Zhang, X., Sun, H., Yang, Y., Dai, X., Gao, J., Li, X., Zhang, P., Wang, H.-H., Yu, N.-F. & Sun, S.-G. Synthesis of Pt–Ni Alloy Nanocrystals with High-Index Facets and Enhanced Electrocatalytic Properties. *Angewandte Chemie International Edition* **53**, 12522-12527 (2014).

27   Du, M., Cui, L., Cao, Y. & Bard, A. J. Mechanoelectrochemical Catalysis of the Effect of Elastic Strain on a Platinum Nanofilm for the ORR Exerted by a Shape Memory Alloy Substrate. *Journal of the American Chemical Society* **137**, 7397-7403 (2015).

28   Luo, M. & Guo, S. Strain-controlled electrocatalysis on multimetallic nanomaterials. *Nature Reviews Materials* **2**, 17059 (2017).

29   Chen, C., Kang, Y., Huo, Z., Zhu, Z., Huang, W., Xin, H. L., Snyder, J. D., Li, D., Herron, J. A., Mavrikakis, M., Chi, M., More, K. L., Li, Y., Markovic, N. M., Somorjai, G. A., Yang, P. & Stamenkovic, V. R. Highly Crystalline Multimetallic Nanoframes with Three-Dimensional Electrocatalytic Surfaces. *Science* **343**, 1339-1343 (2014).

30   Zhao, Z., Feng, M., Zhou, J., Liu, Z., Li, M., Fan, Z., Tsen, O., Miao, J., Duan, X. & Huang, Y. Composition tunable ternary Pt-Ni-Co octahedra for optimized oxygen reduction activity. *Chemical Communications* **52**, 11215-11218 (2016).

31   Antolini, E., Salgado, J. R. & Gonzalez, E. R. The methanol oxidation reaction on platinum alloys with the first row transition metals: the case of Pt–Co and–Ni alloy electrocatalysts for DMFCs: a short review. *Applied Catalysis B: Environmental* **63**, 137-149 (2006).

32   Zhang, L., Roling, L. T., Wang, X., Vara, M., Chi, M., Liu, J., Choi, S.-I., Park, J., Herron, J. A., Xie, Z., Mavrikakis, M. & Xia, Y. Platinum-based nanocages with subnanometer-thick walls and well-defined, controllable facets. *Science* **349**, 412-416 (2015).

33   Du, R., Jin, W., Hübner, R., Zhou, L., Hu, Y. & Eychmüller, A. Engineering Multimetallic Aerogels for pH-Universal HER and ORR Electrocatalysis. *Advanced Energy Materials* **10**, 1903857 (2020).

34   Cai, B. & Eychmüller, A. Promoting Electrocatalysis upon Aerogels. *Advanced Materials* **31**, 1804881 (2019).

35   van der Vliet, D. F., Wang, C., Li, D., Paulikas, A. P., Greeley, J., Rankin, R. B., Strmcnik, D., Tripkovic, D., Markovic, N. M. & Stamenkovic, V. R. Unique Electrochemical Adsorption Properties of Pt-Skin Surfaces. *Angewandte Chemie* **124**, 3193-3196 (2012).

36   Zhang, B.-W., Lai, W.-H., Sheng, T., Qu, X.-M., Wang, Y.-X., Ren, L., Zhang, L., Du, Y., Jiang, Y.-X., Sun, S.-G. & Dou, S.-X. Ordered platinum–bismuth intermetallic clusters with Pt-skin for a highly efficient electrochemical ethanol oxidation reaction. *Journal of Materials Chemistry A* **7**, 5214-5220 (2019).

37   Xia, Z. & Guo, S. Strain engineering of metal-based nanomaterials for energy electrocatalysis. *Chemical Society Reviews* **48**, 3265-3278 (2019).

38   Yang, S., Kim, J., Tak, Y. J., Soon, A. & Lee, H. Single-Atom Catalyst of Platinum Supported on Titanium Nitride for Selective Electrochemical Reactions. *Angewandte Chemie International Edition* **55**, 2058-2062 (2016).

39   Kim, J., Roh, C.-W., Sahoo, S. K., Yang, S., Bae, J., Han, J. W. & Lee, H. Highly Durable Platinum Single-Atom Alloy Catalyst for Electrochemical Reactions. *Advanced Energy Materials* **8**, 1701476 (2018).

40   Duchesne, P. N., Li, Z. Y., Deming, C. P., Fung, V., Zhao, X., Yuan, J., Regier, T., Aldalbahi, A., Almarhoon, Z., Chen, S., Jiang, D.-e., Zheng, N. & Zhang, P. Golden single-atomic-site platinum electrocatalysts. *Nature Materials* **17**, 1033-1039 (2018).

41   Ramaswamy, N., Ghoshal, S., Bates, M. K., Jia, Q., Li, J. & Mukerjee, S. Hydrogen oxidation reaction in alkaline media: Relationship between electrocatalysis and electrochemical double-layer structure. *Nano Energy* **41**, 765-771 (2017).

42   Xu, C. & Shen, P. K. Electrochamical oxidation of ethanol on Pt-CeO2/C catalysts. *Journal of Power Sources* **142**, 27-29 (2005).

43   Kowal, A., Gojković, S. L., Lee, K. S., Olszewski, P. & Sung, Y. E. Synthesis, characterization and electrocatalytic activity for ethanol oxidation of carbon supported Pt, Pt–Rh, Pt–SnO2 and Pt–Rh–SnO2 nanoclusters. *Electrochemistry Communications* **11**, 724-727 (2009).

44   Xie, C., Chen, W., Du, S., Yan, D., Zhang, Y., Chen, J., Liu, B. & Wang, S. In-situ phase transition of WO3 boosting electron and hydrogen transfer for enhancing hydrogen evolution on Pt. *Nano Energy* **71**, 104653 (2020).

45   Fiameni, S., Herraiz-Cardona, I., Musiani, M., Pérez-Herranz, V., Vázquez-Gómez, L. & Verlato, E. The HER in alkaline media on Pt-modified three-dimensional Ni cathodes. *International Journal of Hydrogen Energy* **37**, 10507-10516 (2012).

46   Qiao, B., Wang, A., Yang, X., Allard, L. F., Jiang, Z., Cui, Y., Liu, J., Li, J. & Zhang, T. Single-atom catalysis of CO oxidation using Pt1/FeOx. *Nature Chemistry* **3**, 634-641 (2011).

47   Xu, Y., Chu, M., Liu, F., Wang, X., Liu, Y., Cao, M., Gong, J., Luo, J., Lin, H., Li, Y. & Zhang, Q. Revealing the Correlation between Catalytic Selectivity and the Local Coordination Environment of Pt Single Atom. *Nano Letters* **20**, 6865-6872 (2020).

48   Wang, P., Zhang, X., Zhang, J., Wan, S., Guo, S., Lu, G., Yao, J. & Huang, X. Precise tuning in platinum-nickel/nickel sulfide interface nanowires for synergistic hydrogen evolution catalysis. *Nat Commun* **8**, 14580 (2017).

49   Du, C., Lin, H., Lin, B., Ma, Z., Hou, T., Tang, J. & Li, Y. MoS2 supported single platinum atoms and their superior catalytic activity for CO oxidation: a density functional theory study. *Journal of Materials Chemistry A* **3**, 23113-23119 (2015).

50   Li, X., Lee, J. K., Lu, Y., Gerkman, M. A., Kengmana, E. S., Fonseca, M. V., Warner, J. H. & Han, G. G. D. Precursor Design for High Density Single Pt Atom Sites on MoS2: Enhanced Stability at Elevated Temperatures and Reduced 3D Clustering. *Chemistry of Materials* **32**, 2541-2551 (2020).

51   O'Hayre, R. & Prinz, F. B. The Air/Platinum/Nafion Triple-Phase Boundary: Characteristics, Scaling, and Implications for Fuel Cells. *Journal of The Electrochemical Society* **151**, A756 (2004).

52   O'Hayre, R., Barnett, D. M. & Prinz, F. B. The Triple Phase Boundary. *Journal of The Electrochemical Society* **152**, A439 (2005).

53   Liu, M., Zhao, Z., Duan, X. & Huang, Y. Nanoscale Structure Design for High-Performance Pt-Based ORR Catalysts. *Advanced Materials* **31**, 1802234 (2019).

54   Li, Z., Gao, Q., Zhang, H., Tian, W., Tan, Y., Qian, W. & Liu, Z. Low content Pt nanoparticles anchored on N-doped reduced graphene oxide with high and stable electrocatalytic activity for oxygen reduction reaction. *Scientific Reports* **7**, 43352 (2017).

55   Chong, L., Wen, J., Kubal, J., Sen, F. G., Zou, J., Greeley, J., Chan, M., Barkholtz, H., Ding, W. & Liu, D.-J. Ultralow-loading platinum-cobalt fuel cell catalysts derived from imidazolate frameworks. *Science* **362**, 1276 (2018).

56   Chen, G., Xu, C., Huang, X., Ye, J., Gu, L., Li, G., Tang, Z., Wu, B., Yang, H., Zhao, Z., Zhou, Z., Fu, G. & Zheng, N. Interfacial electronic effects control the reaction selectivity of platinum catalysts. *Nature Materials* **15**, 564-569 (2016).

57   Snyder, J., Fujita, T., Chen, M. W. & Erlebacher, J. Oxygen reduction in nanoporous metal–ionic liquid composite electrocatalysts. *Nature Materials* **9**, 904-907 (2010).

58   Tian, X., Zhao, P. & Sheng, W. Hydrogen Evolution and Oxidation: Mechanistic Studies and Material Advances. *Advanced Materials* **31**, 1808066 (2019).

59   Zhang, T. & Anderson, A. B. Hydrogen Oxidation and Evolution on Platinum Electrodes in Base: Theoretical Study. *The Journal of Physical Chemistry C* **111**, 8644-8648 (2007).

60   Shinagawa, T., Garcia-Esparza, A. T. & Takanabe, K. Insight on Tafel slopes from a microkinetic analysis of aqueous electrocatalysis for energy conversion. *Scientific Reports* **5**, 13801 (2015).

61   Lamoureux, P. S., Singh, A. R. & Chan, K. pH Effects on Hydrogen Evolution and Oxidation over Pt(111): Insights from First-Principles. *ACS Catalysis* **9**, 6194-6201 (2019).

62   Song, J., Wei, C., Huang, Z.-F., Liu, C., Zeng, L., Wang, X. & Xu, Z. J. A review on fundamentals for designing oxygen evolution electrocatalysts. *Chemical Society Reviews* **49**, 2196-2214 (2020).

63   Wan, C., Duan, X. & Huang, Y. Molecular Design of Single-Atom Catalysts for Oxygen Reduction Reaction. *Advanced Energy Materials* **10**, 1903815 (2020).

64   Leng, Y., Chen, G., Mendoza, A. J., Tighe, T. B., Hickner, M. A. & Wang, C.-Y. Solid-State Water Electrolysis with an Alkaline Membrane. *Journal of the American Chemical Society* **134**, 9054-9057 (2012).

65   Abbasi, R., Setzler, B. P., Lin, S., Wang, J., Zhao, Y., Xu, H., Pivovar, B., Tian, B., Chen, X., Wu, G. & Yan, Y. A Roadmap to Low-Cost Hydrogen with Hydroxide Exchange Membrane Electrolyzers. *Advanced Materials* **0**, 1805876 (2019).

66   Durst, J., Siebel, A., Simon, C., Hasché, F., Herranz, J. & Gasteiger, H. A. New insights into the electrochemical hydrogen oxidation and evolution reaction mechanism. *Energy & Environmental Science* **7**, 2255-2260 (2014).

67   Sheng, W., Zhuang, Z., Gao, M., Zheng, J., Chen, J. G. & Yan, Y. Correlating hydrogen oxidation and evolution activity on platinum at different pH with measured hydrogen binding energy. *Nature Communications* **6**, 5848 (2015).

68   Jia, Q., Liu, E., Jiao, L., Li, J. & Mukerjee, S. Current understandings of the sluggish kinetics of the hydrogen evolution and oxidation reactions in base. *Current Opinion in Electrochemistry* **12**, 209-217 (2018).

69   Ledezma-Yanez, I., Wallace, W. D. Z., Sebastián-Pascual, P., Climent, V., Feliu, J. M. & Koper, M. T. M. Interfacial water reorganization as a pH-dependent descriptor of the hydrogen evolution rate on platinum electrodes. *Nature Energy* **2**, 17031 (2017).

70   Lu, S. & Zhuang, Z. Investigating the Influences of the Adsorbed Species on Catalytic Activity for Hydrogen Oxidation Reaction in Alkaline Electrolyte. *Journal of the American Chemical Society* **139**, 5156-5163 (2017).

71   Elbert, K., Hu, J., Ma, Z., Zhang, Y., Chen, G., An, W., Liu, P., Isaacs, H. S., Adzic, R. R. & Wang, J. X. Elucidating Hydrogen Oxidation/Evolution Kinetics in Base and Acid by Enhanced Activities at the Optimized Pt Shell Thickness on the Ru Core. *ACS Catalysis* **5**, 6764-6772 (2015).

72   Han, B. C., Van der Ven, A., Ceder, G. & Hwang, B.-J. Surface segregation and ordering of alloy surfaces in the presence of adsorbates. *Physical Review B* **72**, 205409 (2005).

73   Liu, E., Jiao, L., Li, J., Stracensky, T., Sun, Q., Mukerjee, S. & Jia, Q. Interfacial water shuffling the intermediates of hydrogen oxidation and evolution reactions in aqueous media. *Energy & Environmental Science* **13**, 3064-3074 (2020).

74   Jiao, L., Liu, E., Mukerjee, S. & Jia, Q. In Situ Identification of Non-Specific Adsorption of Alkali Metal Cations on Pt Surfaces and Their Catalytic Roles in Alkaline Solutions. *ACS Catalysis* **10**, 11099-11109 (2020).

75   Dubouis, N. & Grimaud, A. The hydrogen evolution reaction: from material to interfacial descriptors. *Chemical Science* **10**, 9165-9181 (2019).

76   Subbaraman, R., Tripkovic, D., Strmcnik, D., Chang, K.-C., Uchimura, M., Paulikas, A. P., Stamenkovic, V. & Markovic, N. M. Enhancing hydrogen evolution activity in water splitting by tailoring Li+-Ni (OH) 2-Pt interfaces. *Science* **334**, 1256-1260 (2011).

77   Strmcnik, D., Uchimura, M., Wang, C., Subbaraman, R., Danilovic, N., van der Vliet, D., Paulikas, A. P., Stamenkovic, V. R. & Markovic, N. M. Improving the hydrogen oxidation reaction rate by promotion of hydroxyl adsorption. *Nature Chemistry* **5**, 300-306 (2013).

78   Alinezhad, A., Gloag, L., Benedetti, T. M., Cheong, S., Webster, R. F., Roelsgaard, M., Iversen, B. B., Schuhmann, W., Gooding, J. J. & Tilley, R. D. Direct Growth of Highly Strained Pt Islands on Branched Ni Nanoparticles for Improved Hydrogen Evolution Reaction Activity. *Journal of the American Chemical Society* **141**, 16202-16207 (2019).

79   Liu, Z., Qi, J., Liu, M., Zhang, S., Fan, Q., Liu, H., Liu, K., Zheng, H., Yin, Y. & Gao, C. Aqueous Synthesis of Ultrathin Platinum/Non-Noble Metal Alloy Nanowires for Enhanced Hydrogen Evolution Activity. *Angewandte Chemie* **130**, 11852-11856 (2018).

80   Panda, C., Menezes, P. W., Yao, S., Schmidt, J., Walter, C., Hausmann, J. N. & Driess, M. Boosting Electrocatalytic Hydrogen Evolution Activity with a NiPt3@NiS Heteronanostructure Evolved from a Molecular Nickel–Platinum Precursor. *Journal of the American Chemical Society* **141**, 13306-13310 (2019).

81   Xing, Z., Han, C., Wang, D., Li, Q. & Yang, X. Ultrafine Pt Nanoparticle-Decorated Co(OH)2 Nanosheet Arrays with Enhanced Catalytic Activity toward Hydrogen Evolution. *ACS Catalysis* **7**, 7131-7135 (2017).

82   Li, M., Duanmu, K., Wan, C., Cheng, T., Zhang, L., Dai, S., Chen, W., Zhao, Z., Li, P., Fei, H., Zhu, Y., Yu, R., Luo, J., Zang, K., Lin, Z., Ding, M., Huang, J., Sun, H., Guo, J., Pan, X., Goddard, W. A., Sautet, P., Huang, Y. & Duan, X. Single-atom tailoring of platinum nanocatalysts for high-performance multifunctional electrocatalysis. *Nature Catalysis* **2**, 495-503 (2019).

83   Olah, G. A. Beyond oil and gas: the methanol economy. *Angewandte Chemie International Edition* **44**, 2636-2639 (2005).

84   Gumber, S. & Gurumoorthy, A. V. in *Methanol*   661-674 (Elsevier, 2017).

85   Apanel, G. & Johnson, E. Direct methanol fuel cells–ready to go commercial? *Fuel Cells Bulletin* **2004**, 12-17 (2004).

86   Aricò, A. S., Baglio, V. & Antonucci, V. Direct methanol fuel cells: history, status and perspectives. *Electrocatalysis of direct methanol fuel cells*, 1-78 (2009).

87   Iwasita, T. Electrocatalysis of methanol oxidation. *Electrochimica Acta* **47**, 3663-3674 (2002).

88   Chen, D. J. & Tong, Y. J. Irrelevance of carbon monoxide poisoning in the methanol oxidation reaction on a PtRu electrocatalyst. *Angewandte Chemie International Edition* **54**, 9394-9398 (2015).

89   Seiler, T., Savinova, E., Friedrich, K. & Stimming, U. Poisoning of PtRu/C catalysts in the anode of a direct methanol fuel cell: a DEMS study. *Electrochimica Acta* **49**, 3927-3936 (2004).

90   Zhao, Y., Li, X., Schechter, J. M. & Yang, Y. Revisiting the oxidation peak in the cathodic scan of the cyclic voltammogram of alcohol oxidation on noble metal electrodes. *RSC Advances* **6**, 5384-5390 (2016).

91   Neurock, M., Janik, M. & Wieckowski, A. A first principles comparison of the mechanism and site requirements for the electrocatalytic oxidation of methanol and formic acid over Pt. *Faraday discussions* **140**, 363-378 (2009).

92   Yu, E. H., Scott, K. & Reeve, R. W. A study of the anodic oxidation of methanol on Pt in alkaline solutions. *Journal of Electroanalytical Chemistry* **547**, 17-24 (2003).

93   Marković, N. M., Gasteiger, H. A., Ross Jr, P. N., Jiang, X., Villegas, I. & Weaver, M. J. Electro-oxidation mechanisms of methanol and formic acid on Pt-Ru alloy surfaces. *Electrochimica acta* **40**, 91-98 (1995).

94   Yajima, T., Uchida, H. & Watanabe, M. In-situ ATR-FTIR spectroscopic study of electro-oxidation of methanol and adsorbed CO at Pt− Ru alloy. *The Journal of Physical Chemistry B* **108**, 2654-2659 (2004).

95   Hofstead-Duffy, A. M., Chen, D.-J., Sun, S.-G. & Tong, Y. J. Origin of the current peak of negative scan in the cyclic voltammetry of methanol electro-oxidation on Pt-based electrocatalysts: a revisit to the current ratio criterion. *Journal of Materials Chemistry* **22**, 5205-5208 (2012).

96   Liu, S. X., Liao, L. W., Tao, Q., Chen, Y. X. & Ye, S. The kinetics of CO pathway in methanol oxidation at Pt electrodes, a quantitative study by ATR-FTIR spectroscopy. *Physical Chemistry Chemical Physics* **13**, 9725-9735 (2011).

97   Chen, Y. X., Miki, A., Ye, S., Sakai, H. & Osawa, M. Formate, an active intermediate for direct oxidation of methanol on Pt electrode. *Journal of the American Chemical Society* **125**, 3680-3681 (2003).

98   Feng, Y.-Y., Bi, L.-X., Liu, Z.-H., Kong, D.-S. & Yu, Z.-Y. Significantly enhanced electrocatalytic activity for methanol electro-oxidation on Ag oxide-promoted PtAg/C catalysts in alkaline electrolyte. *Journal of catalysis* **290**, 18-25 (2012).

99   Fu, X.-Z., Liang, Y., Chen, S.-P., Lin, J.-D. & Liao, D.-W. Pt-rich shell coated Ni nanoparticles as catalysts for methanol electro-oxidation in alkaline media. *Catalysis Communications* **10**, 1893-1897 (2009).

100   Ren, F., Wang, C., Zhai, C., Jiang, F., Yue, R., Du, Y., Yang, P. & Xu, J. One-pot synthesis of a RGO-supported ultrafine ternary PtAuRu catalyst with high electrocatalytic activity towards methanol oxidation in alkaline medium. *Journal of Materials Chemistry A* **1**, 7255-7261 (2013).

101   Koenigsmann, C. & Wong, S. S. One-dimensional noble metal electrocatalysts: a promising structural paradigm for direct methanol fuel cells. *Energy & Environmental Science* **4**, 1161-1176 (2011).

102   Yang, H., Zhang, J., Sun, K., Zou, S. & Fang, J. Enhancing by weakening: electrooxidation of methanol on Pt3Co and Pt nanocubes. *Angewandte Chemie* **122**, 7000-7003 (2010).

103   Liu, L., Pippel, E., Scholz, R. & Gösele, U. Nanoporous Pt− Co alloy nanowires: fabrication, characterization, and electrocatalytic properties. *Nano letters* **9**, 4352-4358 (2009).

104   Hoster, H., Iwasita, T., Baumgärtner, H. & Vielstich, W. Pt–Ru model catalysts for anodic methanol oxidation: influence of structure and composition on the reactivity. *Physical Chemistry Chemical Physics* **3**, 337-346 (2001).

105   Liao, L. W., Liu, S. X., Tao, Q., Geng, B., Zhang, P., Wang, C. M., Chen, Y. X. & Ye, S. A method for kinetic study of methanol oxidation at Pt electrodes by electrochemical in situ infrared spectroscopy. *Journal of electroanalytical chemistry* **650**, 233-240 (2011).

106   Lamberti, C., Zecchina, A., Groppo, E. & Bordiga, S. Probing the surfaces of heterogeneous catalysts by in situ IR spectroscopy. *Chemical Society Reviews* **39**, 4951-5001 (2010).

107   Jurzinsky, T., Kintzel, B., Bär, R., Cremers, C., Pinkwart, K. & Tübke, J. Methanol Oxidation on Ru-or Ni-Modified Pd-Electrocatalysts in Alkaline Media: A Comparative Differential Electrochemical Mass Spectrometry Study. *ECS Transactions* **75**, 983-995 (2016).

108   McGrath, K. M., Prakash, G. S. & Olah, G. A. Direct methanol fuel cells. *Journal of Industrial and Engineering Chemistry* **10**, 1063-1080 (2004).

109   Subbaraman, R., Tripkovic, D., Chang, K.-C., Strmcnik, D., Paulikas, A. P., Hirunsit, P., Chan, M., Greeley, J., Stamenkovic, V. & Markovic, N. M. Trends in activity for the water electrolyser reactions on 3d M (Ni, Co, Fe, Mn) hydr (oxy) oxide catalysts. *Nature materials* **11**, 550 (2012).

110   Wang, Y., Wang, G., Li, G., Huang, B., Pan, J., Liu, Q., Han, J., Xiao, L., Lu, J. & Zhuang, L. Pt–Ru catalyzed hydrogen oxidation in alkaline media: oxophilic effect or electronic effect? *Energy & Environmental Science* **8**, 177-181 (2015).

111   Bu, L., Guo, S., Zhang, X., Shen, X., Su, D., Lu, G., Zhu, X., Yao, J., Guo, J. & Huang, X. Surface engineering of hierarchical platinum-cobalt nanowires for efficient electrocatalysis. *Nature communications* **7**, 11850 (2016).

112   Zhang, Z., Luo, Z., Chen, B., Wei, C., Zhao, J., Chen, J., Zhang, X., Lai, Z., Fan, Z. & Tan, C. One-Pot Synthesis of Highly Anisotropic Five-Fold-Twinned PtCu Nanoframes Used as a Bifunctional Electrocatalyst for Oxygen Reduction and Methanol Oxidation. *Advanced Materials* **28**, 8712-8717 (2016).

113   Huang, W., Wang, H., Zhou, J., Wang, J., Duchesne, P. N., Muir, D., Zhang, P., Han, N., Zhao, F. & Zeng, M. Highly active and durable methanol oxidation electrocatalyst based on the synergy of platinum–nickel hydroxide–graphene. *Nature communications* **6**, 10035 (2015).

114   Cao, L., Zhao, Z., Liu, Z., Gao, W., Dai, S., Gha, J., Xue, W., Sun, H., Duan, X., Pan, X., Mueller, T. & Huang, Y. Differential Surface Elemental Distribution Leads to Significantly Enhanced Stability of PtNi-Based ORR Catalysts. *Matter* **1**, 1567-1580 (2019).

115   Huang, J., Liu, Y., Xu, M., Wan, C., Liu, H., Li, M., Huang, Z., Duan, X., Pan, X. & Huang, Y. PtCuNi Tetrahedra Catalysts with Tailored Surfaces for Efficient Alcohol Oxidation. *Nano Letters* **19**, 5431-5436 (2019).

116   Huang, L., Zhang, X., Wang, Q., Han, Y., Fang, Y. & Dong, S. Shape-Control of Pt–Ru Nanocrystals: Tuning Surface Structure for Enhanced Electrocatalytic Methanol Oxidation. *Journal of the American Chemical Society* **140**, 1142-1147 (2018).

117   Morin, M. C., Lamy, C., Léger, J. M., Vasquez, J. L. & Aldaz, A. Structural effects in electrocatalysis: Oxidation of ethanol on platinum single crystal electrodes. Effect of pH. *Journal of Electroanalytical Chemistry and Interfacial Electrochemistry* **283**, 287-302 (1990).

118   Busó-Rogero, C., Herrero, E. & Feliu, J. M. Ethanol Oxidation on Pt Single-Crystal Electrodes: Surface-Structure Effects in Alkaline Medium.

CHAPTER 2. SINGLE-ATOM TAILORING OF PLATINUM NANOCATALYSTS FOR HIGH-PERFORMANCE MULTIFUNCTIONAL ELECTROCATALYSIS

2.1 Introduction

Platinum represents the most iconic element for various energy-related electrocatalytic systems, such as hydrogen evolution reaction (HER), oxygen reduction reaction (ORR), methanol oxidation reaction (MOR), and ethanol oxidation reactions (EOR).[1-14] The intrinsic electrocatalytic activity and stability of Pt make it the most widely studied material for diverse electrochemical reactions. However, its high cost and scarcity seriously limit the practical applications of the Pt-based electrocatalysts and widespread adoption of the relevant technologies. Thus, a central challenge for all the Pt-powered reactions is how to substantially reduce the required amount of Pt in the catalysts, which demands a major leap in Pt mass activity (MA) (*i.e.*, the catalytic current per unit mass of Pt).

The MA is fundamentally determined by the product of the electrochemically active surface area (ECSA, normalized by mass) and the specific activity (SA, catalytic current normalized by ECSA). Considerable efforts have been placed on improving the ECSA by tailoring various geometrical factors, including creating ultrafine nanostructures or core/shell nanostructures with an ultrathin Pt skin to expose most Pt atoms on the surface for catalytic reactions.[15-21] In parallel, intensive efforts have been devoted to optimizing the SA for various electrochemical processes by tuning the chemical compositions, exposed catalytic surface, and surface topology[10,22-24]. In particular, surface modification/decoration of the existing Pt catalysts represents an interesting pathway to tailor the electrocatalytic activity. For example, combining Pt-based material with transition metal hydroxides (e.g., Ni(OH)$_2$) has been shown to greatly enhance SA for HER and MOR in alkaline electrolytes.[13,25,26] However, such modification inevitably blocks

some surface active sites and often results in a relatively small ECSA (~20-60 m^2/g$_{Pt}$, typically with 30-50% lower than those without modification).[1,27] This represents an intrinsic dilemma for the surface modification strategy, which may tailor the local electronic structure to boost the SA for a given reaction, but usually at a substantial sacrifice of the ECSA. Together, these competing factors make it extremely challenging to simultaneously achieve a high SA and a high ECSA in the same catalyst system, which is necessary for delivering a high MA.

C	Surface Pt sites before decoration	Surface Pt sites after decoration	Pt sites with Ni neighbor	Pt sites w/o Ni neighbor	Pt sites blocked by Ni
SANi-decorated Pt surface	1394	1204	933	271	190
Ni NPs decorated Pt Surface	1394	557	356	201	837
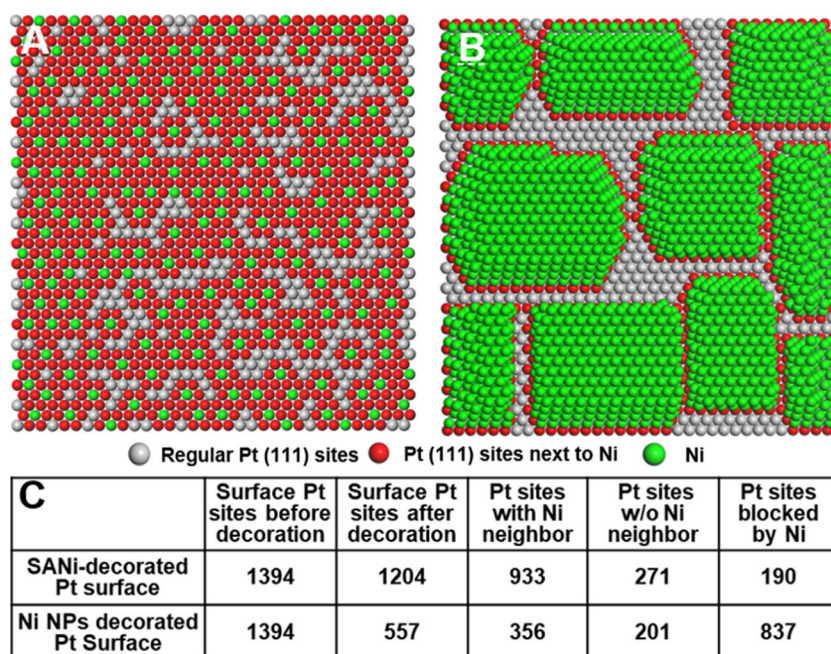
Figure 2.1. A simplified model of Pt (111) surface decorated by (A) single Ni atom species [Ni(OH)$_2$ species, simplified as Ni] and (B) 1-2 nm nanoparticles, with grey representing regular Pt (111) surface site, red representing activated Pt atoms with Ni neighbor, and green representing sites blocked by Ni. (C) Comparing different types of Pt sites for the single atom and nanoparticle decorated Pt surface in the simplified model in a and b. For a Pt (111) surface with a total 1394 Pt sites decorated with 190 single Ni atoms (green), there are a total of 1204 exposed Pt atoms, with 933 having a Ni neighbor (red) and 271 having no Ni neighbor (blue); while for the same Pt (111) surface (a total of 1394 initial Pt surface sites) decorated with 1-2 nm Ni nanoparticles, there are only 557 exposed Pt atoms on the surface, with 356 having a Ni neighbor and 201 without Ni neighbor. This comparison highlights the single atom

modifications activate a lot more surface sites (with Ni neighbors) while blocking much fewer Pt sites.

In general, for Pt nanocatalysts decorated with a given transition metal (*e.g.*, nickel) species, in which the nickel-based nanostructures function as the catalyst promoter to enhance the catalytic activity of nearby surface Pt atoms, it is important to minimize the size of the decorating species to prevent unnecessary blockage of surface Pt sites while creating the most activated Pt site with nickel neighbors for enhanced SA. In this regard, the ultimate limit of the decorating species is single atoms, which uses the smallest number of nickel species to activate the most Pt atoms while blocking the least amount of surface Pt sites to ensure the highest mass activity (**Figure 2.1**). However, the creation of the single-atom decorated Pt surface is challenging with typical synthetic approaches and has not been realized to date.

Pt with Ni neighbor   Pt without Ni neighbor   Ni
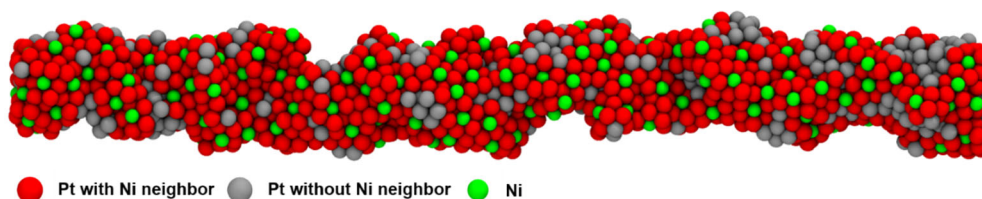
Figure 2.2. The schematic diagram for SANi-PtNWs. The decoration of ultrafine PtNWs with single atomic nickel species tailors the local electronic structure to boost the specific catalytic activity for diverse electrochemical reactions with minimal sacrifice in the number of surface-active sites. Grey atoms represent regular Pt (111) surface sites, green atoms represent isolated Ni sites (Ni is liganded to two OH groups in electrocatalytic conditions), and red atoms represent activated Pt atoms with Ni neighbor as catalytically hot sites.

Herein, by starting with PtNi alloy nanowires and using a partial electrochemical dealloying approach, we create single-atom nickel modified Pt nanowires (SANi-PtNWs) with abundant activated Pt sites next to SANi and minimal blockage of the surface Pt sites (**Figure 2.2**), thus enabling a unique design of single-atom tailored Pt electrocatalysts with an optimum

combination of SA and ECSA to deliver high MA for diverse electrochemical reactions including hydrogen evolution reaction (HER), methanol oxidation reaction (MOR), and ethanol oxidation reaction (EOR), with high catalyst durability. Importantly, we show that the resulting SANi-PtNWs display a substantially increased MA of 11.8 ± 0.43 A/mg$_{Pt}$ for HER at -70 mV *vs.* RHE at pH 14 (comparing with the previous record of 3.03 A/mg$_{Pt}$)[3]. Density functional theory (DFT) calculations reveal that all Pt atoms around SANi show a reduced hydrogen binding energy and are optimal for HER. We further show that such single atomic modification also greatly enhances the catalytic activity for both MOR and EOR to deliver a mass activity of 7.93 ± 0.45 A/mg$_{Pt}$ and 5.60 ± 0.27 A/mg$_{Pt}$ (*vs.* previous records of 2.92 A/mg$_{Pt}$ and 2.95 A/mg$_{Pt}$)[6,9], respectively. These studies demonstrate that the single-atom tailoring approach offers a general strategy for creating highly efficient electrocatalysts for diverse reactions.

2.2 Experiment Section

Synthesis of PtNi alloy NWs. All chemicals were purchased from Sigma-Aldrich unless otherwise specified. In a typical synthesis, 20 mg Pt(acac)$_2$ and 40 mg Ni(acac)$_2$ were mixed with 130 mg glucose, 1.7 mg W(CO)$_6$ and 60 mg PVP-40 in a glass vial, with 5 ml of oleylamine and octadecene (3:2 volume ratio) as co-solvent. The mixture was heated to 140 ºC for 6 hours to form Pt-NiO core-shell nanowires. The result nanowires were collected via centrifuge at 7000 rpm for 20 min. After loading the nanowires on carbon black, the catalysts were then annealed under 450 ºC in argon/hydrogen (97:3) atmosphere for 12 hours to obtain the PtNi alloy nanowires supported on carbon black.

Material Characterizations. High spatial resolution STEM-EELS experiments were conducted by Nion UltraSTEM-200, equipped with C3/C5 corrector and high-energy resolution monochromated EELS system. The instrument was operated at 60 kV with a convergence semi-

angle of 30 mrad and a beam current of ~100 pA. HAADF-STEM imaging was performed using an inner and outer collection semi-angle of 70 and 210 mrad. EELS measurement was carried out using a dispersion of 0.26 eV/channel and the dwell time of 0.5 s/pixel. Background in each spectrum was removed by power-law function in commercial software package Digital Micrograph.

X-ray absorption data analysis. The X-ray absorption fine structure spectra for Ni K-edge and Pt L-edge EXAFS data were recorded at the microprobe beamline 10.3.2 of the Advanced Light Source (ALS), Lawrence Berkeley National Laboratory (LBNL). The storage ring was operated in top-off mode (1.9 GeV and 500 mA). Using a Si (111) monochromator, the data collection was carried out in fluorescence mode for all samples under ambient conditions. The beam spot size was 15×3 μm^2 for XANES and EXAFS measurements. The acquired EXAFS data were processed according to the standard procedures using the ATHENA module implemented in the IFEFFIT software packages. The k^3-weighted EXAFS spectra were obtained by subtracting the post-edge background from the overall absorption and then normalizing with respect to the edge-jump step. Subsequently, k^3-weighted $\chi(k)$ data were Fourier transformed to real (R) space using a hanning windows (dk=1.0 $Å^{-1}$) to separate the EXAFS contributions from different coordination shells. To obtain the quantitative structural parameters around central atoms, least-square curve parameter fitting was performed using the ARTEMIS module of the IFEFFIT software packages.

The following EXAFS equation was used:

$$\chi(k)=\sum_{j}\frac{N_{j}S_{o}^{2}F_{j}(k)}{kR_{j}^{2}}\exp[-2k^{2}\sigma_{j}^{2}]\exp[\frac{-2R_{j}}{\lambda(k)}]\sin[2kR_{j}+\phi_{j}(k)] \tag{1}$$

S_0^2 is the amplitude reduction factor, $F_j(k)$ is the effective curved-wave backscattering amplitude, N_j is the number of neighbors in the jth atomic shell, R_j is the distance between the X-ray absorbing central atom and the atoms in the jth atomic shell (backscatterer), λ is the mean free path in Å, $\phi_j(k)$ is the phase shift (including the phase shift for each shell and the total central atom phase shift), σ_j is the Debye-Waller parameter of the jth atomic shell (variation of distances around the average R_j). The functions $F_j(k)$, λ and $\phi_j(k)$ were calculated with the *ab initio* code FEFF8.2.

Electrochemical measurements for HER. To prepare the SANi-PtNW catalyst ink, 2 mg catalysts (SANi-PtNWs on Vulcan 72 carbon black) were dispersed in 2 mL pure ethanol. 20 μL Nafion 117 solution was added to the ink as the binder. 30 μL ink was drop-cast on the glassy carbon electrode (0.196 cm^2). For Pt/C, 2 mg Pt/C (10% Pt/C purchased from Alfa Aesar) were dispersed in 2 mL pure ethanol, with 20 μL Nafion 117 solution added as the binder. 10 uL Pt/C ink was drop-cast on the glassy carbon electrode (0.196 cm^2). The Pt loading on RDE for Pt/C, pure-PtNWs, and SANi-PtNWs was 3.0 μg/cm^2, 2.0 μg/cm^2, and 2.0 μg/cm^2 respectively for RDE test. Alkaline/mercury oxide electrode was used as the reference electrode, and graphite rod was used as the counter electrode. The reference electrode calibration was completed in H_2-saturated 1 M KOH at room temperature. 1600 rpm rotation speed was applied on working RDE to get rid of generated bubble during the performance test. The ECSA was determined by H_{upd} at 0.05 V – 0.35 V vs. RHE in 0.1 M $HClO_4$. The specific and mass current densities were normalized by the ECSA and total Pt loading.

Electrochemical measurements for MOR and EOR. Alkaline/mercury oxide electrode was used as the reference electrode, and graphite rod was used as the counter electrode. The reference electrode calibration was completed in H_2-saturated 1 M KOH at room temperature. 1 M methanol and ethanol were added to the electrolyte as the reactant for MOR and EOR, respectively. The Pt

loading on RDE for Pt/C, pure-PtNWs, and SANi-PtNWs was 3.0 μg/cm^2, 3.47 μg/cm^2, and 3.47 μg/cm^2, respectively. The ECSA was determined by H$_{upd}$ at 0.05 V – 0.35 V vs. RHE in 0.1M HClO$_4$. The specific and mass current densities were normalized by the ECSA and total Pt loading.

Electrochemical measurements for acidic CO stripping. The CV dealloying cycles were interrupted at 10th, 50th, 100th, 150th, 180th and 200th cycles. Before each CO stripping measurement, we firstly performed chronoamperometry at 0.05 V *vs*. RHE in CO saturated electrolyte (0.1 M HClO$_4$) for 10 min. Then we performed chronoamperometry at 0.05 V *vs*. RHE in N$_2$ saturated electrolyte (0.1 M HClO$_4$) for 10 min. The CO stripping CV scan range was set in 0.05 V to 1.1 V vs. RHE with a positive-scan starting direction. The scan rate was set to 50 mV/s. Ag/AgCl electrode was used as the reference electrode, and graphite rod was used as the counter electrode.

Electrochemical measurements for alkaline CO stripping. For the alkaline CO striping experiment, we first performed chronoamperometry at 0.05 V *vs*. RHE in CO saturated electrolyte (1 M KOH) for 15 min. After the current reached to a steady-state, we then performed chronoamperometry at 0.05 V *vs*. RHE in N$_2$ saturated electrolyte (1 M KOH) for 10 min. The CO stripping CV scan range was set between 0.05 V to 1.1 V *vs*. RHE with a positive-scan starting direction. The scan rate was set to 25 mV/s. alkaline/mercury oxide electrode. The graphite rod was used as the counter electrode.

Computational details All the DFT calculations are carried out by *VASP*[41,42] with the PBE exchange-correlation functional[43]. The one-electron wavefunction is developed on a plane wave basis set with a 450 eV energy cut-off. The reciprocal space is sampled using a 5×5×1 K-point grid for systems with 4×4 or 5×5 unit cell, and 7×7×1 K-points for systems with 3×3 unit cell. All model slabs contain 5 layers. For the models with cavities, the top three layers are fully relaxed,

while for the models with Ni(OH)$_2$ decoration, the top two layers are relaxed. The convergence threshold on atomic forces is 0.01 eV/Å.

Calculation of adsorption free energy

The adsorption free energy of H$_2$ is calculated by equation (2):

$$\Delta G_{nH} = G(\text{slab}+n\text{H}) - G(\text{slab}) - \frac{n}{2}G(\text{H}_2) \tag{2}$$

G is the Gibbs free energy, and n is the number of adsorbed H atoms. We used the following equations to calculate the free energies:

$$G(\text{slab}+n\text{H}) = E(\text{slab}+n\text{H}) + \text{ZPE }(n\text{*H}) + \text{TS}_{vib}(n\text{*H}) \tag{3}$$

$$G(\text{slab}) = E(\text{slab}) \tag{4}$$

$$G(\text{H}_2) = E(\text{H}_2) + ZPE(\text{H}_2) + TS(\text{H}_2) \tag{5}$$

In equation (3), $E(\text{slab}+n\text{H})$ is the electronic energy of the metal slab with adsorbed H atoms, *H means the adsorbed H atom, ZPE (n*H) means the zero point energy of n adsorbed H atoms, T is the temperature, and S_{vib} is the vibrational entropy. The latter two terms are calculated from the vibrational frequencies v_i of the adsorbed H atoms by using equations (6) and (7):

$$ZPE(n\text{*H}) = \sum_{i=1}^{3n} \frac{hv_i}{2} \tag{6}$$

$$S_{vib}(n\text{*H}) = \sum_{i=1}^{3n} \left\{ \frac{hv_i \exp(-hv_i/2k_BT)}{k_BT[1-\exp(-hv_i/2k_BT)]} - \ln\left[1-\exp(-hv_i/2k_BT)\right] \right\} \tag{7}$$

When calculating the vibrational frequencies of multiple adsorbed H atoms, the slab thickness was reduced by one layer to reduce the computational cost.

Relative free energy with respect to Pt (111) $\Delta G_H - \Delta G_H{}^{Pt\,(111)}$ ($\Delta\Delta G$), are calculated using a 5 layer Pt (111) surface with 4×4 unit cell.

Calculation of adsorption free energy in the solution with the effect of applied potential and pH.

$$\Delta G = G(\text{slab}+n\text{H}) - G(\text{slab}) - \frac{n}{2}G(\text{H}_2) - n\mu_{H^++e^-} \tag{8}$$

$$\mu_{H^++e^-} = -eU_{SHE} - 2.3kTpH \tag{9}$$

We used equation (8) to calculate the adsorption free energy with the impact of the reduction potential on the electrode, where the first three terms on the right side are the same as the terms in equation (2), the term $\mu_{H^++e^-}$ is the chemical potential of hydrogen ion and electron, which is calculated using equation (9)[44]. U_{SHE} is the potential vs. standard hydrogen electrode.

2.3 Synthesis and Structure Characterization

A simple one-pot synthetic procedure followed by an annealing process in argon/hydrogen mixture (Ar/H$_2$: 97/3) was used to produce the Ni-rich PtNi alloy NWs (composition ~Pt$_{17}$Ni$_{83}$) with an average length of ~300 nm and diameter of ~4.5 nm (**Figure 2.3A**). The resulted PtNi NWs were dispersed on carbon support in ethanol to form the catalyst ink, which was then cast onto glassy carbon rotating disk electrode (RDE, geometry area = 0.196 cm^2) to form a homogeneous film. An electrochemical dealloying process was performed via cyclic voltammetry (CV) between 0.05 V - 1.10 V *vs.* RHE in 0.1 M HClO$_4$ to gradually remove nickel species. The ECSA gradually increases with the increasing number of CV cycles and eventually saturates at about 112.9 ± 5.4 m^2/g$_{Pt}$ after 200 CV cycles (**Figure 2.3C and D**), which indicates the completion of the dealloying process to obtain pure Pt NWs (pure-PtNWs)[10]. Such an ECSA evolution trend

was also confirmed by acidic CO stripping experiments (**Figure 2.3E, F**). The average diameter is reduced from ~4.5 nm before to ~2.0 nm after the complete dealloying process (**Figure 2.3B**).
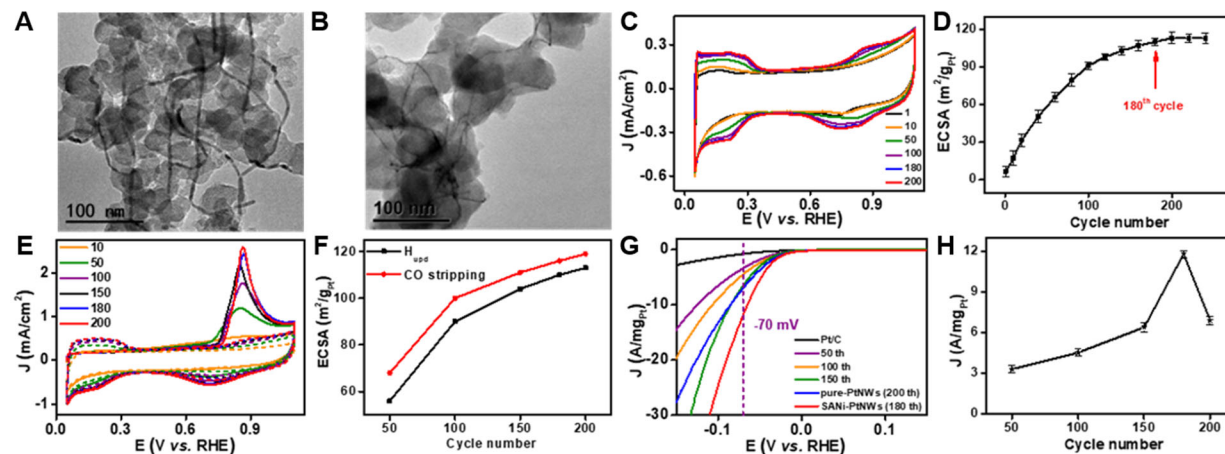
Figure 2.3. (A) TEM images of PtNi alloy nanowire and (B) TEM images of SANi-PtNWs. (C) CV in 0.1 M $HClO_4$ of PtNi alloy NWs at different scan cycles. (D) ECSA evolution of the nanowire samples with the increasing number of dealloying CV cycles (error bars showing the variations from 10 independent batches). (E) The acidic CO stripping curves for $Pt_{17}Ni_{83}$ nanowires de-alloyed at different cycles. (F) Comparison of the ECSA evolution (vs. the number of dealloying CV cycles) derived from Hupd and CO stripping, respectively. (g) HER polarization curve for Pt/C and PtNi nanowires dealloyed with different numbers of CV cycles. (H) The mass activity of the dealloyed nanowires as a function of the number CV cycles, with the peak HER activity achieved after the 180th CV cycles, when the surface decorating species is in single atomic state to ensure maximum activation and the least surface blockage. Error bars in D and H indicate the standard deviation from ten independent samples.

To tailor the nickel decoration in the resulting PtNWs, we interrupt the acidic CV dealloying process periodically to produce PtNWs with different amounts of nickel decorating species, which was then transferred into nitrogen-saturated 1 M KOH for 100 additional CV cycles between 0.05 V – 1.6 V for further activation. The resulting dealloyed NWs with selectively decorated Ni species are generally stable in the basic conditions, in which their catalytic

performance is evaluated. We have initially used HER as a model reaction to evaluate the activity of the resulting PtNW catalysts with varying amounts of nickel species (**Figure 2.3G**) and discovered that the peak performance is achieved at 180 acidic dealloying CV cycles. Too much (<180 cycles) or too little (>180 cycles) nickel species would reduce the overall HER activity (**Figure 2.3H**). The produced Ni species are stable in basic conditions. We have thus focused our discussion on this optimum material produced with 180 dealloying CV cycles unless otherwise specifically mentioned.

A high-angle annular dark-field scanning transmission electron microscope (HAADF-STEM) was conducted to probe the atomic structure of the resulting material. The HAADF-STEM shows an ultrafine 1D crystalline configuration with rich surface defects, concave cavity sites and steps as highlighted by white arrows (**Figure 2.4A**). HAADF-STEM image shows that the (111) spacing is 0.225 nm (**Figure 2.4A**), about 2.2 % smaller than that of crystalline Pt (0.230 nm). The composition analysis by inductively coupled plasma atomic emission spectrometry (ICP-AES) reveal an overall Pt:Ni ratio of 92:8 for SANi-PtNWs, corresponding to 2.4 Ni atoms per square nanometer surface area. Considering the Pt surface atom density around 15 Pt/nm^2, the surface Ni:Pt atom ratio is around 1:6. Electron energy loss spectroscopy (EELS) elemental mapping of Ni (**Figure 2.4B**) and that overlaid on Pt HAADF contrast image (**Figure 2.4C**) reveals that the nickel atoms are sparsely distributed on the PtNWs.
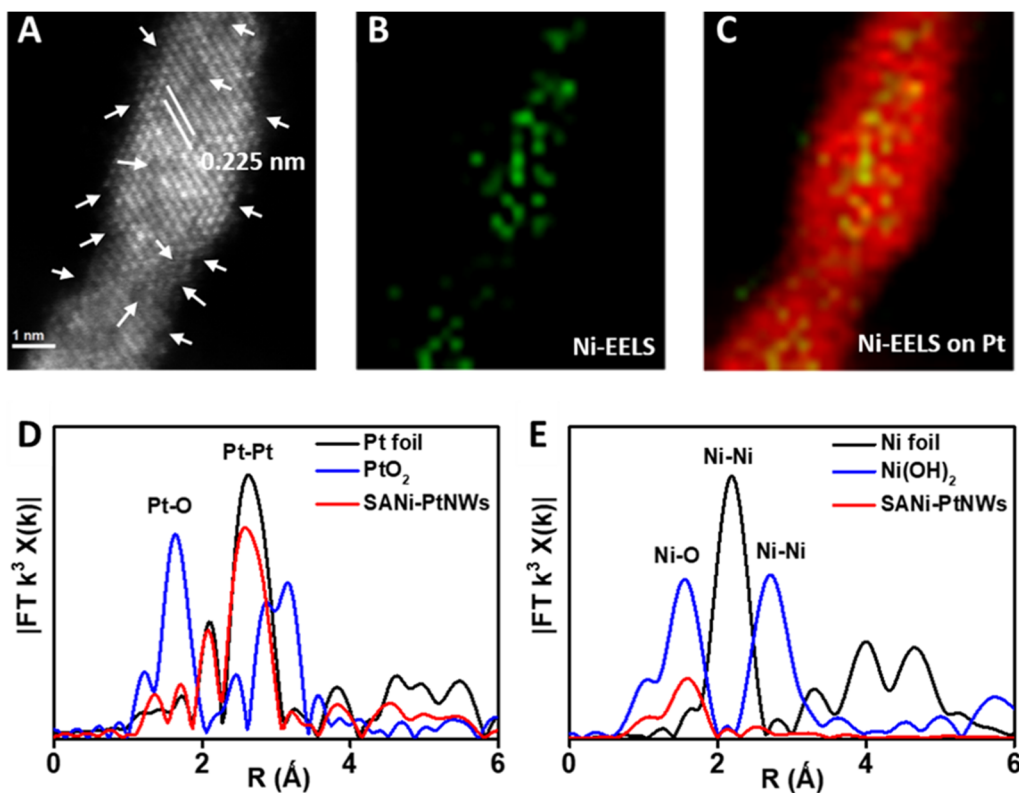
Figure 2.4. Structural characterization of the SANi-PtNWs. (**A**) HAADF-STEM image of SANi-PtNWs, with the white arrows highlight the surface defects, steps, and concave cavity sites. (**B**) Ni EELS mapping. (**C**) Overlaid image of Ni-EELS mapping on Pt, with red representing Pt and green representing Ni. (**D**) Pt EXAFS fitting result and (**e**) Ni EXAFS fitting result.

We have further conducted the X-ray absorption fine structure (XAFS) and X-ray absorption near edge structure (XANES) measurements to probe the local atomistic and electronic structures. The oxidation state of Pt can be probed by the white line intensity at Pt L_3-edge in XANES spectra.[28,29] The Pt XANES result shows that the white line intensity of our sample (**Figure 2.5A**) is close to that of a Pt foil, indicating that the average oxidation state of Pt is mostly zero. The Pt extended X-ray absorption fine structure (EXAFS) fitting result shows a main peak at about 2.74 Å (**Figure 2.4D, Table 2.1**), which is about 1.8 % smaller than the Pt-Pt bond length

in bulk Pt (2.79 Å in Pt foil), consistent with the TEM studies described above and previous report.[10]
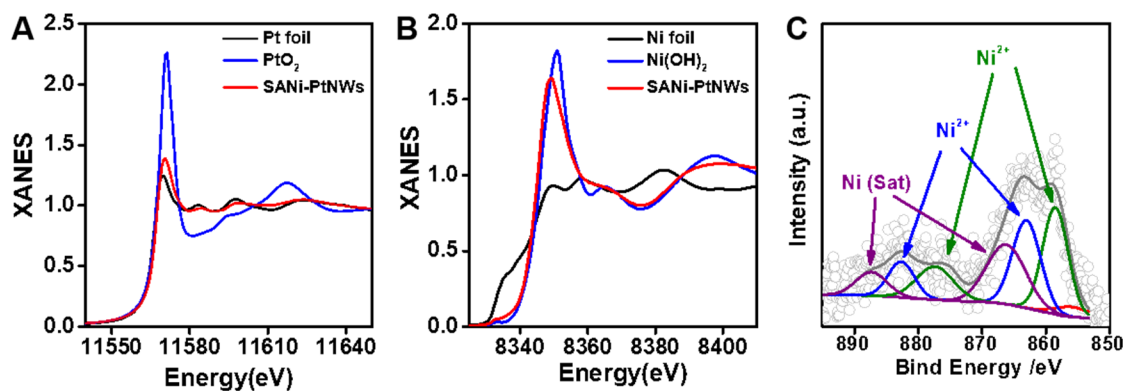
Figure 2.5. (A) XANES spectra of Pt L_3-edge and (B) XANES spectra of Ni K-edge. (c) The XPS result for Ni 2p of SANi-PtNWs post electrocatalytic test.

Table 2.1. Structural parameters extracted from the Pt L_3-edge EXAFS fitting. (S_0^2=0.78)

Sample	Scattering pair	CN	R(Å)	$\sigma^2(10^{-3}Å^2)$	ΔE_0(eV)	R factor
SANi-PtNWs	Pt-Pt	8.9	2.74	7.1	5.4	0.01
Pt foil	Pt-Pt	12*	2.79	4.3	7.7	0.0062
PtO$_2$ bulk	Pt-O	2*	1.97	3.2	7.5	0.0043
	Pt-O	4*	2.05	4.1		
	Pt-Pt	2*	3.12	3.4	13.6	

S_0^2 is the amplitude reduction factor; CN is the coordination number; R is the interatomic distance (the bond length between Pt central atoms and surrounding coordination atoms); σ^2 is Debye-Waller factor (a measure of thermal and static disorder in absorber-scatterer distances); ΔE_0 is edge-energy shift (the difference between the zero kinetic energy value of the sample and that of the theoretical model). R factor is used to value the goodness of the fitting. * This value was fixed during EXAFS fitting, based on the known structure of Pt metal and PtO$_2$ bulk. Error bounds that characterize the structural parameters obtained by EXAFS spectroscopy were estimated as N ± 20%; R ± 1%; σ^2 ± 20%; ΔE_0 ± 20%.

Table 2.2. Structural parameters extracted from the Ni K-edge EXAFS fitting (S_0^2=0.77).

Sample	Scattering pair	CN	R(Å)	$\sigma^2(10^{-3}\text{Å}^2)$	$\Delta E_0(eV)$	R factor
SANi-PtNWs	Ni-O	2.3	2.04	5.3	-2.5	0.01
Ni foil	Ni-Ni	12*	2.49	5.9	6.1	0.0013
Ni(OH)$_2$ bulk	Ni-O	6*	2.05	5.3	4.3	0.0038
	Ni-Ni	6*	3.12	6.4	7.2	

S_0^2 is the amplitude reduction factor; CN is the coordination number; R is interatomic distance (the bond length between Ni central atoms and surrounding coordination atoms); σ^2 is Debye-Waller factor (a measure of thermal and static disorder in absorber-scatterer distances); ΔE_0 is edge-energy shift (the difference between the zero kinetic energy value of the sample and that of the theoretical model). R factor is used to value the goodness of the fitting. * This value was fixed during EXAFS fitting, based on the known structure of Ni metal and Ni(OH)$_2$ bulk. Error bounds that characterize the structural parameters obtained by EXAFS spectroscopy were estimated as N ± 20%; R ± 1%; σ^2 ± 20%; ΔE_0 ± 20%.

The XANES for Ni K-edge provides information on the oxidation state of Ni species based on the absorption threshold position and white line intensity (due to the allowed 1s→4p transition).[30] The Ni K-edge XANES in our optimum material closely resembles that of Ni(OH)$_2$ with slightly lower intensity (**Figure 2.5B**), suggesting the nickel species have an average oxidation state close to two, and primarily exists as surface decorating species (an oxidation state of zero is expected for the buried nickel). Further XPS studies also confirmed the 2+ oxidation state of the Ni species (**Figure 2.5C**). The Ni EXAFS shows a single peak at 1.6 Å (**Figure 2.4E, Table 2.2**), which can be attributed to the first shell Ni-O bond. There is no obvious peak at 2.1 Å (for Ni-Ni coordination in metallic Ni) or 2.7 Å (For Ni-O-Ni coordination in Ni(OH)$_2$) (**Figure 2.4E**), strongly confirming that the Ni species exist as single atomic species without long-range coordination to another Ni center. The XANES and EXAFS hence demonstrate the successful creation of single atom nickel modified PtNWs (SANi-PtNWs) catalysts.

2.4 HER Measurements of the SANi-PtNWs
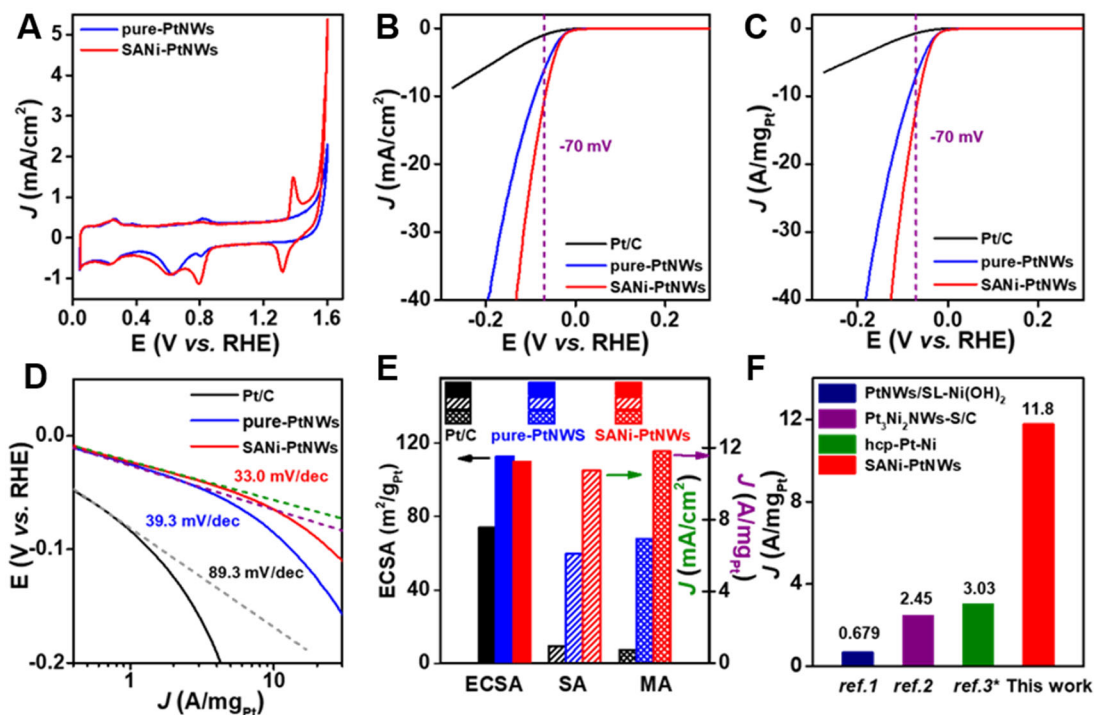
Figure 2.6. Electrocatalytic performance of the SANi-PtNWs for HER compared against Pt/C and pure-PtNWs in 1 M KOH electrolyte. (**A**) Cyclic voltammetry (CV) performed between 0.05 V – 1.60 V vs. RHE at a scan rate of 50 mV/s. (**B**) Electrochemically active surface area normalized and (**C**) Pt mass loading normalized HER LSVs with 95% iR-compensation at the scan rate of 5 mV/s. (**D**) Pt mass normalized HER Tafel-slope. (**E**) Comparison of ECSA (black arrow to the left), specific activities (normalized by ECSA, green arrow to the right) and mass activities (normalized by Pt mass, purple arrow to the right) for HER at -70 mV vs. RHE for all tested materials. (**F**) Comparison of HER mass activity of the SANi-PtNWs at -70 mV vs. RHE with the state-of-art values reported previously. * The material in Ref. 3 was tested in 0.1 M KOH. Error bars in e and f indicate the standard deviation of ten independent samples.

The HER activity of the SANi-PtNWs was investigated by using the rotating disk electrode (RDE) test and compared against the fully dealloyed pure-PtNWs and the commercial Pt/C (10 wt%). The CV studies of the SANi-PtNWs show two exclusive Ni^{2+}/Ni^{3+} redox peaks at 1.321 V

($Ni^{3+} \rightarrow Ni^{2+}$) and 1.388 V ($Ni^{2+} \rightarrow Ni^{3+}$) *vs.* RHE respectively (**Figure 2.6A**), which are absent in the pure-PtNWs. These redox peaks are widely recognized as the signature of nickel species,[31,32] which further confirms that the nickel species were successfully decorated on PtNWs. The integration of the hydrogen absorption desorption region gives a high ECSA of the 106.2 ± 4.5 m^2/g_{Pt} for SANi-PtNWs, nearly comparable to that of the pure-PtNWs, and considerably larger than those the previously reported Pt-Ni(OH)$_2$ based nano-composites (ECSA~20-60 m^2/g_{Pt}),[1,4] highlighting it is critical to precisely tune the number and structure of the decorating species to prevent undesired blockage of surface reactive sites and ensure high ECSA.

The HER performance of SANi-PtNWs was further evaluated using linear sweep voltammetry (LSV) at room temperature in 1 M N$_2$-saturated KOH with a scan rate of 5 mV/s and compared against commercial Pt/C and pure-PtNWs (**Figure 2.6B**). The specific activities are 0.95, 6.11 ± 0.34, and 10.72 ± 0.41 mA/cm^2 at -70 mV vs. RHE for the Pt/C, pure-PtNWs, and SANi-PtNWs, respectively. It should be noted that the specific activities reported here are normalized to the ECSA, in contrast to the electrode geometrical area used in some previous studies.[2] Meanwhile, the LSV curves normalized by Pt mass give a mass activity of 0.71, 6.90 ± 0.36, and 11.80 ± 0.43 A/mg$_{Pt}$ for Pt/C, pure-PtNWs, and SANi-PtNWs at -70 mV vs. RHE (**Figure 2.6C**). The Tafel diagrams give a Tafel-slope of 60.3 mV/dec for the SANi-PtNWs compared to 78.1 mV/dec for the PtNWs and 133.4 mV/dec for the Pt/C (**Figure 2.6D**), clearly demonstrating the considerably improved HER kinetics with the single Ni atom decorated catalysts.
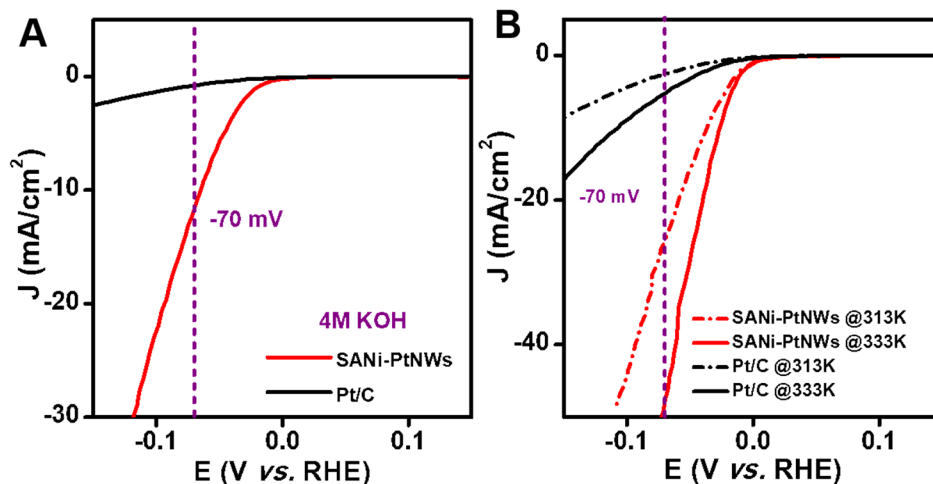
Figure 2.7. HER performance of the SANi-PtNWs and Pt/C under harsher conditions. (A) ECSA normalized HER LSVs for Pt/C and SANi-PtNWs in 4 M KOH with 95% iR-compensation at the scan rate of 5 mV/s. (B) ECSA normalized HER LSVs for Pt/C and SANi-PtNWs at 313 K and 333 K, respectively. The measurements were conducted in 1 M KOH with 95% iR-compensation at the scan rate of 5 mV/s.

We have further compared the ECSA, SA and MA of the three different catalysts tested (**Figure 2.6E**). Both the pure-PtNWs and the SANi-PtNWs exhibit a similar ECSA, much higher than that of the Pt/C control. Importantly, the specific activity of the SANi-PtNWs is nearly twice that of the pure-PtNWs, clearly demonstrating that the SANi decoration considerably improves the HER kinetics. Together, with the simultaneous achievement of high ECSA and high SA, the SANi-PtNWs deliver a clear leap in mass activity, achieving an MA about 3-10 times higher than those of the state-of-the-art HER catalysts reported to date (**Figure 2.6F** and **Table 2.3**). Additionally, at -70 mV *vs.* RHE, SANi-PtNWs showed a specific activity (normalized by ECSA) of 11.8 mA/cm^2 in 4 M KOH (**Figure 2.7A**) and 25.7 mA/cm^2 and 48 mA/cm^2 at elevated temperature (313 K and 333 K, **Figure 2.7 B**), about 9-14 times higher than those of Pt/C. These results indicate the promoted HER activity of SANi-PtNWs is maintained under harsher conditions.
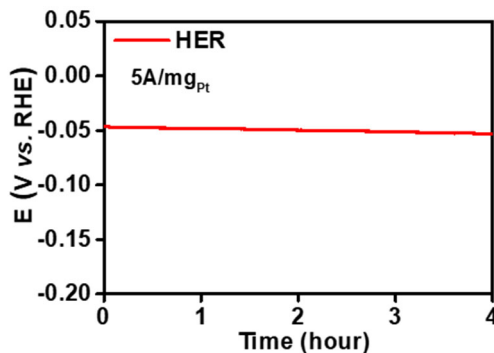
Figure 2.8. HER chronopotentiometry test of SANi-PtNWs, in 1 M KOH at a constant current density of 5 A/mg$_{Pt}$.

We should also note that the preparation of SANi-PtNWs by interrupted dealloying process is highly repeatable and the resulting materials show consistent performance in 10 independent batches. Furthermore, chronopotentiometry stability test shows negligible over-potential change for HER when operating at a constant current density of 5 A/mg$_{Pt}$ in 1 M KOH after 4 hours, suggesting such single atomic decoration is stable in the electrochemical processes (**Figure 2.8**). The improved HER durability could be partly attributed to multipoint line contacts between the 1D NWs and the carbon support, which prevents physical movement and aggregation (note that the movement and aggregation 0D nanoparticle catalysts contribute significantly to the degrading activities); Additionally, the SANi-PtNWs can effectively reduce the reaction kinetic barrier, delivering a higher current density at the reduced over-potential, which could also contribute to **the durability of the catalyst during long time operation.**

Table 2.3. Comparing HER performance of SANi-PtNWs and pure-PtNWs *vs.* the state-of-the-art at -70mV *vs.* RHE.

Material	Test condition	ECSA (m^2/g$_{Pt}$)	SA (mA/cm^2)	MA (A/mg$_{Pt}$)
SANi-PtNWs	1 M KOH	**106.2 ± 4.5**	**10.72 ± 0.41**	**11.8 ± 0.43**
pure-PtNWs		112.9 ± 5.4	6.11 ± 0.34	6.90 ± 0.36

PtNWs/SL Ni(OH)$_2$[#]	1 M KOH	27.4	2.48	0.68
Pt$_3$Ni$_2$ NWs-S/C[†]	1 M KOH	NA	NA	2.45
hcp-Pt-Ni[§]	0.1 M KOH	26.6	11.41	3.03

[#]Pt nanowires grown on single-layered Ni(OH)$_2$ nanosheets (Ref 1); [†]PtNi/NiS nanowires (Ref 2); [§]hcp

platinum-nickel alloy excavated nano-multipods (Ref 3).

2.5 Density Functional Theory Calculations of HER Activity

To further explore the impact of the SANi species on HER activity, we have conducted

density functional theory (DFT) calculations, probing the hydrogen (H) adsorption free energies

on a series of model catalytic active sites[33]. We have first considered the fully dealloyed pure-

PtNWs that present a variety of defect sites including atoms with lower and higher metallic

coordination than the regular Pt (111) termination. To this end, we constructed representative

models of the local surface environments in the form of steps or one-layer concave cavities[21]. The

local surface environment at these sites has been described using three models: model *A* (**Figure**

2.9 A and **Figure 2.10 A**) and *B* (**Figure 2.10 B**) consisting of different size concave cavities on

the Pt (111) surface, and model *C* (**Figure 2.10C** and **D**) consisting of a Pt (553) stepped surface.

Figure 2.9. Density functional theory (DFT) calculations of the active sites. (A) Cavity defect on the Pt (111) surface (Model A). The unit cell is 4×4, and the figure shows 2 unit cells. The locally stable adsorption sites for the H atom are labeled on the top view model. (B) Exchange current i_0 for HER as a function of *H adsorption free energy for the locally stable adsorption sites in Models A, B and C. (C) Adsorption free energy of hydrogen on model A Pt surface as a function of the applied potential U_{RHE} at various coverage in pH=14 solution. (D) Model D for SANi decorated Pt (111) surface, Ni atom being in the surface layer. The unit cell is 3×3, and the figure shows 2 unit cells. (E) Volcano curve for adsorption sites on model D at low coverage (LC) and high coverage (HC) conditions. (F) Adsorption free energy of hydrogen on model D as a function of U_{RHE} at various coverage at pH=14.

50

Figure 2.10. DFT models for HER activity calculation. To better distinguish the sites in Models A, C, E, and F, we use two letters to label the adsorption sites. The first letter indicates whether the site is top (T), bridge (B), FCC hollow (F) or HCP hollow (H), the second letter indicates whether the site is in a cavity (C), on the step (S), or on the terrace (T). For the adsorption sites in Models B, D and G, there are no cavities so we use simple labels to represent whether the site is top (T), bridge (B), FCC hollow (F) or HCP hollow (H). The local minima sites are in red color. The adsorption free energies ($\Delta G_H - \Delta G_H^{Pt\ (111)}$) for all the adsorption sites are shown in Supplementary Table 3. Besides that, we also directly write the adsorption free energies on the adsorption sites. The local minima sites are in red color. (A) Model A with 4×4 unit cell and 5 layers. BS1 and BS2 are the most stable adsorption sites. By symmetry, there are 3 BS1 and 6 BS2 sites in one unit cell. Since they will be occupied first and they will block TS1, TS2 and FT1 sites, FT3 and TT1 sites will become the local minima sites. The TC site in the cavity is another local minimum. (B) Model B with 5×5 unit cell and 5 layers. Model C has a larger cavity than Model A, but there are many similarities. The BS sites are still the most stable sites. The TS sites have lower energies than TT3, FT2 and FT3, but they are blocked by the BS sites, so the local minima sites on the terrace are TT3, FT2, FT3 and FT4. The

51

TC site in the cavity is still a local minimum site. (C) Model C of Pt (553) stepped surface. (D) Bond lengths (Å) in model C. The Pt-Pt distance in bulk is 2.81 Å. Model C is Pt (553) surface and it's a model for the step defect. We find the fcc hollow sites, such as F1, F2 and F3 are destabilized compared to Pt (111), which could be explained by the strain effect. In this figure, we can see that the bond lengths between the terrace atoms are about 3.5% less than the normal distance in the Pt bulk. (E) Model D with 3×3 unit cell and 5 layers. Model D is the (OH) bounded Ni single atoms decorated Pt (111) surface. B1 is the most preferred site, then T3, T2 and T1 sites will be covered if more H is adsorbed. Since all the other sites are blocked, T4 will be covered if one more H atom comes in although it's not a local minimum. If higher coverage is reached, the fcc sites and B2 site rather than the top sites will be covered. (F) SANi/Pt model with 3×3 unit cell and 5 layers. This model has no OH groups binding to the Ni, the fcc hollow sites F1 and F2 are the locally stable sites, and they are less active than Pt (111). (G) Model E with 4×4 unit cell and 5 layers. This is another model of Pt (111) with a cavity. (H) Model F with 5×5 unit cell and 5 layers. This is another model of Pt (111) with a cavity. (I) Model G with 3×3 unit cell and 5 layers. Model G is an isomer of model D, which is also (OH) bounded SANi decorated Pt (111) surface, it's 0.027 eV higher in energy. All the sites on this model are also more active than Pt (111).

All the potential adsorption sites for H have been explored on these surfaces, and only the locally stable H structures were considered for evaluating HER activity. To determine which adsorption sites are accessible in the experimental conditions, we explored the occupied adsorption sites as a function of H coverage. The optimal H coverage is determined via first-principle atomistic thermodynamics. The HER activity for all locally stable sites is calculated using a volcano-type kinetic model, which expresses the exchange current i_0 as a function of H adsorption free energy (**Figure 2.9B**).[33] The activity optimum appears for a site with H-binding energy 0.09 eV weaker than that on the hollow sites occupied on Pt (111).[33] This model was first proposed for HER in acidic water, but then proven to be also valid for HER in alkaline water.[9]

The defective surface models of the dealloyed PtNWs show a large distribution of H binding strengths with a rich population of active sites with binding energy near the optimum value (**Figure 2.9B**). Bridge sites on the ridge of the cavities are clearly more stable than hollow sites on Pt (111), but accordingly poorly active for HER. The *fcc* sites on the defective surface models are less stable than those on Pt (111) by 0.03 to 0.1 eV and in the uppermost volcano region. Top sites are not stable on Pt (111) (they diffuse to *fcc* hollow sites), but interestingly they become locally stable both inside the cavity and on the upper terrace close to the ridge on the defective models (see T1 and T2 on model *A* for example). These top sites show a weaker H-binding energy *vs.* hollow sites on Pt (111) and are placed in the highly active zone.

When considering all sites together, the H atoms will first occupy the inactive bridge sites at low coverage, and then occupy the active top and *fcc* hollow sites with increasing coverage. It is hence crucial to determine the H coverage in realistic conditions. The total adsorption free energy at different H coverage is shown in **Figure 2.9B** as a function of the electrode potential *vs.* RHE (U_{RHE}). For model *A*, in pH=14 solution, a low coverage (1/16 ML) is favored for a $U_{RHE} >$ 0.40 V, while below 0.25 V the H coverage strongly rises to 9/16 ML (occupation of 3 B1 sites and 6 B2 sites in **Figure 2.9C**). For a potential below 0.10 V, sites that are more active than Pt (111) begin to be populated (3 F sites, 3 T2 sites and 1 T1 site). At the experimental potential of - 70 mV vs. RHE, a high coverage of 1 ML is reached, with occupation of both active (7/16 ML) and inactive (9/16 ML) sites. The significant density of highly active sites contributes to the high activity of the pure-PtNWs.
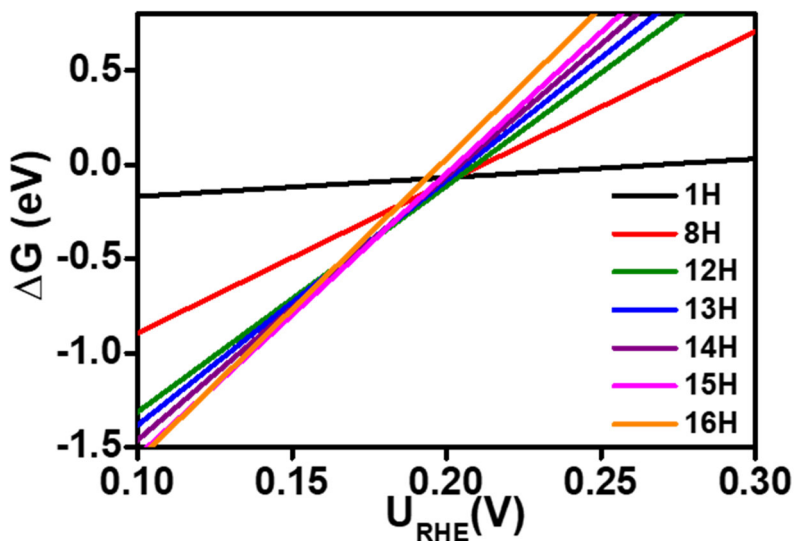
Figure 2.11. Adsorption free energy of hydrogen on a 4×4 unit cell of Pt (111) surface as a function of U_{RHE} at various coverage in pH=14 solution. This figure shows that in the experimental condition of U_{RHE}=0.07 V, the Pt (111) surface adsorbs 1 monolayer of H.

In addition to the models of defective surface, the influence of SANi on the surface is modeled by inserting single Ni atoms in the first layer of a Pt (111) surface. In the considered basic conditions, two OH groups bind with surface Ni atom (**Figure 2.9D**), in line with experimental data (**Figure 2.9E** and **Table 2.3**). **Figure 2.9E** shows the HER activity predicted from the volcano curve for the stable adsorption sites at low and high H coverage conditions. DFT calculations demonstrate that such SANi species electronically modify the Pt atoms in their surroundings, decreasing their H bind energy to the nearly optimal HER activity region. At low coverage condition ($\leq$ 5/9 ML), H adsorbs preferentially on Pt-Ni bridge site B1 (**Figure 2.9D**) and then on the top Pt sites (T1-T4); while at high coverage (>5/9 ML), occupation of bridge sites B1 and B2 together with slightly less stable hollow sites F1-F5 becomes favored over top site occupations (**Figure 2.10E**). Notably, all the sites in the SANi decorated Pt surface as shown in **Figure 2.9D** are more active than those without SANi decoration. At experimental condition (-70 mV *vs*. RHE),

54

the optimal coverage is 5/9 ML (**Figure 2.9F**), which means the B1 bridge site and T1-T4 top sites are occupied by H (black and red marks in **Figure 2.9E**).

Table 2.4. Adsorption free energies for adsorption sites in models A-G (unit: eV).[‡]

model A	ΔΔG	model B	ΔΔG	model C	ΔΔG	model F	ΔΔG
BC	0.341	BC	0.218	B1	0.044	BC	0.235
BS1	-0.180	BS1	-0.118	F1	0.049	BS1	-0.121
BS2	-0.047	BS2	-0.123	F2	0.089	BS2	-0.104
BT1	0.077	BS3	-0.109	F3	0.033	BS3	-0.110
FC	0.349	FC	0.197	F4	0.163	BS4	-0.134
FT1	0.011	FT1	-0.039	F5	0.131	BS5	-0.117
FT2	0.088	FT2	0.066	H1	0.100	FC	0.205
FT3	0.039	FT3	0.115	H2	0.108	FT1	-0.028
HT1	0.105	FT4	0.099	H3	0.087	FT2	0.040
HT2	0.081	HC	0.199	T1	0.151	FT3	0.072
TC	0.161	HT1	0.071	T2	0.087	FT4	0.114
TS1	0.049	HT2	0.137	T3	0.090	FT5	0.017
TS2	0.024	TC	0.116	T4	0.069	FT6	0.017
TT1	0.055	TS1	0.023			FT7	0.073
TT2	0.066	TS2	0.022			FT8	0.082
		TT1	0.088			HC	0.198
		TT2	0.100			HT1	0.075
		TT3	0.049			HT2	0.090
						HT3	0.088
model D	ΔΔG	model E	ΔΔG	model G	ΔΔG	HT4	0.118
B1	0.030	BC	0.241	B1	0.156	HT5	0.123
B2	0.145	BS1	-0.127	B2	0.156	HT6	0.068
B3	0.148	BS2	-0.104	F1	0.111	TC	0.126
B4	0.098	FT1	-0.039	F2	0.112	TS1	0.042

F1	0.127	FT2	0.070	F3	0.096	TS2	0.085
F2	0.097	FT3	0.101	H1	0.126	TT1	0.059
F3	0.175	HC	0.218	H2	0.134	TT2	0.086
F4	0.120	HT1	0.068	T1	0.091	TT3	0.091
F5	0.100	HT2	0.118	T2	0.072	TT4	0.061
H1	0.146	TS1	0.035	T3	0.071	TT5	0.083
H2	0.142	TS2	0.020			TT6	0.103
T1	0.108	TT1	0.033				
T2	0.087	TT2	0.080				
T3	0.042						
T4	0.120						

[‡]The adsorption free energy is expressed in $\Delta G_H - \Delta G_H^{Pt\,(111)}$ ($\Delta\Delta G$), which is the difference between the actual free energy ΔG_H and the adsorption free energy on Pt (111) surface $\Delta G_H^{Pt\,(111)}$.

One should note that the OH ligands are crucial for the enhanced HER activity: a single bare Ni atom does not produce this favorable electronic modification (**Figure 2.10F**). All the additional DFT models and the adsorption free energies for all the models are shown in **Figure 2.10G-I**, **Figure 2.11** and **Table 2.3** respectively. It is important to note that the SANi species only significantly enhances the nearest neighboring Pt sites. In this regard, the surface decoration by the well-distributed SANi is indeed highly desired for generating most activated Pt sites without unnecessarily blocking too many Pt sites to achieve optimized mass activity. Larger clusters of nickel species would have much fewer neighboring Pt sites and also block more surface Pt sites (**Figure 2.1B**).

2.6 MOR/EOR Activities of the SANi-PtNWs

To further explore the SANi-PtNWs as multifunctional electrocatalysts, we have evaluated their performance for methanol oxidation reactions (MOR) and ethanol oxidation reactions (EOR). The SANi-PtNWs were prepared in the same way as those described in the HER experiments. The MOR test was conducted in aqueous electrolyte with 1 M methanol and 1 M KOH. Cyclic voltammetry (CV) with a scan rate of 20 mV/s were used to evaluate catalytic properties of the SANi-PtNWs and compared with that of the pure-PtNWs and the Pt/C under the same test conditions. Importantly, the Pt mass normalized CV curve shows a peak current density of 7.93 ± 0.45 A/mg$_{Pt}$ at 0.816 V *vs.* RHE (**Figure 2.12A**), more than 7 and 2 times those of the commercial Pt/C (1.04 A/mg$_{Pt}$) and the pure-PtNWs (3.87 A/mg$_{Pt}$), respectively. Additionally, a 144 mV decrease of the onset overpotential (defined as overpotential required to reach a mass activity reach of 0.1 A/mg$_{Pt}$) is observed in the SANi-PtNWs when compared with that of Pt/C, suggesting the lower activation barrier of methanol oxidation on the SNAi-PtNWs surface (**Figure 2.12A**). Similarly, the EOR test in 1 M ethanol/1 M KOH solution shows a peak mass activity of 5.60 ± 0.27 A/mg$_{Pt}$ at 0.785V *vs.* RHE for the SANi-PtNWs (**Figure 2.12B**), which is more than 7 and 3 times higher than those of the Pt/C and the pure-PtNWs, respectively. Additionally, a 61 mV decrease of the onset overpotential is also observed for the SANi-PtNWs vs. Pt/C reference.
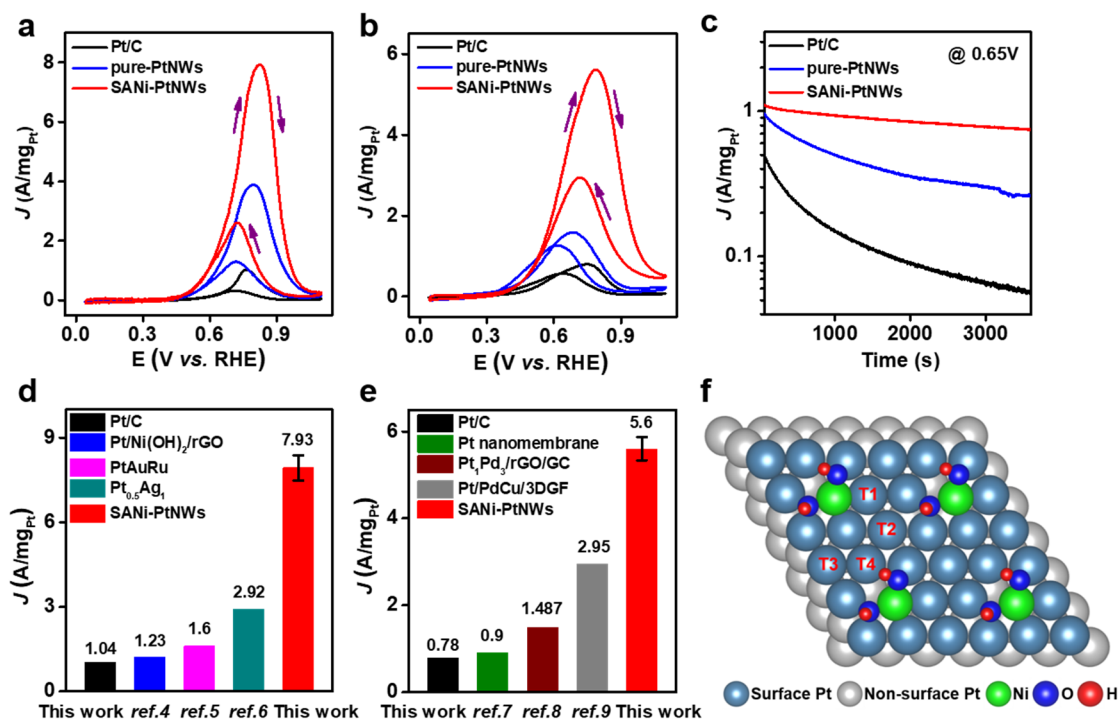
Figure 2.12. MOR and EOR electrocatalytic activities of the SANi-PtNWs, pure-PtNWs, and Pt/C in 1 M KOH electrolyte. (**A**) The MOR CVs under sweeping rate of 20 mV/s, the concentration of methanol is 1 M. (**B**) The EOR CVs under sweeping rate of 20 mV/s, the concentration of ethanol is 1 M. (**C**) The chronoamperometry MOR test at the potential of 0.65 V vs. RHE. (**D**) The MOR and (**E**) EOR peak mass activity compared with the state-of-art values reported recently. Error bars in D and E indicate the standard deviation of ten independent samples. *The material in ref. 6 was tested in 0.5 M KOH and 2 M methanol, and that in ref. 8 was tested in 0.5 M NaOH. (**f**) Model D for SANi decorated Pt (111) surface with different CO adsorption sites labeled as T1, T2, T3 and T4.

The chronoamperometry (CA) tests were used to evaluate the stability of SANi-PtNWs, pure-PtNWs and Pt/C in MOR (**Figure 2.12C**). Apparently, the MOR activity of the Pt/C benchmark material shows a rather rapid decay to 0.056 A/mg$_{Pt}$ after 3600 s CA test at 0.650V *vs.* RHE. In contrast, the SANi-PtNWs shows a relatively stable mass activity 0.76 A/mg$_{Pt}$ after 3600 s CP test under the same conditions, clearly demonstrating the superior stability of SANi-PtNWs catalysts

when compared to the Pt/C. The pure-PtNWs also show a faster activity decay to 0.26 A/mg$_{Pt}$ after

3600 s CA test (*vs.* 0.76 A/mg$_{Pt}$ for the SANi-PtNWs). The studies demonstrate that the SANi

decoration not only boosts the activity but also improves durability.
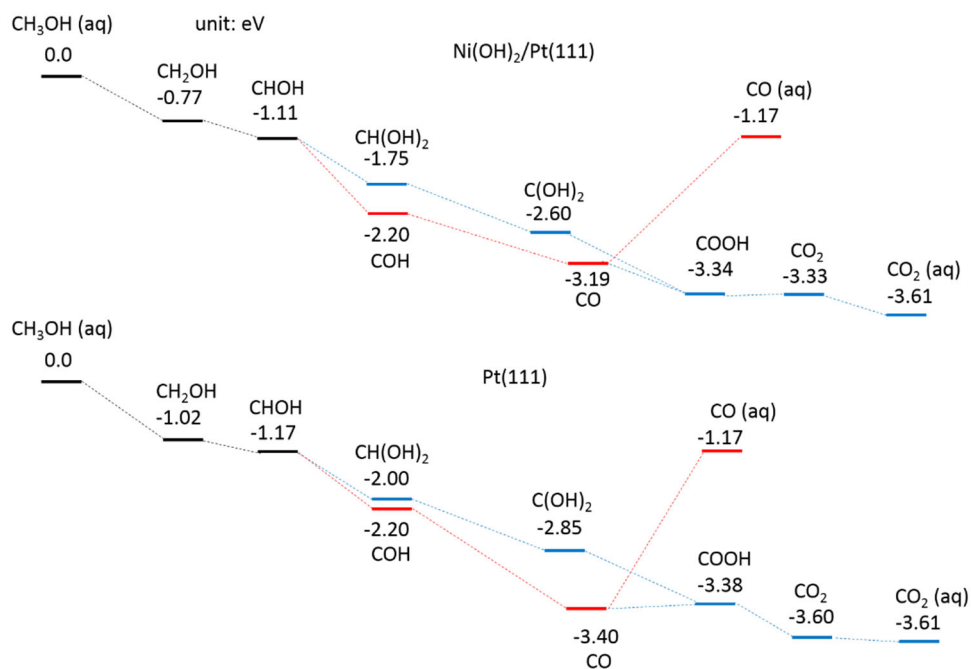
Figure 2.13. Reaction profile for MOR on Ni(OH)$_2$/Pt(111) (top) and Pt(111) (bottom). A continuum

solvent model with dielectric constant 78.4 was used, together with a potential of 0.65 V vs. RHE.

We have further conducted DFT calculations to probe the origin of activity/stability

enhancement by SANi decoration. A major path for catalyst deactivation in MOR is the poisoning

by CO intermediates. On the model D consisting of a Ni(OH)$_2$ decorated Pt (111) surface (**Figure

2.12F**), the DFT calculations clearly indicate that all steps in the reaction pathway are exothermic

at the experimental potential (**Figure 2.13**) and that the CO adsorption on SANi-modified Pt top

sites is 0.06 eV – 0.28 eV weaker than that on Pt (111) top site **Table 2.4** and **Figure 2.12F**), hence

facilitating the final step conversion from CO to CO$_2$. Furthermore, we have conducted CO

stripping experiments to probe the CO binding strength of different catalysts (**Figure. 2.14**). The

CO stripping experiments show that the SANi-PtNWs exhibit a 52 mV and 88 mV decrease of the onset potential, and 8 mV and 38 mV decrease of CO oxidation peak potential compared to the cases of pure-PtNWs and Pt/C respectively. These results are largely consistent with the DFT calculations and suggest that the enhanced activity and durability for MOR/EOR could be at least partly attributed to the change in CO binding strength upon SANi modification, hence effectively mitigating catalyst poisoning issue. This understanding further demonstrates the exciting potential of the single-atom tailoring in modifying the kinetics of MOR or EOR.

Table 2.5. CO adsorption energies for adsorption sites are shown in **Figure 2.12F**.

Adsorption site	$\Delta E/eV$
Pt (111)	-1.77
T1	-1.54
T2	-1.64
T3	-1.71
T4	-1.69

Comparing with the state-of-art Pt or PtRu-based MOR catalysts tested under the same conductions, the SANi-PtNWs catalysts show the highest specific activity and mass activity reported to date, to the best of our knowledge, with the mass activity achieved in the SANi-PtNWs catalysts ~3-6 times of the state-of-art values reported recently (**Figure 2.12D**). Comparing with all EOR catalysts reported to date, the SANi-PtNWs also show a considerable advantage in mass activity (**Figure 2.12E**), about 2-6 times the best values reported recently. Together, these studies clearly demonstrate that SANi tailored pure-PtNWs presents a major leap for both MOR and EOR, offering significant potential for future alkaline anion exchange membrane fuel cell development.
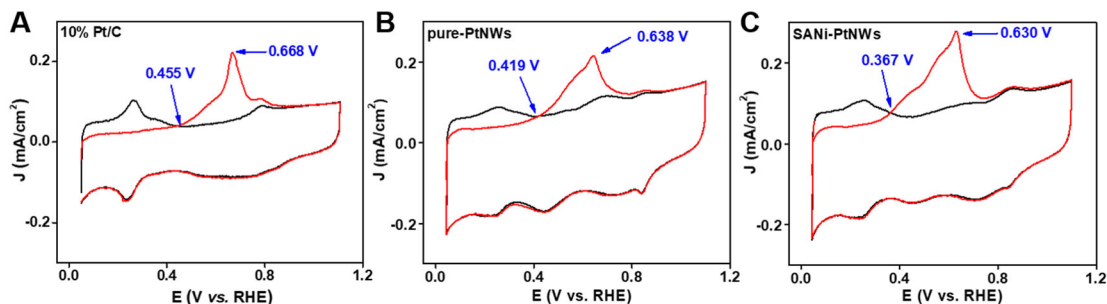
Figure 2.14. The CO stripping results for (A) 10% Pt/C, (B) pure-PtNWs, and (c) SANi-PtNWs. The measurements were conducted in 1 M KOH at the scan rate of 25 mV/s.

2.7 Conclusion

Together, we have designed an effective approach to tailor Pt nanocatalysts with single atomic nickel (SANi) species. By combining XANES, EXAFS analyses with atomic-scale STEM and EELS mapping studies, we verify that the PtNWs surface was successfully modified with surface SANi. The electrocatalytic test revealed that the resulting SANi modified Pt nanocatalysts exhibit considerably improved HER performance when compared with the state-of-art HER catalysts. Density functional theory calculations demonstrate that the single Ni atoms, liganded by two hydroxyl groups, electronically promote the neighboring Pt atoms and enhance their activity towards HER. Our studies suggest that an optimum decoration density (surface Ni:Pt ratio ~1:6) is critical for maximizing specific activity while retaining a high ECSA. This decoration density can be readily tuned, in a fully repeatable way, by our gradual dealloying process but is difficult to achieve with other direct synthetic approaches. Additional MOR and EOR electro-catalytic studies further demonstrate greatly improved mass activities for these reactions. It is important to note that the mass activities achieved in SANi-PtNWs not merely surpass previous works, but also represent a conceptual advance over the state-of-art, with the Pt mass activities for HER, MOR and EOR about 4-20, 3-6, and 2-6 times higher than the state-of-art values reported recently.

Our previous studies have shown that the fully dealloyed pure-PtNWs show high activity for ORR,[10] which can be largely attributed to their defective surface featuring rich atomic vacancies and strain.[34-36] As we demonstrated with pure-PtNWs both experimentally and theoretically, these surface features can also contribute to improved activity for HER, MOR and EOR when compared with Pt/C reference. Taking a step further, the current study further explores single atom decoration as a general strategy for tailoring the local electronic structure of Pt catalysts to achieve further enhanced specific activity for a series of technological relevant electrochemical reactions at little or no sacrifice of the surface area and thus delivering optimized mass activity that is critical for practical applications. The significant enhancement of mass activity for various electrocatalytic systems clearly demonstrates that the surface decoration with single atoms offers an effective and general strategy for tailoring precious metal catalysts for diverse reactions. This strategy of single-atom decoration, by interrupting dealloying, can be expected to apply to other dopant elements such as Fe, Co or Cu species.

We should also note that the single-atom tailoring of Pt nanocatalysts is also conceptually distinct from typical single-atom catalysts intensively explored recently. In a typical single-atom catalyst, single metallic atoms are often dispersed on a host substrate with the single metal atoms functioning as the primary active sites.[37-40] To the opposite, in our case, single metal atoms decorate the surface of precious metal Pt catalysts to modify the local atomic configuration and electronic structures of surrounding Pt atoms, thus tailoring their catalytic activity for specific reactions. Here single metal atoms are not the primary active sites but play a critical role as a promoter to enhance the activity of the Pt-based catalysts without significantly blocking the surface active sites, thus defining a general strategy for creating multifunctional electrocatalysts with optimized surface area, specific activity, and mass activity at the same time.

2.7 Reference

1   Yin, H., Zhao, S., Zhao, K., Muqsit, A., Tang, H., Chang, L., Zhao, H., Gao, Y. & Tang, Z. Ultrathin platinum nanowires grown on single-layered nickel hydroxide with high hydrogen evolution activity. *Nat. Commun.* **6**, 6430 (2015).

2   Wang, P., Zhang, X., Zhang, J., Wan, S., Guo, S., Lu, G., Yao, J. & Huang, X. Precise tuning in platinum-nickel/nickel sulfide interface nanowires for synergistic hydrogen evolution catalysis. *Nat. Commun.* **8**, 14580 (2017).

3   Cao, Z., Chen, Q., Zhang, J., Li, H., Jiang, Y., Shen, S., Fu, G., Lu, B.-a., Xie, Z. & Zheng, L. Platinum-nickel alloy excavated nano-multipods with hexagonal close-packed structure and superior activity towards hydrogen evolution reaction. *Nat. Commun.* **8**, 15131 (2017).

4   Huang, W., Wang, H., Zhou, J., Wang, J., Duchesne, P. N., Muir, D., Zhang, P., Han, N., Zhao, F. & Zeng, M. Highly active and durable methanol oxidation electrocatalyst based on the synergy of platinum–nickel hydroxide–graphene. *Nat. Commun.* **6**, 10035 (2015).

5   Ren, F., Wang, C., Zhai, C., Jiang, F., Yue, R., Du, Y., Yang, P. & Xu, J. One-pot synthesis of a RGO-supported ultrafine ternary PtAuRu catalyst with high electrocatalytic activity towards methanol oxidation in alkaline medium. *J. Mater. Chem. A* **1**, 7255-7261 (2013).

6   Feng, Y.-Y., Bi, L.-X., Liu, Z.-H., Kong, D.-S. & Yu, Z.-Y. Significantly enhanced electrocatalytic activity for methanol electro-oxidation on Ag oxide-promoted PtAg/C catalysts in alkaline electrolyte. *J. Catal.* **290**, 18-25 (2012).

7   Wu, H., Li, H., Zhai, Y., Xu, X. & Jin, Y. Facile Synthesis of Free-Standing Pd-Based Nanomembranes with Enhanced Catalytic Performance for Methanol/Ethanol Oxidation. *Adv. Mater.* **24**, 1594-1597 (2012).

8   Ren, F., Wang, H., Zhai, C., Zhu, M., Yue, R., Du, Y., Yang, P., Xu, J. & Lu, W. Clean method for the synthesis of reduced graphene oxide-supported PtPd alloys with high electrocatalytic activity for ethanol oxidation in alkaline medium. *ACS Appl. Mater. Interfaces* **6**, 3607-3614 (2014).

9   Danilovic, N., Subbaraman, R., Strmcnik, D., Chang, K. C., Paulikas, A., Stamenkovic, V. & Markovic, N. M. Enhancing the alkaline hydrogen evolution reaction activity through the bifunctionality of Ni (OH) 2/metal catalysts. *Angew. Chem.* **124**, 12663-12666 (2012).

10   Li, M., Zhao, Z., Cheng, T., Fortunelli, A., Chen, C.-Y., Yu, R., Zhang, Q., Gu, L., Merinov, B. V. & Lin, Z. Ultrafine jagged platinum nanowires enable ultrahigh mass activity for the oxygen reduction reaction. *Science* **354**, 1414-1419 (2016).

11   Chen, C., Kang, Y., Huo, Z., Zhu, Z., Huang, W., Xin, H. L., Snyder, J. D., Li, D., Herron, J. A. & Mavrikakis, M. Highly crystalline multimetallic nanoframes with three-dimensional electrocatalytic surfaces. *Science* **343**, 1339-1343 (2014).

12   Choi, S.-I., Xie, S., Shao, M., Odell, J. H., Lu, N., Peng, H.-C., Protsailo, L., Guerrero, S., Park, J. & Xia, X. Synthesis and characterization of 9 nm Pt–Ni octahedra with a record high activity of 3.3 A/mgPt for the oxygen reduction reaction. *Nano Lett.* **13**, 3420-3425 (2013).

13   Zhang, Z., Liu, G., Cui, X., Chen, B., Zhu, Y., Gong, Y., Saleem, F., Xi, S., Du, Y. & Borgna, A. Crystal Phase and Architecture Engineering of Lotus‐Thalamus‐Shaped Pt‐Ni Anisotropic Superstructures for Highly Efficient Electrochemical Hydrogen Evolution. *Adv. Mater.*, **30**, 1801741 (2018).

14   Zhang, Z., Luo, Z., Chen, B., Wei, C., Zhao, J., Chen, J., Zhang, X., Lai, Z., Fan, Z. & Tan, C. One‐Pot Synthesis of Highly Anisotropic Five‐Fold‐Twinned PtCu Nanoframes Used as a Bifunctional Electrocatalyst for Oxygen Reduction and Methanol Oxidation. *Adv. Mater.* **28**, 8712-8717 (2016).

15   Zhang, L., Roling, L. T., Wang, X., Vara, M., Chi, M., Liu, J., Choi, S.-I., Park, J., Herron, J. A. & Xie, Z. Platinum-based nanocages with subnanometer-thick walls and well-defined, controllable facets. *Science* **349**, 412-416 (2015).

16   van der Vliet, D. F., Wang, C., Li, D., Paulikas, A. P., Greeley, J., Rankin, R. B., Strmcnik, D., Tripkovic, D., Markovic, N. M. & Stamenkovic, V. R. Unique Electrochemical Adsorption Properties of Pt‐Skin Surfaces. *Angew. Chem.* **124**, 3193-3196 (2012).

17   Cui, C., Gan, L., Heggen, M., Rudi, S. & Strasser, P. Compositional segregation in shaped Pt alloy nanoparticles and their structural behaviour during electrocatalysis. *Nat. Mater.* **12**, 765-771 (2013).

18   Zhang, J., Lima, F., Shao, M., Sasaki, K., Wang, J., Hanson, J. & Adzic, R. Platinum monolayer on nonnoble metal− noble metal core−shell nanoparticle electrocatalysts for O2 reduction. *J. Phys. Chem. B* **109**, 22701-22704 (2005).

19   Fu, X.-Z., Liang, Y., Chen, S.-P., Lin, J.-D. & Liao, D.-W. Pt-rich shell coated Ni nanoparticles as catalysts for methanol electro-oxidation in alkaline media. *Catal. Commun.* **10**, 1893-1897 (2009).

20   Calle-Vallejo, F., Tymoczko, J., Colic, V., Vu, Q. H., Pohl, M. D., Morgenstern, K., Loffreda, D., Sautet, P., Schuhmann, W. & Bandarenka, A. S. Finding optimal surface sites on heterogeneous catalysts by counting nearest neighbors. *Science* **350**, 185-189 (2015).

21   Calle-Vallejo, F., Pohl, M. D., Reinisch, D., Loffreda, D., Sautet, P. & Bandarenka, A. S. Why conclusions from platinum model surfaces do not necessarily lead to enhanced nanoparticle catalysts for the oxygen reduction reaction. *Chem. Sci.* **8**, 2283-2289 (2017).

22   Huang, X., Zhao, Z., Cao, L., Chen, Y., Zhu, E., Lin, Z., Li, M., Yan, A., Zettl, A. & Wang, Y. M. High-performance transition metal–doped Pt3Ni octahedra for oxygen reduction reaction. *Science* **348**, 1230-1234 (2015).

23   Strasser, P., Koh, S., Anniyev, T., Greeley, J., More, K., Yu, C., Liu, Z., Kaya, S., Nordlund, D. & Ogasawara, H. Lattice-strain control of the activity in dealloyed core–shell fuel cell catalysts. *Nat. Chem.* **2**, 454-460 (2010).

24   Cui, C., Gan, L., Li, H.-H., Yu, S.-H., Heggen, M. & Strasser, P. Octahedral PtNi nanoparticle catalysts: exceptional oxygen reduction activity by tuning the alloy particle surface composition. *Nano Lett.* **12**, 5885-5889 (2012).

25   Subbaraman, R., Tripkovic, D., Chang, K.-C., Strmcnik, D., Paulikas, A. P., Hirunsit, P., Chan, M., Greeley, J., Stamenkovic, V. & Markovic, N. M. Trends in activity for the water

electrolyser reactions on 3d M (Ni, Co, Fe, Mn) hydr (oxy) oxide catalysts. *Nat. Mater.* **11**, 550-557 (2012).

26   Jiang, Q., Jiang, L., Wang, S., Qi, J. & Sun, G. A highly active PtNi/C electrocatalyst for methanol electro-oxidation in alkaline media. *Catal. Commun.* **12**, 67-70 (2010).

27   Subbaraman, R., Tripkovic, D., Strmcnik, D., Chang, K.-C., Uchimura, M., Paulikas, A. P., Stamenkovic, V. & Markovic, N. M. Enhancing hydrogen evolution activity in water splitting by tailoring Li+-Ni (OH) 2-Pt interfaces. *Science* **334**, 1256-1260 (2011).

28   Lytle, F. W. Determination of d-band occupancy in pure metals and supported catalysts by measurement of the LIII X-ray absorption threshold. *J. Catal.* **43**, 376-379 (1976).

29   Pearson, D., Ahn, C. & Fultz, B. White lines and d-electron occupancies for the 3d and 4d transition metals. *Phys. Rev. B* **47**, 8471-8478 (1993).

30   Becknell, N., Kang, Y., Chen, C., Resasco, J., Kornienko, N., Guo, J., Markovic, N. M., Somorjai, G. A., Stamenkovic, V. R. & Yang, P. Atomic structure of Pt3Ni nanoframe electrocatalysts by in situ X-ray absorption spectroscopy. *J. Am. Chem. Soc.* **137**, 15817-15824 (2015).

31   Burke, M. S., Enman, L. J., Batchellor, A. S., Zou, S. & Boettcher, S. W. Oxygen evolution reaction electrocatalysis on transition metal oxides and (oxy) hydroxides: activity trends and design principles. *Chem. Mater.* **27**, 7549-7558 (2015).

32   Bates, M. K., Jia, Q., Doan, H., Liang, W. & Mukerjee, S. Charge-transfer effects in Ni–Fe and Ni–Fe–Co mixed-metal oxides for the alkaline oxygen evolution reaction. *ACS Catal.* **6**, 155-161 (2015).

33   Nørskov, J. K., Bligaard, T., Logadottir, A., Kitchin, J., Chen, J. G., Pandelov, S. & Stimming, U. Trends in the exchange current for hydrogen evolution. *J. Electrochem. Soc.* **152**, J23-J26 (2005).

34   Le Bacq, O., Pasturel, A., Chattot, R., Previdello, B., Nelayah, J., Asset, T., Dubau, L. & Maillard, F. Effect of Atomic Vacancies on the Structure and the Electrocatalytic Activity of Pt-rich/C Nanoparticles: A Combined Experimental and Density Functional Theory Study. *ChemCatChem* **9**, 2324-2338 (2017).

35   Chattot, R. l., Asset, T., Bordet, P., Drnec, J., Dubau, L. & Maillard, F. d. r. Beyond Strain and Ligand Effects: Microstrain-Induced Enhancement of the Oxygen Reduction Reaction Kinetics on Various PtNi/C Nanostructures. *ACS Catal.* **7**, 398-408 (2016).

36   Chattot, R., Le Bacq, O., Beermann, V., Kühl, S., Herranz, J., Henning, S., Kühn, L., Asset, T., Guétaz, L. & Renou, G. Surface distortion as a unifying concept and descriptor in oxygen reduction reaction electrocatalysis. *Nat. Mater.* **17**, 827-834 (2018).

37   Fei, H., Dong, J., Feng, Y., Allen, C. S., Wan, C., Volosskiy, B., Li, M., Zhao, Z., Wang, Y. & Sun, H. General synthesis and definitive structural identification of MN 4 C 4 single-atom catalysts with tunable electrocatalytic activities. *Nat. catal.* **1**, 63-72 (2018).

38   Marcinkowski, M. D., Darby, M. T., Liu, J., Wimble, J. M., Lucci, F. R., Lee, S., Michaelides, A., Flytzani-Stephanopoulos, M., Stamatakis, M. & Sykes, E. C. H. Pt/Cu single-atom alloys as coke-resistant catalysts for efficient C–H activation. *Nat. Chem.* **10**, 325-332 (2018).

39   Back, S., Lim, J., Kim, N.-Y., Kim, Y.-H. & Jung, Y. Single-atom catalysts for CO 2 electroreduction with significant activity and selectivity improvements. *Chem. Sci.* **8**, 1090-1096 (2017).

40   Zhang, H., Liu, G., Shi, L. & Ye, J. Single‑Atom Catalysts: Emerging Multifunctional Materials in Heterogeneous Catalysis. *Adv. Energy Mater.* **8**, 1701343(2018).

41   Kresse, G. & Hafner, J. Ab initio molecular dynamics for liquid metals. *Physical Review B* **47**, 558-561 (1993).

42   Kresse, G. & Hafner, J. Ab initio molecular-dynamics simulation of the liquid-metal–amorphous-semiconductor transition in germanium. *Physical Review B* **49**, 14251-14269 (1994).

43   Perdew, J. P., Burke, K. & Ernzerhof, M. Generalized gradient approximation made simple. *Physical review letters* **77**, 3865-3868 (1996).

44   Hansen, M. H., Jin, C., Thygesen, K. S. & Rossmeisl, J. Finite Bias Calculations to Model Interface Dipoles in Electrochemical Cells at the Atomic Scale. *The Journal of Physical Chemistry C* **120**, 13485-13491 (2016).

CHAPTER 3. TAILORING THE PT SURFACE OXOPHILICITY VIA SINGLE ATOM RH DOPING FOR BOOSTING HYDROGEN OXIDATION REACTION IN ALKALINE ELECTROLYTE

3.1 Introduction

Hydrogen fuel cells, which can directly convert hydrogen gas (H_2) and oxygen gas (O_2) into electricity and only release water, have been rapidly developed for replacing the internal combustion engine used in vehicles. Because of the high commercialization level of the proton exchange membrane (PEM), the design of current state-of-the-art fuel cells is all based on the PEM which serves as the solid electrolyte. However, the high acidity of PEM requires a huge amount of expensive Pt-based catalysts for oxygen reduction reaction (ORR) and thus limits the widespread adoption of fuel cell electric vehicles. In acidic condition, the anode hydrogen oxidation reaction is a rapid process and only need a small amount of Pt catalysts. However, the sluggish cathode ORR can only be accelerated using a high amount of Pt catalysts, which account for approximately 55% of the cost of the fuel cell stacks. Recently, because of the rapid development of the anion exchange membrane (AEM) with the greatly enhanced anion exchange rate and durability, AEM fuel cells (AEMFCs) show a more promising future on the commercialization of low cost and long-term stable FCEVs.[1,2] AEM features an alkaline electrolyte, where non-precious metal ORR catalysts possess high ORR activity and can replace Pt catalysts. Although Pt is still the best selection for HOR catalysts in the alkaline medium, The HER/HOR activity of Pt is highly pH-dependent and decreases over two orders of magnitude when pH increases from 1 to 14.[3] Thus, the sluggish HER/HOR reaction in the alkaline electrolyte becomes the most critical issue in developing AEMFCs and alkaline water electrolytic devices. The slow HER/HOR in the alkaline electrolyte has been mainly ascribed to the positive shift of

potential of zero free charge (PZFC) while increasing the pH value of electrolyte.[4-6] As PZFC shifts to a more positive value vs. RHE, it becomes more difficult for $H_2O_{\downarrow}$/OH_{ads} to adsorb on the Pt surface, which hinders H_2O dissociation in HER or the removal of H_{ads} in HOR.[6]
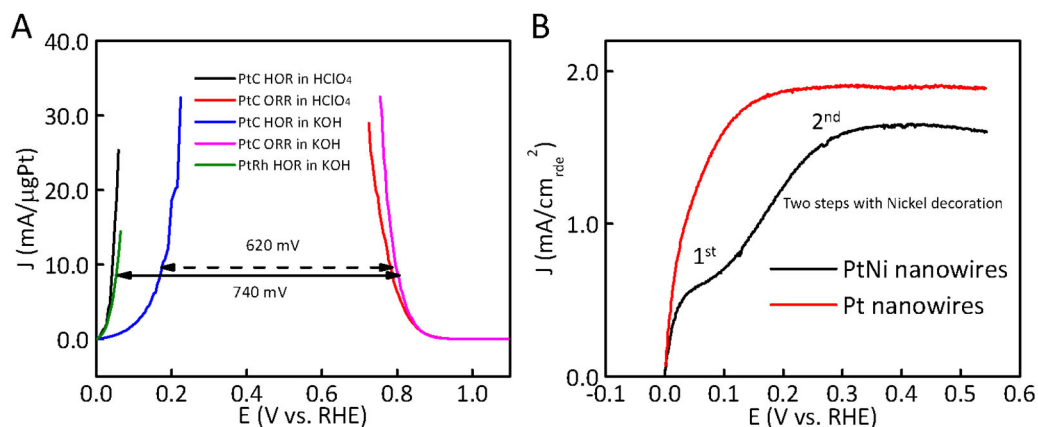
Figure 3.1. (A) Activity discrepancy of Pt/C in 0.1 M HClO$_4$ and 1.0 M KOH, and the mass activity of PtRh based nanowires in 1 M KOH is comparable with the mass activity of Pt/C in 0.1 M acid (B) Conventional Ni decoration will lead to obvious plateau region after 30 mV vs. RHE.

Tailoring Pt surface with a second transition metal hydroxides (*e.g.,* Ni(OH)$_2$, Ru. etc.) has been proved to be an effective method to boost the HER/HOR activity on Pt.[7-9] Such surface decoration improves the Pt surface oxophilicity and leads to the enhanced adsorption of $H_2O_{\downarrow}$ on the surface. The interaction between the O atoms in the $H_2O_{\downarrow}$ and H_{ads} on Pt surface facilitates the removal of the H_{ads} and thus accelerates the HOR rate.[10-12] In the case of HER, the water dissociation is the rate-determining step (rds) in the alkaline condition. With higher surface oxophilicity, the $H_2O_{\downarrow}$ will get readily adsorbed on the surface with the configuration that the O atom stays on the transition metal site and one H atom stays on the neighboring Pt site.[6,11] Such configuration weakens the H-OH bond and thus facilitates the water dissociation step and enhances the HER activity. (**Figure 3.1**) Therefore, the surface oxophilicity enhancement resulted from the

surface decoration is vital for tuning the HER/HOR activity in the alkaline condition.[11] However, these surface decorations come at the sacrifice of active surface Pt sites, leading to decreased electrochemical surface area (ECSA) and hence mass activity (MA). Also, current surface tailoring strategies lack the fine control of the decorated species and distribution, thus limiting the understanding of the relationship between Pt surface and HER/HOR kinetics. **Thus, how to effectively tune the Pt surface oxophilicity is critical in enhancing the surface HER/HOR kinetics and developing the theoretical study**. Herein, taking advantage of the single-atom tailoring strategy, we have achieved single Rh atom tailoring of Pt nanowires for the optimization of surface oxophilicity for OH adsorption to boost the HOR activity in alkaline condition.

3.2 Experimental Section

Synthesis of PtRh NWs. All chemicals were purchased from Sigma-Aldrich unless otherwise specified. In a typical synthesis, 20 mg Pt(acac)$_2$ and the desired amount of Rh(acac)$_3$ (2mg, 5mg, 10 mg, 20mg, 30 mg, and 40 mg) were mixed with 130 mg glucose, 1.7 mg W(CO)$_6$ and 60 mg PVP-40 in a glass vial, with 5 ml of oleylamine and octadecene (3:2 volume ratio) as co-solvent. The mixture was heated to 140 ºC for 8 hours to form PtRh nanowires. The result nanowires were collected via centrifuge at 12000 rpm for 20 min.

Material Characterizations. Transmission electron microscopy (TEM) images were taken on an FEI T12 operated at 120 kV. Atomic resolution high-angle annular dark-field scanning transmission electron microscopy (HAADF-STEM) images and X-ray energy dispersive spectroscopy (EDS) mapping were taken on FEI Titan Cubed Themis G2 300 at 200 kV and JEOL Grand ARM 300CF TEM/STEM with double spherical aberration-correctors operated at 300 kV. Samples for TEM measurements were prepared by dropping 10-20 μL nanoparticle dispersion in hexane on a carbon-coated copper grid (Ladd Research, Williston, VT). The composition of

catalysts was determined by inductively coupled plasma atomic emission spectroscopy (ICP- AES, Shimadzu ICPE-9000) as well as SEM-EDS (JEOL JSM-6700F FE-SEM). X-ray photoelectron spectroscopy (XPS) tests were done with Kratos AXIS Ultra DLD spectrometer. The *in-situ* X-ray absorption fine structure spectra for Ni K-edge and Pt L-edge EXAFS The electrode inks for the XAS electrodes were collected in the fluorescence mode at the beamlines of X3B and X19A at the National Synchrotron Light Source (NSLS) (Brookhaven National Laboratory, NY, USA). All of the experimental data were collected in conjunction with the appropriate reference foils to aid in energy alignment and normalization. The data were processed and fitted using the Ifeffit-based Athena and Artemis programs. Scans were calibrated, aligned, and normalized with background removed using the IFEFFIT suite. The $\chi(R)$ were modeled using single scattering paths calculated by FEFF6. The $\Delta\mu$-XANES analysis technique has been described in great detail elsewhere. Briefly, difference spectra were calculated using the equation

$$\Delta\mu = \mu(V) - \mu(V1, N_2)$$

where $\mu(V)$ is the absorption coefficient of the sample at a potential of interest and $\mu(V1, N_2)$ is the reference signal at V1 potential, which is in the regular clean double-layer region for the tested metal, i.e., free of any adsorbed H, O(H), or oxygen adsorbates.

3.3 Results and Discussion

By tuning the mass ratio between Rh(acac)$_3$ and Pt(acac)$_2$ to be 2:20. 5:20, and 10:20, 20:20, 30:20, 40:20, PtRh nanowires with a different surface concentration of Rh were successfully synthesized. Based on the HAADF-STEM EDS mapping, the surface Rh concentration increases with the increased ratio of Rh:Pt.
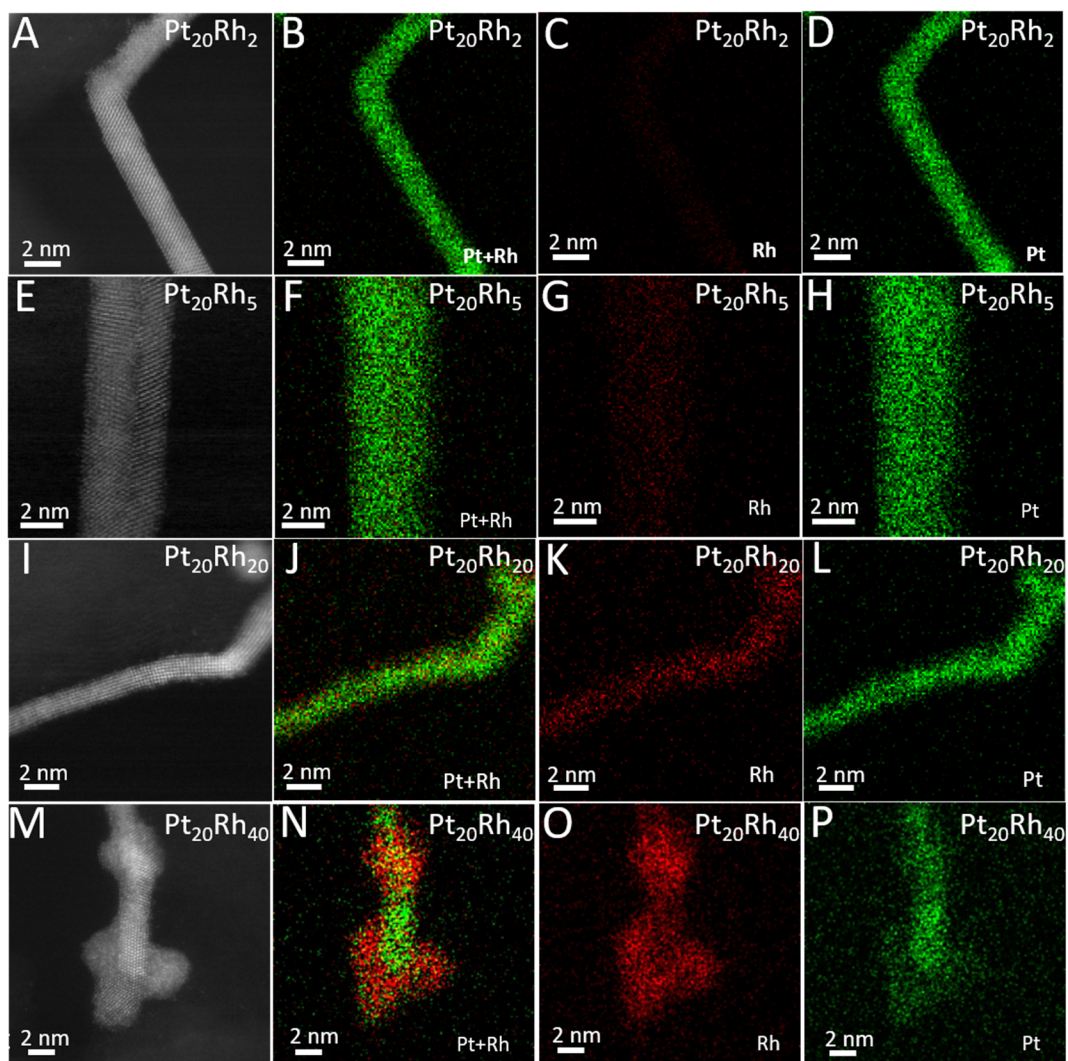
Figure 3.2. Representative HAADF-STEM images and corresponding EDS mapping of Ru, Pt, and Pt+Rh for (A-D) $Pt_{20}Rh_2$, (E-H) $Pt_{20}Rh_5$, (I-L) $Pt_{20}Rh_{20,}$ and (M-P) $Pt_{20}Rh_{40}$ nanowires.

When the Rh/Pt ratio is as low as 2:20, there are barely any Rh atoms observed on the surface. Rh atoms only occupy 5 at% of the whole nanowires and most of them are on the sublayer of Pt nanowires. (**Figure 3.2A-D**) When the Rh/Pt ratio goes up to 5:20, the nanowires' surface is still domain by Pt, but with singly dispersed Rh atom (~ 10 %) on the surface (**Figure3.2 E-H**). The existence of single atom Rh in the whole range of the HOR region is proved by the ex-situ and in-situ extended X-Ray absorption fine structure (**Figure 3.3**). No Rh-Rh bonding was observed from

0 V to 0. 54 V vs. RHE, the range where HOR takes place. When the ratio goes above 20:20, the Rh atoms start to aggregate on the surface of Pt nanowires and induce side-growth of Rh rich branches that cover Pt nanowires (**Figure 3.2 I-P**).
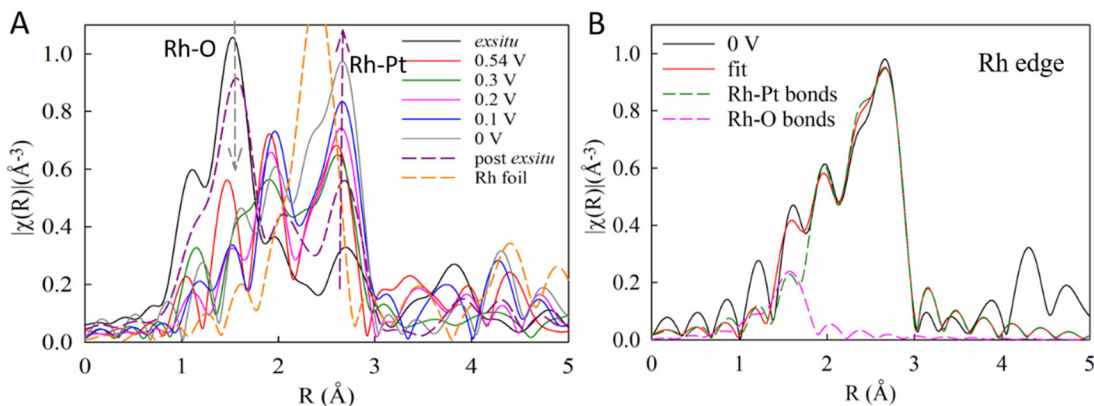
Figure 3.3. (A) *In-situ* Rh K edge EXAFS spectra of $Pt_{20}Rh_5$ nanowires under different potential. (A) Fitting *of in- situ* Rh K edge EXAFS spectra of $Pt_{20}Rh_5$ nanowires at 0 V vs. RHE.

Interestingly, the HOR activity of PtRh nanowires is highly sensitive to the oxophilicity of Pt surface and the structure of surface Rh species. Pt surface with higher oxophilicity usually shows a higher HER/HOR rate in alkaline condition because the sluggish Volmer step can be accelerated by the early adsorption of OH in the H_{upd} potential region. It was observed that the CO oxidation peak continuously shifts to negative potential when increasing the surface Rh concentration (**Figure 3.4A**), indicating that the oxophilicity of the Pt surface has a positive correlation with surface Rh concentration. However, both the HOR specific activity and the exchange current density of the PtRh nanowires reach the maximum value only when the Rh is in the single-atom form (**Figure 3.4B-D**).
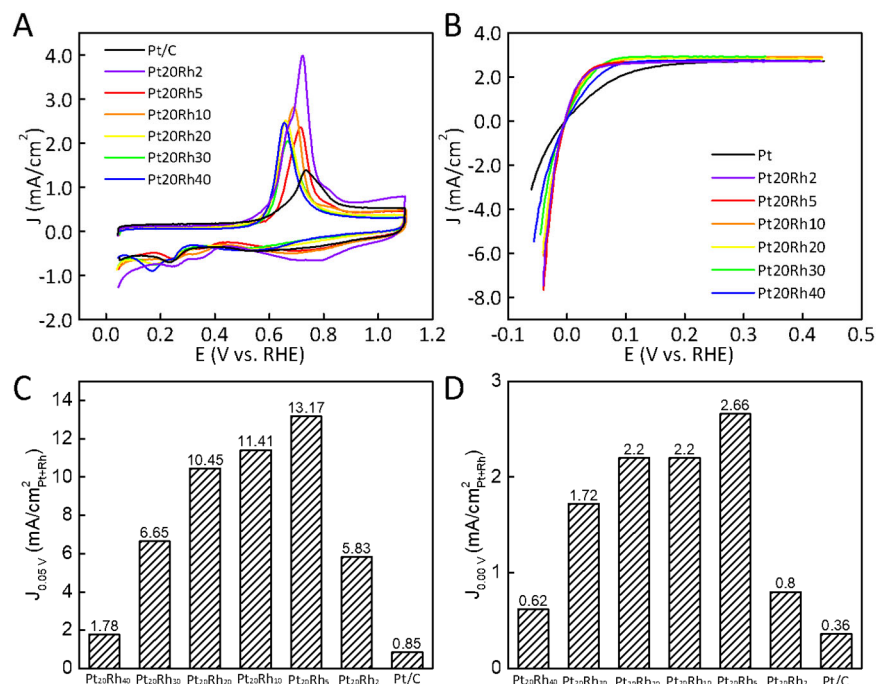
Figure 3.4. (A) HER/HOR polarization curve; (B) CO stripping; (C) specific activity and (D) exchange current density of Pt/C, $Pt_{20}Rh_2$, $Pt_{20}Rh_5$, $Pt_{20}Rh_{10}$, $Pt_{20}Rh_{20}$, $Pt_{20}Rh_{30}$, $Pt_{20}Rh_{40}$.

It was revealed by the XANES spectra that the single Rh atoms under 0 V vs. RHE are slightly positively charged (**Figure 3.5**) The *in-situ* and *ex-situ* XANES spectra of Rh L edge (**Figure 3.5A** and **B**) shows that Rh is redox-active and electroactive. The positive shift of the edge position from Rh foil to Rh under 0 V vs. RHE indicates that the single Rh atoms under 0 V vs. RHE is slightly oxidized. The Rh is largely oxidized at a potential higher than 0.3 V vs. RHE. From 0.3 to 0 V vs. RHE, although the XANES edge does not shift at all, the oscillation increases, and the FT-EXAFS peak intensity increases accordingly (**Figure 3.5C** and **D**). This indicates the removal of nearly neutral oxygen species (OH_{ad} and/or H_2O_{ad}) that blocks the Rh-Pt interactions with decreasing potentials. As the potential increase, Rh-O bond intensity increase, and Rh-Pt bond intensity decreases, as expected from the oxidation from slightly charged single atom Rh to single $Rh(OH)_x$ species.

Note that the Rh-O peak shift positively when potentials shifts from 0.54 V to 0 V, indicating an elongated Rh-O bond at a lower potential, which indicates that the adsorbed oxygen species under 0 V are not the OH from Rh(OH)x and should be weakly adsorbed OH or $H_2O\downarrow$. The fitting of in-situ EXAFS of Rh L edge on the SARh-PtNWs also confirms that the Rh atoms are bonded with eight Pt atoms and one OH_{ads}, and No Rh-Rh interaction is observed (**Table 3.1**). It should be addressed that the regular water structure on negatively charged Pt surface below the PZFC should in hydrogen downward direction and cannot assist the removal of H_{ads}, however, with the help of Rh, the surface water molecule alignment is partially changed to oxygen downwards on the Rh sites.
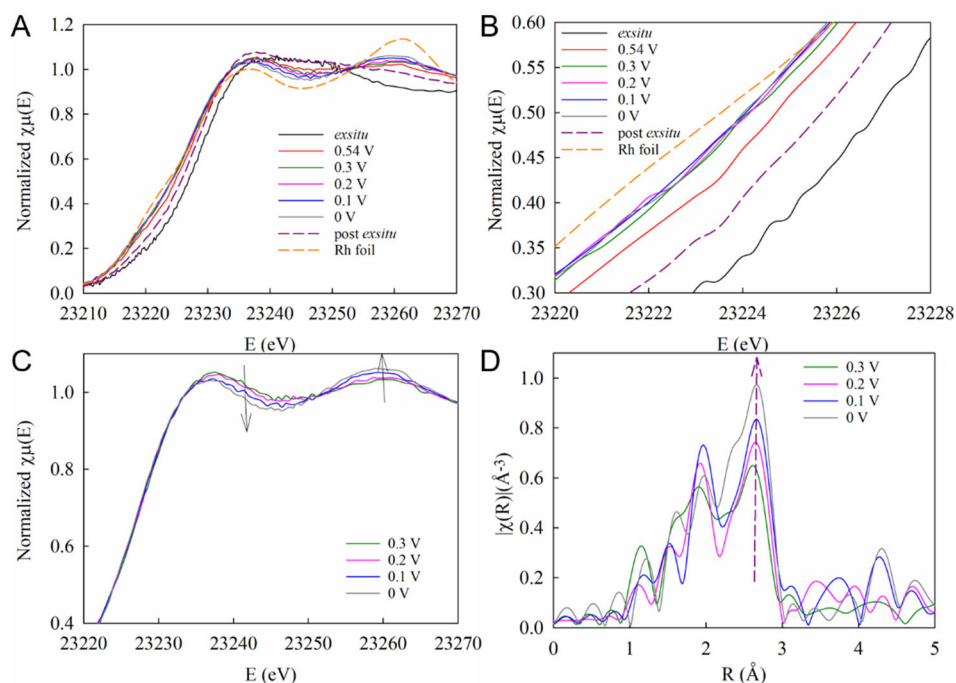
Figure 3.5. (A) The Rh L-edge in-situ XANES of SARh-PtNWs from 0 V to 0.54 V vs. RHE and the ex-situ, post-ex-situ XANES spectra of Rh foil, and (B) zoom-in region. The Rh L-edge in-situ (C) XANES and (D) FT-EXAFS under 0 V, 0.1 V, 0.2 V, and 0.3 V vs. RHE

74

The existence of single atom Rh-OH$_{ads}$ or Rh-H$_2$O$_\downarrow$ under 0 V vs. RHE significantly facilitates the sluggish Volmer step at the minimal sacrifice of the active Pt sites where H$_2$ dissociation and H adsorption take place. When the surface Rh concentration surpasses a critical point, singly dispersed Rh atoms start to aggregate to a continuously distributed Rh layer which significantly increases the surface oxophilicity, but at the sacrificial of highly active Pt site for H$_2$ dissociation and H surface coverage. HOR requires an equilibrium of H adsorption and OH/H$_2$O adsorption on the Pt surface to reach the maximum oxidation rate of H$_2$. However, both the Tafel step and the Volmer step on the Rh rich Pt surface are far away from the optimum condition, Also, the excess Rh and adsorbed water may form a rigid water layer that covers the Pt surface and prevents it from accessing to the H$_2$, results in the decreased overall HOR activity.

Table 3.1. EXAFS fitting of SARH-PtNWs.

Rh-Pt	$R_{Rh\text{-}Pt}$ (Å)	$N_{Rh\text{-}Pt}$	$\sigma^2_{Rh\text{-}Pt} \times 10^{-3}$ (Å^2)	$R_{Rh\text{-}O}$ (Å)	$N_{Rh\text{-}O}$	$\sigma^2_{Rh\text{-}o} \times 10^{-3}$ (Å^2)	E_0 (eV)
Ex situ	2.76±0.01	3±1	7±2	2.01±0.01	3.8±0.5	5±2	1±2
0 V	2.748±0.006	7.8±1.0	6.2±0.8	2.05±0.02	0.6±0.2	0.001 (fixed)	-3±1
Post Exsitu	2.754±0.008	5.6±0.9	8±1	2.017±0.009	3.1±0.3	4±1	0±1

3.4 Conclusion

In short, we have synthesized a series of PtRh NWs with different surface Rh concentration by controlling the molar ratio between the Pt(acac)$_2$ and Rh(acac)$_3$ and found that the HOR activity reaches the maximum value when the Rh is in the single-atom structure. We have conducted the *in-situ EXAFS and XANES spectroscopy* to carefully probe the atomistic structure, electronic and chemical state of Pt, and single-atom promotors under the real reaction condition. No Rh-Rh

bonding was observed from 0 V to 0. 54 V vs. RHE, the potential range where HOR takes place. It was revealed by the XANES and the fitting of *in-situ* FT-EXAFS spectra that the single Rh atoms at 0 V vs. RHE are slightly positively charged and bonded with eight Pt atoms and one O atom. And this Rh-O bond is longer than the Rh-O bond in the regular Rh oxides, indicating that this Rh-O bond may be from the Rh- $OH_{ads}/H_2O\downarrow$. The existence of this special Rh- $OH_{ads}/H_2O\downarrow$. under 0 V vs. RHE significantly facilitates the sluggish Volmer step at the minimal sacrifice of the active Pt sites where H_2 dissociation and H adsorption takes place.

In the future, we will collaborate with the computation chemistry group for further understanding of the HOR mechanism on a single atom tailored Pt surface and try to summarize the data to be a high-quality paper targeted at high impact journal.

3.5 Reference

1   Abbasi, R., Setzler, B. P., Lin, S., Wang, J., Zhao, Y., Xu, H., Pivovar, B., Tian, B., Chen, X., Wu, G. & Yan, Y. A Roadmap to Low-Cost Hydrogen with Hydroxide Exchange Membrane Electrolyzers. *Advanced Materials* **31**, 1805876 (2019).

2   Gu, S., Cai, R., Luo, T., Chen, Z., Sun, M., Liu, Y., He, G. & Yan, Y. A Soluble and Highly Conductive Ionomer for High-Performance Hydroxide Exchange Membrane Fuel Cells. *Angewandte Chemie International Edition* **48**, 6499-6502 (2009).

3   Durst, J., Siebel, A., Simon, C., Hasché, F., Herranz, J. & Gasteiger, H. A. New insights into the electrochemical hydrogen oxidation and evolution reaction mechanism. *Energy & Environmental Science* **7**, 2255-2260 (2014).

4   Ledezma-Yanez, I., Wallace, W. D. Z., Sebastián-Pascual, P., Climent, V., Feliu, J. M. & Koper, M. T. M. Interfacial water reorganization as a pH-dependent descriptor of the hydrogen evolution rate on platinum electrodes. *Nature Energy* **2**, 17031 (2017).

5   Dubouis, N. & Grimaud, A. The hydrogen evolution reaction: from material to interfacial descriptors. *Chemical Science* **10**, 9165-9181 (2019).

6   Liu, E., Jiao, L., Li, J., Stracensky, T., Sun, Q., Mukerjee, S. & Jia, Q. Interfacial water shuffling the intermediates of hydrogen oxidation and evolution reactions in aqueous media. *Energy & Environmental Science* **13**, 3064-3074 (2020).

7   Strmcnik, D., Uchimura, M., Wang, C., Subbaraman, R., Danilovic, N., Van Der Vliet, D., Paulikas, A. P., Stamenkovic, V. R. & Markovic, N. M. Improving the hydrogen oxidation reaction rate by promotion of hydroxyl adsorption. *Nature chemistry* **5**, 300 (2013).

8   Danilovic, N., Subbaraman, R., Strmcnik, D., Chang, K. C., Paulikas, A., Stamenkovic, V. & Markovic, N. M. Enhancing the alkaline hydrogen evolution reaction activity through the bifunctionality of Ni (OH) 2/metal catalysts. *Angewandte Chemie* **124**, 12663-12666 (2012).

9   Li, J., Ghoshal, S., Bates, M. K., Miller, T. E., Davies, V., Stavitski, E., Attenkofer, K., Mukerjee, S., Ma, Z.-F. & Jia, Q. Experimental Proof of the Bifunctional Mechanism for the Hydrogen Oxidation in Alkaline Media. *Angewandte Chemie International Edition* **56**, 15594-15598 (2017).

10   Strmcnik, D., Uchimura, M., Wang, C., Subbaraman, R., Danilovic, N., van der Vliet, D., Paulikas, A. P., Stamenkovic, V. R. & Markovic, N. M. Improving the hydrogen oxidation reaction rate by promotion of hydroxyl adsorption. *Nature Chemistry* **5**, 300-306 (2013).

11   Ramaswamy, N., Ghoshal, S., Bates, M. K., Jia, Q., Li, J. & Mukerjee, S. Hydrogen oxidation reaction in alkaline media: Relationship between electrocatalysis and electrochemical double-layer structure. *Nano Energy* **41**, 765-771 (2017).

12   Lamoureux, P. S., Singh, A. R. & Chan, K. pH Effects on Hydrogen Evolution and Oxidation over Pt(111): Insights from First-Principles. *ACS Catalysis* **9**, 6194-6201 (2019).

CHAPTER 4. WATER PERMEABLE NI(OH)₂ LAYER ON PT TETRAHEDRA FRAMEWORK AS HIGHLY ACTIVE HYDROGEN EVOLUTION ELECTROCATALYSTS

4.1 Introduction

Satisfying the increasing energy demand of our society while simultaneously fighting global warming requires the development of green energy technology that can efficiently produce renewable chemical fuels (e.g., H_2). The conventional production of hydrogen gas is mainly based on steam reforming of natural gas and fossil fuels, which is highly energy-consuming and emits millions of tons of carbon dioxide annually[1]. Moreover, due to the nature of the steam reforming reaction, impurities such as CO or H_2S are inevitable in the produced H_2[1]. Trace amounts of such impurities can severely poison the platinum (Pt) based catalysts currently used in proton exchange membrane fuel cells (PEMFCs)[2,3]. Therefore, electrochemical and photoelectrochemical hydrogen production has attracted considerable interest worldwide as an alternative, environmentally friendly pathway to high purity hydrogen as feedstock for highly stable PEMFCs. To this end, the development of effective and reliable electrocatalysts is essential for electrochemical and photoelectrochemical hydrogen evolution reaction (HER).

Among all the elements, Pt is the best choice for electrochemical hydrogen evolution reaction (HER) due to the optimal hydrogen adsorption energy at the Pt surface.[4-11] The overpotential for HER with Pt catalysts in the acid condition is indeed small. Nonetheless, in the acidic condition, precious metals are the only reliable catalysts for oxygen evolution reaction (OER), yet still with significant overpotential. On the other hand, OER in the alkaline condition is much more favored even with non-precious metal hydroxides (Ni, Fe, Co, etc.), which significantly saves the cost of catalysts from the OER side. Moreover, the low-cost and durable

anion exchange membrane technique has also been rapidly developed in recent years, providing solid technical support for developing efficient anion exchange membrane (AEM) assembles.[12,13] Therefore, there is more motivation to conduct water electrolysis in alkaline conditions from OER and membrane perspective. However, the HER kinetics of Pt in the alkaline condition is about 2-3 orders of magnitude slower than that in acid due to the sluggish water dissociation step in the alkaline condition.
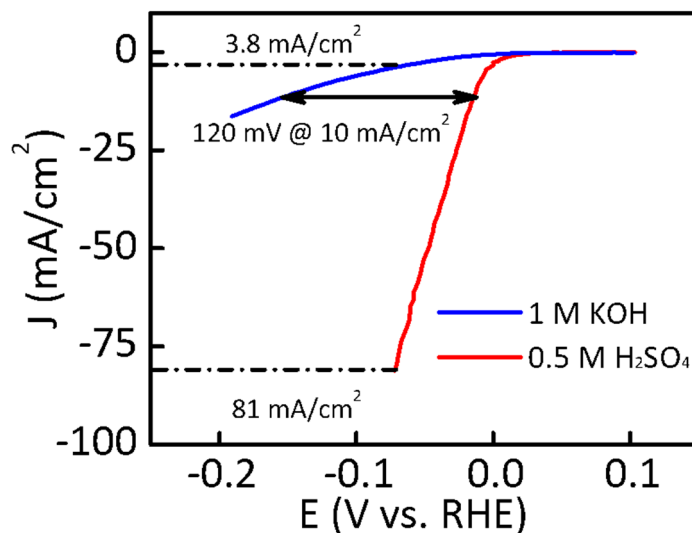
Figure 4.1. The discrepancy of Pt/C HER activity in acid and base.

Based on the HER polarization curve obtained with rotating disk electrode ($5\mu g_{Pt}/cm^2$) in 0.5 M H_2SO_4 and 1 M KOH (**Figure 4.1**), It is apparent that the overpotential required to reach a current density of only 10 mA/cm^2 in the alkaline electrolyte has already been up to 120-mV larger than that in acidic electrolyte. Since HER kinetics in the base is much slower, the Tafel slope of Pt/C in base (120 mV/dec in 1 M KOH) is also much bigger than it in acid (30 mV/dec, 0.5 M H_2SO_4). Therefore, the activity discrepancy between acid and base condition in the RDE test under relatively low current density (10 mA/cm^2) would be further amplified under full device condition at applicable current density (500-1000 mA/cm^2). The HER in KOH is not an "easy" reaction but

becomes one of the major problems. It has been revealed that greatly enhanced HER specific activity of Pt in alkaline condition can be achieved by decorating Pt surface with transition metal oxides but at the sacrificial of surface active sites and ECSA.[9] Most of the decorated Pt alkaline catalysts possess relatively high specific activity (SA, activity normalized by ECSA) but suffer from the low mass activity (MA, activity normalized by mass loading) and low ECSA because of the blockage of surface Pt sites by the decorated nanocrystals or the transition metal-based flakes that wrapped outside that is hydrogen impermeable.[14,15] Downsizing the decorated species to single-atom level can maximize the exposure of active sites around nickel single atoms to deliver an ultrahigh ECSA and mass activity, while its specific activity (10.72 mA/cm_{Pt}^2) is not as high as the reported PtNi-O octahedrons (14.8 mA/cm_{Pt}^2), indicating that the single Ni sites may not be the best solution for tailoring the HER kinetics on Pt surface and the specific activity due to the low single Ni/Pt sites ratio.[8,16] How to effectively decorated Pt surface while still maintain the proton accessibility to the Pt surface remains to be a challenge for designing Pt-based HER catalysts in alkaline condition. Constructing amorphous and defective $Ni(OH)_2$ shell on the Pt surface that can ensure both the proton accessibility to Pt surface and the fast water dissociation step is a good choice compared with a single atom Ni decorated surface and crystalline NiO decorated Pt surface. Herein, we report the synthesis of $Pt_{tet}@Ni(OH)_2$ core-shell structure with water/ion-permeable $Ni(OH)_2$ shell. The $Pt_{tet}@Ni(OH)_2$ exhibits the record high MA of 13.4 A/mg_{Pt} and SA (27.7mA/cm_{Pt}^2) for HER in 1 M KOH, which is over 17-fold and 28-fold higher than the mass activity and the specific activity of commercial Pt/C respectively.

4.2 Experimental Section

Chemicals: Platinum(II) acetylacetonate [$Pt(acac)_2$, Pt 48.0%], nickel(II) acetylacetonate [$Ni(acac)_2$, 95%], glucose, tungsten(0) hexacarbonyl ($W(CO)_6$, 97%), oleylamine (> 98%), 1-

octadecene (ODE, > 90%) and Nafion® 117 solution (~ 5%) were purchased from Sigma Aldrich. Commercial Pt/C catalyst (10 wt% Pt, and particle size ~ 2 nm) was purchased from Alfa Aesar. Ethanol (200 proof) was obtained from Decon Labs, Inc. Potassium hydroxide (KOH) was purchased from Fisher Chemical. All the above reagents were used as received without further purification. Carbon black (Vulcan XC-72) was received from Cabot Corporation and was annealed for 2 hours at 400 °C under Ar gas environment before used. The deionized water (18 MΩ/cm) was obtained from an ultra-pure purification system (Milli-Q advantage A10).

Synthesis of Pt$_{tet}$@Ni(OH)$_2$: In a 30 mL glass vial, 20 mg Pt(acac)$_2$, 25.6 mg Ni(acac)$_2$, 50 mg W(CO)$_6$, and 135 mg glucose were dissolved in a mixture of 3 mL oleylamine and 2 mL octadecene. The mixture was sonicated for 1 hour and the resulted homogenous solution was kept at 80 °C for 2.5 hours and then heated to 140 °C for another 8 hours. After the reaction, the precipitate was centrifuged out at 12100 r.p.m. and washed by ethanol/hexane (25 mL/5 mL) for three times. The final product was suspended in 10 mL cyclohexane.

Loading Tetrahedrons on Carbon: In a 30 mL glass vial, 30 mg carbon black was sonicated in 15 mL ethanol for 1 hour. 5 mL Pt$_{tet}$@Ni(OH)$_2$ hexane solution was then added into the carbon black/ethanol solution and the mixture was sonicated for another 1 hour. The catalysts were centrifuged out at 12100 r.p.m. and washed with cyclohexane/ethanol solution for three times, followed by being dried in the vacuum oven for 1 hour. The Pt$_{tet}$@Ni(OH)$_2$/C catalysts were then annealed in the air at 200 °C (air-Pt$_{tet}$@Ni(OH)$_2$)for 2 hours before the electrochemical test.

Characterization: Transmission electron microscopy (TEM) images were taken on an FEI T12 operated at 120 kV. Atomic resolution high-angle annular dark-field scanning transmission electron microscopy (HAADF-STEM) images and X-ray energy dispersive spectroscopy (EDS) mapping were taken on FEI Titan Cubed Themis G2 300 at 200 kV and JEOL Grand ARM 300CF

TEM/STEM with double spherical aberration-correctors operated at 300 kV. Samples for TEM measurements were prepared by dropping 10-20 μL nanoparticle dispersion in hexane on a carbon-coated copper grid (Ladd Research, Williston, VT). Powder X-ray diffraction patterns (PXRD) were collected on a Panalytical X'Pert Pro X-ray Powder Diffractometer with Cu-Kα radiation. The composition of catalysts was determined by inductively coupled plasma atomic emission spectroscopy (ICP-AES, Shimadzu ICPE-9000) as well as SEM-EDS (JEOL JSM-6700F FE-SEM). X-ray photoelectron spectroscopy (XPS) tests were done with Kratos AXIS Ultra DLD spectrometer.

Electrochemical Measurement: To obtain a homogeneous catalyst ink, 1 mg of dried air-Pt_{tet}@Ni(OH)$_2$/C was mixed with 1 mL ethanol and sonicated for 5 minutes. Then, 10 μL of Nafion (5 wt%) was added to the solution. After sonication, 20 μL of the homogeneous ink was dropped onto a 5 mm diameter glassy carbon electrode (0.196 cm^2, Pine Research Instrumentation). The Pt mass loading was about 5.6 μg/cm^2. The Pt/C was prepared in similar methods. The Pt mass loading for Pt/C was about 5.1 μg/cm^2. The ink was dried under ambient air, then was ready for electrochemical testing.

All electrochemical tests were carried out in a three-electrode cell from Pine Research Instrumentation. The working electrode was a glassy carbon rotating disk electrode (RDE) coated with corresponding catalysts. The reference electrode was a Hg/HgO electrode from CH Instrument and was calibrated in 1.0 M KOH with saturated H$_2$. A graphite rod was used as the counter electrode. The alkaline electrolyte was 1.0 M KOH saturated with N$_2$. Cyclic voltammetry (CV) was conducted in each solution between 50 mV to 1100 mV vs. Reversible Hydrogen Electrode (RHE) at a sweep rate of 100 mV/s. Hydrogen evolution reaction (HER) was tested between 200 mV to 100 mV vs. RHE at a sweep rate of 5 mV/s in 1.0 M KOH with a Pt loading

of 5.1 µg/cm^2 for Pt/C and 5.6 µg/cm^2 for Pt$_{tet}$@Ni(OH)$_2$. The impedance of 1 M KOH was tested on a CH Instrument electrochemistry workstation. The solution resistances measured via impedance test are 4.75 Ω for 1 M KOH. The above values are used for post-test iR correction. ECSA was tested through hydrogen underpotential deposition (Hupd) in N$_2$ saturated 1 M KOH. To perform the CO stripping test, the electrode was immersed in CO saturated 1.0 M KOH and kept under 50 mV vs. RHE for 30 minutes. It was then transferred to N$_2$ saturated 1.0 M KOH and kept under 50 mV vs. RHE for 10 minutes. Two full cycles from 50 mV to 1100 mV were then scanned at a rate of 25 mV/s. The stability test was performed with chronopotentiometry under 10 mA/cm^2 for 10 hours following the same setup used in the CV test.

4.3 Structure Characterization

Structure characterizations The Pt$_{tet}$@Ni(OH)$_2$ was prepared in a facile one-pot synthesis. The mixture of Pt(acac)$_2$, Ni(acac)$_2$, W(CO)$_6$, and glucose were dissolved in oleylamine (OAm) and octadecene (ODE) solution. The mixture was then heated to and maintained at 80 °C for 2.5 hours for nucleates incubation, followed by heating at 140 °C for another 8 hours to deliver the final products. The as-synthesized products were annealed under air under 200 °C for 1 hour to remove the surface ligands before testing the HER. The reaction temperature (140 °C) is selected since only Pt(acac)$_2$ can be reduced to metallic Pt under this temperature while Ni(acac)$_2$ is just decomposed to form Ni(OH)$_2$ shell on the Pt core. High temperature up to over 200 °C always leads to a well crystalized PtNi alloy other than a core-shell structure.[4,17,18]
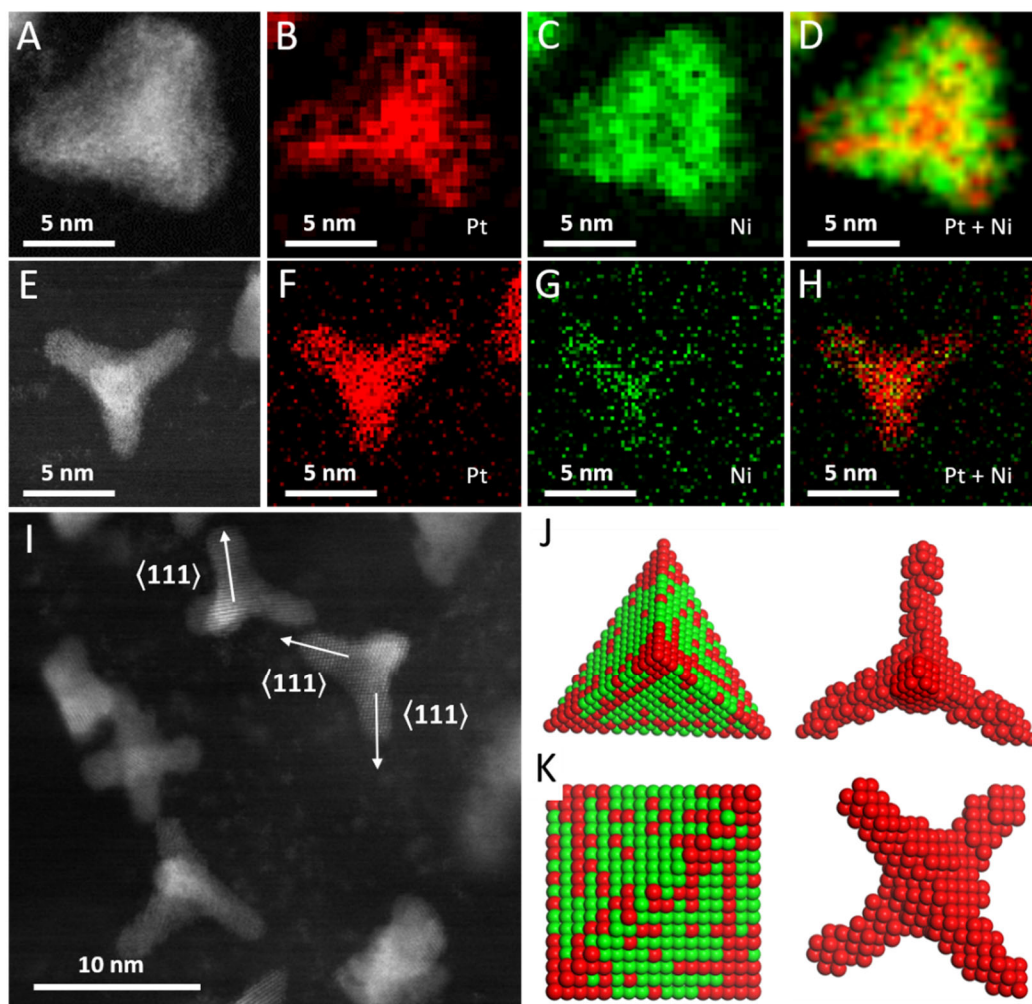
Figure 4.2. (A) HAADF-STEM of $Pt_{tet}@Ni(OH)_2$. EDS maps of the $Pt_{tet}@Ni(OH)_2$ (B) Pt, (C) Ni and (D) Pt+Ni. (E) HAADF-STEM of Pt skeleton after leaching $Pt_{tet}@Ni(OH)_2$ with 0.5 M H_2SO_4 for 2 days. EDS maps of Pt skeleton (F) Pt, (G) Ni and (H) Pt+Ni. (I) HAADF-STEM image of the Pt skeleton with different viewing angles and the <111> growth directions are marked with white arrows. (J) Structure illustration of The $Pt_{tet}@Ni(OH)_2$ and Pt skeleton from <111> direction. (K) Structure illustration of $Pt_{tet}@Ni(OH)_2$ framework and Pt skeleton from <002> direction.

Indeed, the $Pt_{tet}@Ni(OH)_2$ products exhibit interesting elemental segregation, as shown by the STEM EDS mapping (**Figure 4.2A-D**). Instead of a fully alloyed structure, the $Pt_{tet}@Ni(OH)_2$ is composed of Pt-rich tetrapod skeleton and Ni-based shell. To further confirm the Pt-rich tetrapod

skeleton structure, the $Pt_{tet}@Ni(OH)_2$ was dispersed in 0.5 M sulfuric acid under 60 °C for 48 hours to leach out the surface Ni species. The HAADF-STEM and EDS mapping images visualize the remaining Pt tetrapod skeleton with a trace amount of Ni residue after the acid leaching process (**Figure 4.2E-H**). Furthermore, the distance between the lattice fringe perpendicular to the Pt pods was measured to be 0.225 nm (**Figure 4.2I**), indicating that these Pt pods grow along with ⟨111⟩ directions. Based on the mapping images and the HAADF-STEM images above, the model in **Figure 1J** and **K** was constructed to clearly illustrate the shape and the elemental distribution of the $Pt_{tet}@Ni(OH)_2$. In **Figure 4.2J**, viewing along the ⟨111⟩ direction, a projection of a triangular structure and tripod structure can be observed for the $Pt_{tet}@Ni(OH)_2$ and the Pt skeleton, respectively. On the other hand, in **Figure 1K**, viewing along the ⟨002⟩ direction, a projection of square structure arises for The $Pt_{tet}@Ni(OH)_2$ framework while a cross structure is observed for the Pt skeleton. Thus, **Figure 2I** clearly shows a high population of tetrapod structures, indicating this elemental segregation is a general phenomenon for all the synthesized particles.

Detailed composition and the valence of Pt core and Ni shell were investigated by X-ray photoelectron spectroscopy (XPS) (**Figure 4.3A** and **B**). In **Figure 4.3A**, two main peaks at around 74.4 (Pt $4f_{5/2}$) and 71.1 eV (Pt $4f_{7/2}$) indicate that most of the Pt atoms are in the metallic phase. The existence of small Pt^{2+} and Pt^{4+} peaks indicates the slight oxidation of surface Pt atoms under ambient air. In **Figure 4.3B**, the small peak at around 852 eV belongs to the metallic Ni $2p_{3/2}$. The two main peaks at 856.1 eV and 873.7 eV belong to the $Ni(OH)_2$ $2p_{3/2}$ and $Ni(OH)_2$ $2p_{1/2}$ orbitals respectively, and the characteristic spin-energy separation of 17.6 eV between $Ni(OH)_2$ $2p_{3/2}$ and $Ni(OH)_2$ $2p_{1/2}$ is also in consist with other literature,[19,20] delivering clear results of $Ni(OH)_2$ dominated shell composition (**Figure 2A** and **B**). The singlet feature of the $Ni(OH)_2$ $2p_{1/2}$ (**Figure**

4.3B) also strengthens the conclusion of Ni(OH)$_2$ shell since NiO 2p$_{1/2}$ peak possesses a doublet

peak feature Ni 2p$_{1/2}$.[21-23]
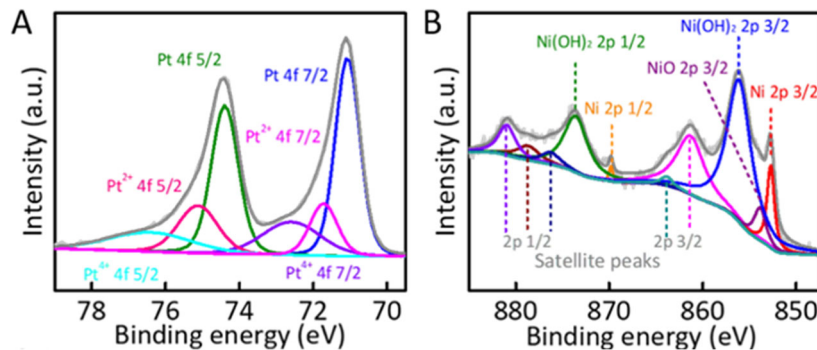
Figure 4.3. The structure characterization of the Pt$_{tet}$@Ni(OH)$_2$. High-resolution Pt 4f (A) and (B) Ni 2p

XPS spectra of the Pt$_{tet}$@Ni(OH)$_2$.

Based on such large element segregation, separation of the PtNi (111) and Ni(OH)$_2$ (101)

peaks is expected in the X-ray diffraction (XRD) pattern. However, in the XRD pattern of the

Pt$_{tet}$@Ni(OH)$_{2s}$, only symmetric Pt$_3$Ni$_1$ (111) peaks were found at 40.8°, which was related to the

Pt rich tetrapod skeleton (**Figure 4.4C**). No Ni-rich PtNi alloy (111) peak was found from 42° to

44° and no Ni(OH)$_2$ (101) peak was found at around 37° (**Figure 4.4C**). The absence of Ni-rich

PtNi alloy peaks could be ascribed to the highly segregated composition of Pt and Ni in the

nanoparticles. The absence of the Ni(OH)$_2$ peak is possibly due to the unavailable XRD signal

from the amorphous Ni(OH)$_2$ on the Pt$_{tet}$@Ni(OH)$_2$ surface.[24] Such an amorphous feature of

Ni(OH)$_2$ is also supported by the STEM images and the FFT pattern from HRTEM images (**Figure**

4.4A and B). In the FFT pattern (**Figure 4.4A** inset) extracted from **Figure 2C**, there are only the

Pt{202}, and {220} patterns and no signals from the crystalline Ni(OH)$_2$ structure. In **Figure 4.4B**,

Pt skeleton with {022} lattice fringe can be observed, however, in between each two Pt pods, only

blurry Ni(OH)$_2$ shell was observed, proving that the Ni(OH)$_2$ shell is amorphous.[24]
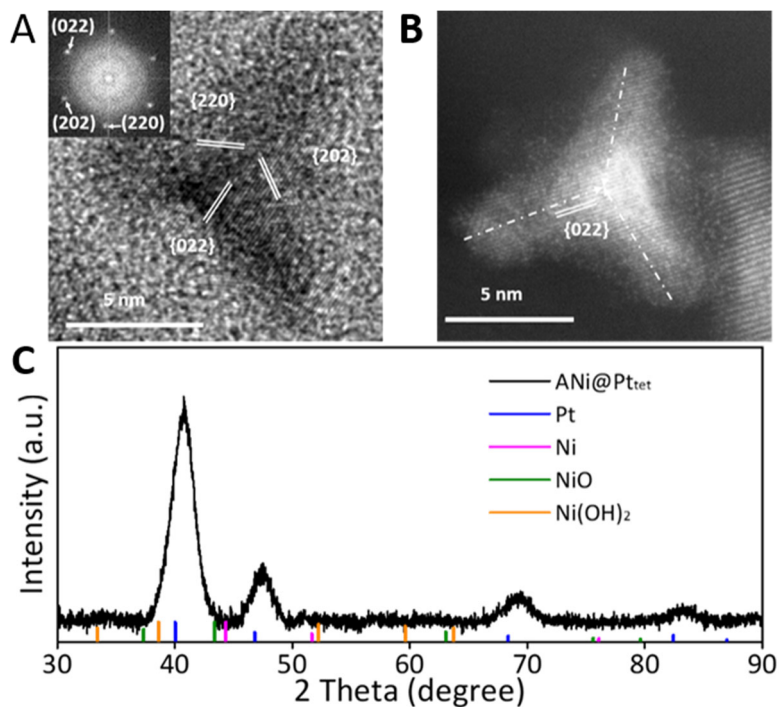
Figure 4.4. (A) HRTEM image with the inset FFT pattern and (B) HAADF-STEM image of The Pt$_{tet}$@Ni(OH)$_2$. (C) XRD pattern of the Pt$_{tet}$@Ni(OH)$_2$. The droplines represent the standard peak position of Pt (JCPDS PDF No. 96-101-1115), Ni (JCPDS PDF No. 04-0850), NiO (JCPDS PDF No. 96-101-0094), Ni(OH)$_2$ (JCPDS PDF No. 00-002-1112), respectively.

To remove the surface capping ligands, the as-synthesized the Pt$_{tet}$@Ni(OH)$_2$ were annealed under 200 °C in the air for 2 hours, denoted as air-Pt$_{tet}$@Ni(OH)$_2$. The air-Pt$_{tet}$@Ni(OH)$_2$ maintained the Pt tetrapod structure covered with a Ni(OH)$_2$ shell (**Figure 4.5**). The small metallic Ni 2p$_{3/2}$ peak at around 852 eV decreased and the Pt^{2+} and Pt^{4+} peaks increased (**Figure 4.3A** and **B**, and **Figure 4.6A** and **B**), indicating the slight surface oxidation of Pt$_{tet}$@Ni(OH)$_2$ after being annealed in air. From the singlet peak feature and the unchanged peak position of Ni(OH)$_2$ 2p$_{3/2}$ peak after annealing, the air annealed product still possesses the Ni(OH)$_2$ shell. Also, the slightly negative XRD peak shift (**Figure 4.4C** and **Figure 4.6C**) of air-Pt$_{tet}$@Ni(OH)$_2$ indicates slightly larger Pt/Ni segregation induced by the air annealing.
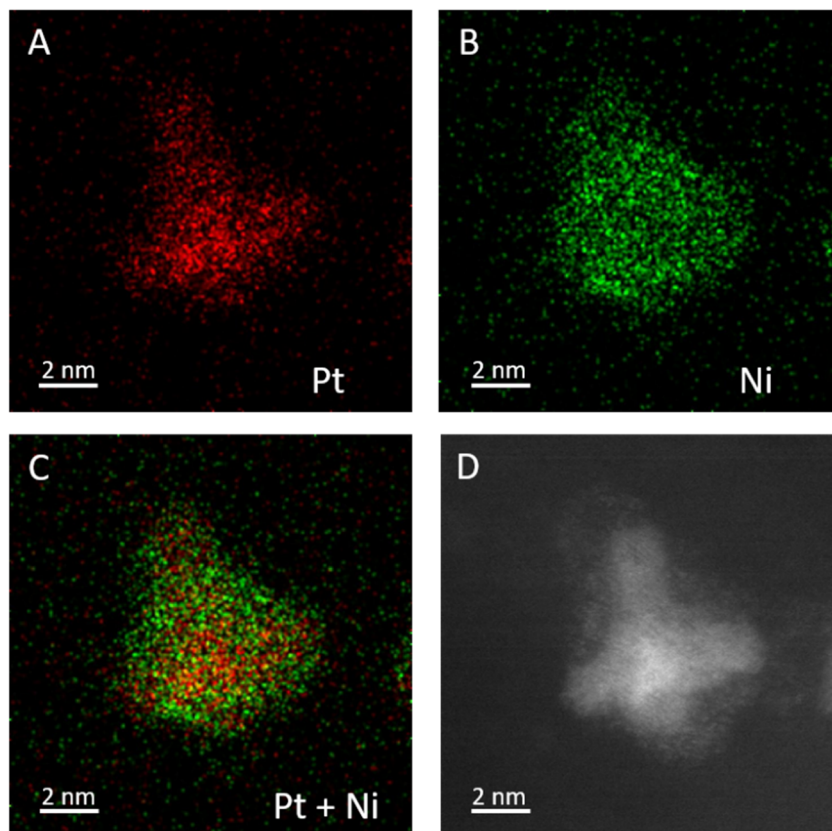
Figure 4.5. (A-C) STEM-EDS mapping images of the air-Pt$_{tet}$@Ni(OH)$_2$ and (D) the corresponding HAADF-STEM image.
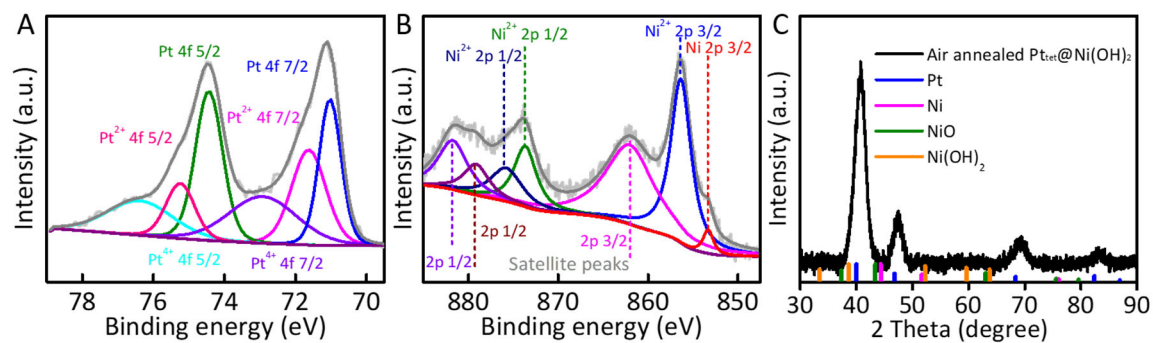
Figure 4.6. XPS (A) Pt$_{4f}$ and (B) Ni$_{2p}$ and (C) XRD characterization of the air-Pt$_{tet}$@Ni(OH)$_2$.

4.4 Amorphous Ni(OH)$_2$ Shell Boosts the Specific Activity of the Air-Pt$_{tet}$@Ni(OH)$_2$ towards HER While Maintains the Electrochemical Active Surface Area
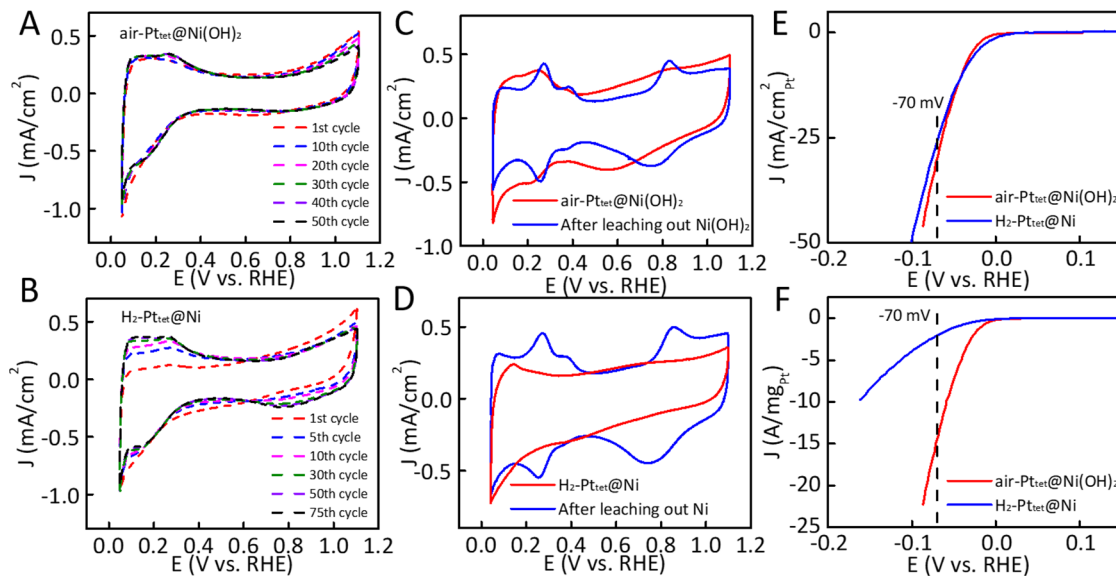
Figure 4.7. The Electrochemistry characterization of proton accessibility to the Pt sites on the air-Pt$_{tet}$@Ni(OH)$_2$ and H$_2$ annealed sample. (A) The CV of 1st, 10th, 20th, 30th, 40^{th,} and 50th cycle of The air-Pt$_{tet}$@Ni(OH)$_2$ in 0.1 M HClO$_4$ with the scan rate of 100 mV/s. (B) The CV of 1st, 5th, 10th, 30th, 50^{th,} and 75th cycle of air-Pt$_{tet}$@Ni(OH)$_2$ in 0.1 M HClO$_4$ with the scan rate of 100 mV/s. (C) The CV of air-Pt$_{tet}$@Ni(OH)$_2$ tested in 1 M KOH with and without leaching out the Ni(OH)$_2$ in acid, scan rate 100 mV/s. (D) The CV of H$_2$ annealed sample in KOH with and without leaching out the alloyed Ni.

It is recognized that the HER activity of pure Pt in alkaline solution is two orders of magnitude slower than that in acidic conditions due to the sluggish water dissociation kinetics and strong H-binding strength. Previous studies have suggested that decoration of the Pt (111) surface with transition metal oxides (Fe, Co, Ni) can lead to greatly enhanced HER activity in 0.1 M KOH,[9] However, ~50% of the ECSA of the Pt (111) electrode is blocked by the decorated Ni species. Surface decorated particles, such as NiO, NiS, and Ni$_4$N, usually possess high crystallinity after oxidation,[25] sulphuration,[26] and nitridation treatment,[27] hence block the proton from accessing the

Pt active sites under the decorated particles. And only a small fraction of Pt sites located near the interface can be activated. On the contrary, amorphous Ni(OH)$_2$ shell, with abundant defects that allow hydrogen permeation and fast water dissociation, can simultaneously activate all the surface Pt sites and maintain the ECSA, delivering both high specific activity and mass activity.
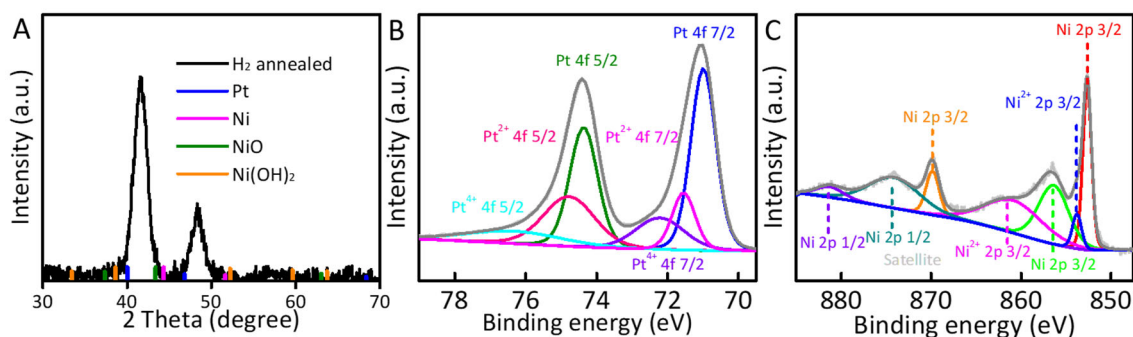
Figure 4.8. XRD and XPS characterization of H$_2$-Pt$_{tet}$@Ni(OH)$_2$.

Based on the XPS spectra and mapping results, the surface of air-Pt$_{tet}$@Ni(OH)$_2$ is dominated by amorphous Ni(OH)$_2$ layers. To evaluate the hydrogen permeability of the amorphous Ni(OH)$_2$ layer, cyclic voltammetry tests both in acid (0.1 M HClO$_4$) and based condition (1 M KOH) were conducted. The air-Pt$_{tet}$@Ni(OH)$_2$ was first undergoing the dealloying process in 0.1 M HClO$_4$. The 1st, 10th, 20th, 30th, 40^{th,} and 50th cycles were plotted in **Figure 4.7A**. The anode current density started above 0.8 V vs. RHE gradually decrease as the cycle number increase and finally stabilized, indicating they completed oxidation and dissolution of surface Ni species. On other hand, in the hydrogen underpotential deposition (Hupd) region, the 1st cycle's Hupd area still possess ~70% of the 50th Hupd area, indicating that the protons are accessible to the Pt surface even at the first cycle when the thick Ni(OH)$_2$ shell still cover the whole Pt core. Similarly, in the alkaline condition, when direct scanning the CV curve of air-Pt$_{tet}$@Ni(OH)$_2$ without any surface Ni(OH)$_2$ leaching process, the Hupd area of air-Pt$_{tet}$@Ni(OH)$_2$ is still 80% of the Hupd area of the Pt tetrapod skeleton which obtained from leaching out all the surface Ni(OH)$_2$, indicating that the

proton can easily penetrate the thick Ni(OH) shell in the alkaline condition as well (**Figure 4.7C**). To further confirm this hypothesis, we annealed $Pt_{tet}@Ni(OH)_2$ under 430 °C H_2/Ar (4/96) atmosphere for 1 hour to reduce the $Pt_{tet}@Ni(OH)_2$ into a well-crystallized structure denoted as H_2-$Pt_{tet}@Ni$. The thermal diffusion of Pt and Ni atoms results in a well-crystallized structure with a higher level of alloying, as indicated by the PtNi alloy peak shifted to a high angle in the XRD (**Figure 4.8A**) and the STEM-EDS mapping (**Figure 4.9**).
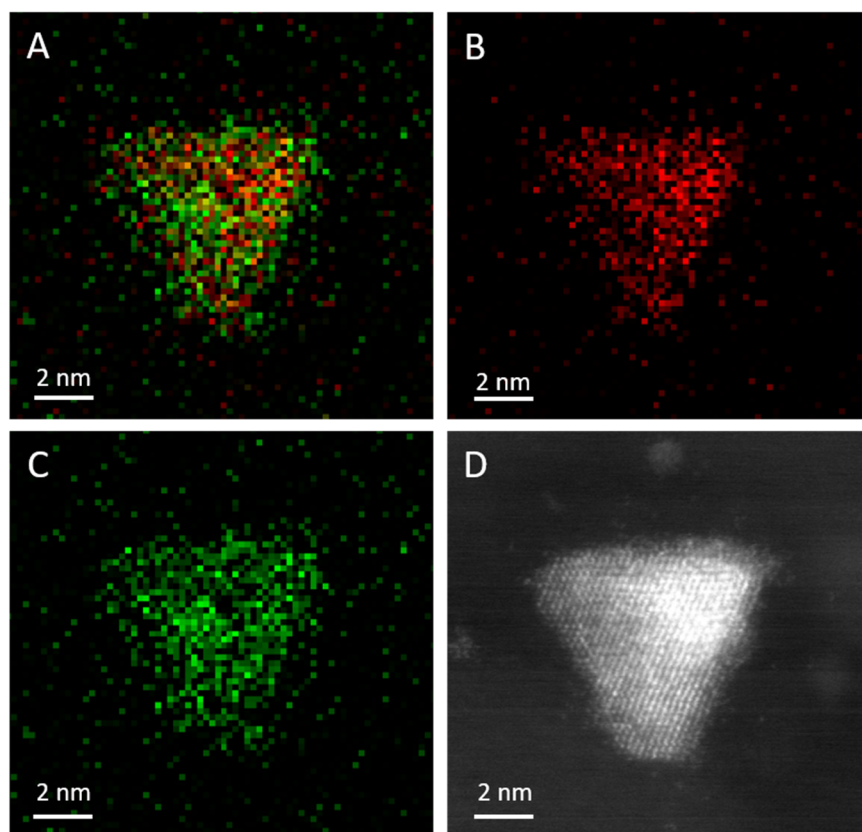
Figure 4.9. (A-C) STEM-EDS mapping images of H_2-$Pt_{tet}@Ni$ and (D) the relevant HAADF-STEM image.

The Ni 2p XPS spectra of the H_2 annealed sample shows most surface amorphous Ni(OH)$_2$ get reduced to metallic Ni (**Figure 4.8B** and **C**). Similar CV tests were conducted on the H_2-$Pt_{tet}@Ni$ (**Figure 4.7B** and **D**). In 0.1 M HClO$_4$, the Hupd area of H_2-$Pt_{tet}@Ni$ after 1st cycle is negligible while its Hupd is rapidly increasing when the surface Ni is dissolving, indicating that

the proton cannot penetrate well-crystallized dense Ni layer in acidic condition. Indeed, there is barely any Hupd area of the H_2-Pt_{tet}@Ni in 1 M KOH, compared with the Hupd area of the H_2 annealed products after first dealloying in the 0.1 M $HClO_4$ for 200 cycles to fully remove the alloyed Ni, indicating that the firm nickel layer is hydrogen impermeable in KOH and only a small portion of Pt atoms alloyed with Ni in the surface layer is accessible to the protons (**Figure 4.7D**). The HER activity of the air-Pt_{tet}@Ni(OH)$_2$ and the H_2-Pt_{tet}@Ni are investigated in 1 M KOH (**Figure 4.7E** and **F**). Because all the surface Pt sites on the H_2-Pt_{tet}@Ni are always surrounded by at least one Ni atoms, these Pt sites can be spontaneously activated during HER reaction. Therefore, the HER kinetics on all the surface Pt sites are accelerated to the maximum level. In **Figure 4.7E** the SA of Ni-rich PtNi alloy surface represents the upper limit of HER SA but at the sacrificial of 85% percent of the ECSA, which explains its low MA (**Figure 4.7 F**). On the other hand, air-Pt_{tet}@Ni(OH)$_2$ possesses comparable specific activity with PtNi alloy (**Figure 4.7E**), which means the Pt surface sites of air-Pt_{tet}@Ni(OH)$_2$ share the equal level of HER kinetics acceleration with PtNi alloy surface. Most importantly, the amorphous and defective nature of the Ni(OH)$_2$ shell ensures the high ECSA of air-Pt_{tet}@Ni(OH)$_2$ and thus delivering the maximum mass activity (**Figure 4.7F**).

To fairly evaluate and investigate the HER activity of our air-Pt_{tet}@Ni(OH)$_2$, we also benchmarked the electrocatalytic properties of the air-Pt_{tet}@Ni(OH)$_2$ against commercial Pt/C. The typical cyclic voltammetry (CV) curves of the air-Pt_{tet}@Ni(OH)$_2$ and 10 % commercial Pt/C in 1 M KOH at a sweep rate of 100 mV/s are shown in **Figure 4.10A**. Compared with the OH adsorption/desorption peak at around 0.782 V vs. RHE of Pt/C, the negative shifted broad peak of the air-Pt_{tet}@Ni(OH)$_2$ at around 0.516 V vs. RHE arises from the OH adsorption/desorption on surface segregated Ni species. In contrast, the change of H adsorption/desorption on Pt (110) step

is small (0.276 V for Pt/C and 0.256 V for the air-Pt$_{tet}$@Ni(OH)$_2$), indicating only a slight weakening of H binding strength with a surface decorated Ni. The ECSA was calculated to be 48.4 ± 2.1% m^2/g$_{Pt}$ for the air-Pt$_{tet}$@Ni(OH)$_2$ and 76.4 ± 2.0% m^2/g$_{Pt}$ for Pt/C based on the H$_{upd}$ current of the air-Pt$_{tet}$@Ni(OH)$_2$ and commercial Pt/C. **Figure 4.10B** shows the linear sweep voltammetry curves of the HER mass activity of the air-Pt$_{tet}$@Ni(OH)$_2$ and Pt/C in 1 M KOH with a sweep rate of 5 mV/s (after iR correction). At -70 mV vs. RHE, The air-Pt$_{tet}$@Ni(OH)$_2$ possesses MA of 13.4 ± 2.8% A/mg$_{Pt}$ and SA of (27.7 mA/cm$^2_{Pt}$), which is 17.8-fold and 28-fold higher than that of the commercial Pt/C (**Figure 4.10C**), and considerably higher than the reported state-of-the-art Pt and other noble metal (Ru and Ir) based alkaline HER catalysts so far (**Table 4.1** and **4.2**).[7,8,10,16,25,26,28-31] The overpotentials required to achieve 10 mA/cm^2 current density (normalized by electrode surface area, 0.196 cm^2) of air-Pt$_{tet}$@Ni(OH)$_2$ (Pt loading: 5.6 µg/cm^2) and commercial Pt/C (Pt loading: 5.1 µg/cm^2) are 24.5 mV and 129 mV, respectively (**Figure 4.11 A** and **B**). The exchange current density (normalized by ECSA) of air-Pt$_{tet}$@Ni(OH)$_2$ is 3.56 mA/cm^2 Pt while the Pt/C only exhibits 0.44 mA/cm$_{Pt}^2$ (Figure 4.11C), indicating the intrinsic high specific activity of The air-Pt$_{tet}$@Ni(OH)$_2$. Besides the high activity, the air-Pt$_{tet}$@Ni(OH)$_2$ also possesses promoted stability under CP testing at 10 mA/cm^2. Only a 28 mV overpotential increase was observed for The air-Pt$_{tet}$@Ni(OH)$_2$ while a 147 mV overpotential increase was observed for Pt/C under the same test conditions (**Figure 4.10D**, no iR). Post electrochemical XPS results of Ni (**Figure 4.12**) shows that no metallic Ni presented on the tetrahedron surface. This indicates that the reduction of Ni^{2+} to Ni(0) is negligible under the stability test conditions, demonstrating that the activity is stable over a long period. Additionally, the tetrahedron shape together with the segregated structure is clearly retained after the 10-hour stability test (**Figure 4.13**). The durable activity and stable structure are probably due to the shielding effect from Ni(OH)$_2$ shell.
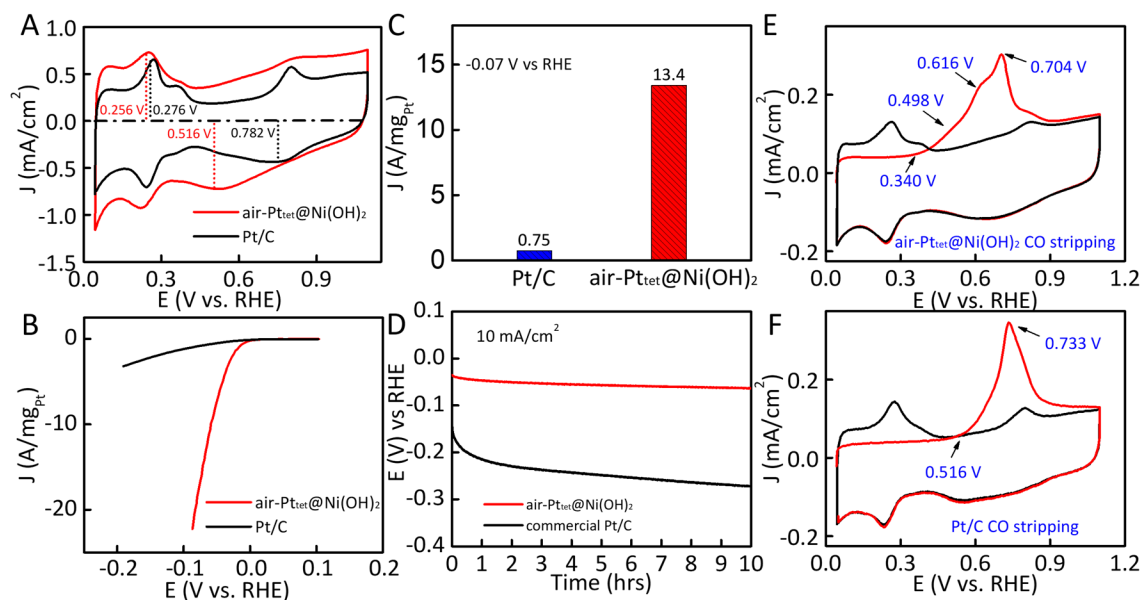
Figure 4.10. (A) Pt mass normalized HER polarization curve of Pt/C and the air-Pt$_{tet}$@Ni(OH)$_2$. Scan rate: 5 mV/s, rotation speed: 1600 r.p.m. After IR correction. (B) The mass activity of Pt/C and the air-Pt$_{tet}$@Ni(OH)$_2$ at -0.07 V vs RHE. (C) Tafel plot and the Tafel slope of Pt/C and The air-Pt$_{tet}$@Ni(OH)$_2$. (D) Comparison of exchange current density (ECSA normalized) of Pt/C and the air-Pt$_{tet}$@Ni(OH)$_2$. The 1st cycle of CO stripping scan (red) and the 2nd cycle of CO stripping scan (black) of (E) the air-Pttet@Ni(OH)$_2$ and (F) Pt/C.

Although both air-Pt$_{tet}$@Ni(OH)$_2$ and commercial Pt/C possess a similar onset overpotential, the significant difference of the Tafel slope (**Figure 4.11D**) indicates that there is greatly modified HER kinetics on the air-Pt$_{tet}$@Ni(OH)$_2$ with the existence of amorphous Ni(OH)$_2$. Due to the slow water dissociation rate in the alkaline condition, the Volmer step (H$_2$O + e$^-$ ↔ H$_{ads}$ + OH$^-$) replaces the Tafel step (H$_{ads}$ + H$_{ads}$ ↔ H$_2$) and Heyrovsky step (H$_2$O + e$^-$ + H$_{ads}$ ↔ H$_2$ + OH$^-$) to become the rate-determining step (rds) of HER, delivering a typical Tafel slope of around 120 mV/dec. Our Pt/C has a reasonable Tafel slope (~ 137 mV/dec) slightly higher than the 120 mV/dec. This deviation from the Bulter-Volmer equation is probably caused by the mass diffusion resistance under high overpotential and high current density. On the contrary, decoration of

94

amorphous surface Ni significantly accelerates the Volmer step so that the contribution of the Tafel step and Heyrovsky step should be taken into consideration as well. In this case, the Tafel slope should be within the range from 30 mV/dec to 120 mV/dec, and our air-Pt_{tet}@Ni(OH)$_2$ framework possesses a Tafel slope of ~ 75 mV/dec. Due to the negligible HER activity of Ni foam (**Figure 4.14A**), the Ni species are not expected to directly contribute significant HER current in our potential regime. Without Ni(OH)$_2$ decoration, the Pt_{tet} skeleton only retains around 34% HER current compared with the air-Pt_{tet}@Ni(OH)$_2$ framework (**Figure 4.14B**). The enhanced water dissociation has been attributed to the interaction between surface amorphous Ni(OH)$_2$ and the adsorbed OH_{ad} (Ni-OH_{ad}) and the amorphous Ni(OH)$_2$ provides abundant unsaturated Ni sites that interact more strongly with the OH_{ad} and enable faster water dissociation step compared with crystalized Ni(OH)$_2$ decoration.[9] The OH_{ad} is one of the reactants in the CO oxidation reaction, therefore the CO oxidation tests of air-Pt_{tet}@Ni(OH)$_2$ and Pt/C were conducted to probe the existence of Ni-OH_{ad}. In binary systems (i.e. PtNi, PtMo) CO oxidation reaction follows the Langmuir-Hinshelwood (L-H) pathway in which CO molecules are adsorbed on the Pt sites and the adsorbed OH group up on the more oxophilic Ni sites.[9] The existence of surface Ni^{2+}-OH_{ad} interactions would facilitate the oxidation of CO on the Pt sites, and thus the air-Pt_{tet}@Ni(OH)$_2$ framework should have a lower onset overpotential of CO oxidation with respect to Pt/C. Indeed, the CO stripping test demonstrates that the PtNi tetrahedron shows a 176 mV decrease in the onset overpotential for CO stripping and 29 mV decrease in the peak potential compared with the CO stripping curve of Pt/C (**Figure 4.10E** and **F**). Moreover, the appearance of another two peaks, which were not observed in the case of Pt/C, at around 0.498 V and 0.616 V vs. RHE, is due to the existence of surface Ni(OH)$_2$ and the interaction between Ni(OH)$_2$ site and CO.[7] The downshift of

CO oxidation onset overpotential and peak potential indicate the weaker CO binding strength on Pt surface due to the existence of surface OH_{ad}–$Ni^{\delta+}$ interactions.
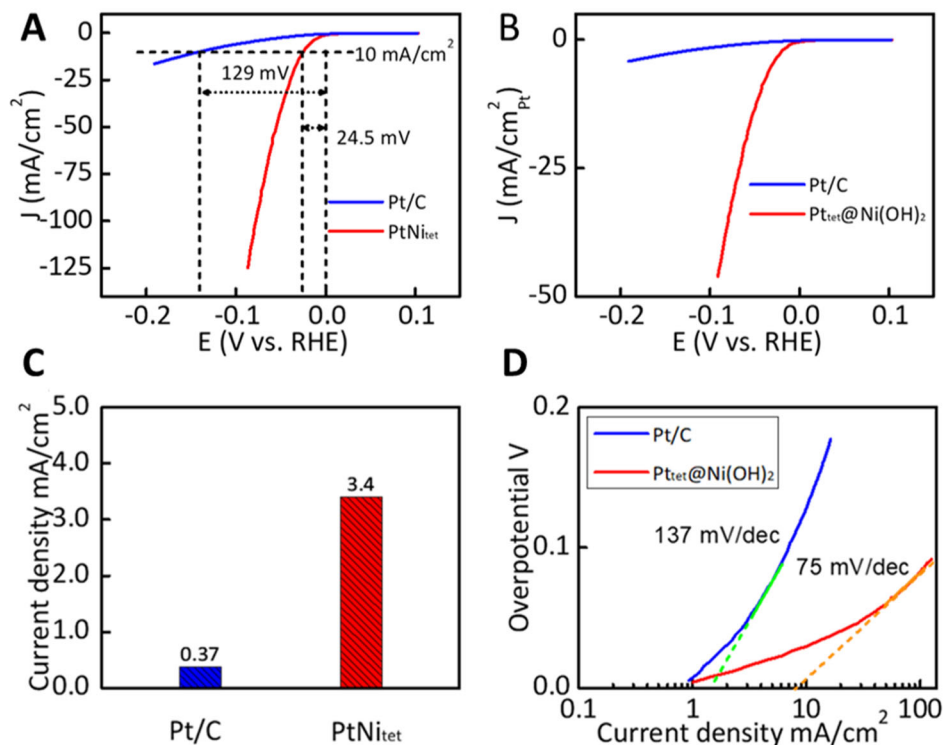
Figure 4.11. Electrode surface area normalized (A) and ECSA normalized (B) HER polarization curve of Pt/C and air-Pt_{tet}@$Ni(OH)_2$. Scan rate: 5 mV/s. 1600 r.p.m. (C) Exchange current density and (D) Tafel slope of Pt/C and air-Pt_{tet}@$Ni(OH)_2$.

4.5 Conclusion

In summary, we have developed a new shape-controlled synthesis method for the amorphous $Ni(OH)_2$@Pt_{tet} framework, with the highest mass activity and specific activity towards HER. Taking advantage of the low reducibility of the OAm system and the Ni induced anisotropic growth, an amorphous $Ni(OH)_2$/Pt interface is built to simultaneously ensure the mass transfer of protons and the rapid water dissociation step. The boosted HER activity and optimized Tafel slope of amorphous $Ni(OH)_2$@Pt_{tet} framework can be attributed to the high hydrogen permeability of

Ni(OH)$_2$ shell and the strong interaction between abundant Ni sites and OH$_{ad}$. This novel shape and surface-controlled synthesis of PtNi core-shell tetrahedra framework also fill a long-standing gap in the extensive list of Pt-based nanoparticle morphologies. Its high HER activity and stability resulting from the Ni(OH)$_2$ Pt/interface engineering is also an important step towards tailorable catalysts for a variety of reactions, vital for future energy demand.
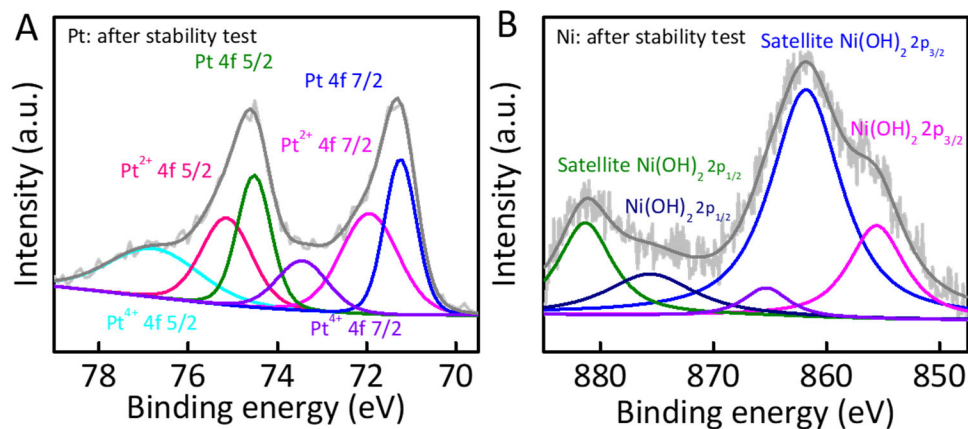
Figure 4.12. (A) The Pt 4f XPS spectra of air-Pt$_{tet}$@Ni(OH)$_2$ after chronopotentiometry test (B) The Ni 2p XPS spectra of air-Pt$_{tet}$@Ni(OH)$_2$ after chronopotentiometry test. Only peaks regarding the Ni(OH)$_2$ species were observed and No metallic Ni peak appeared, indicating that under 10 mA/cm^2 current density the reduction of Ni (2+) to Ni (0) is negligible.
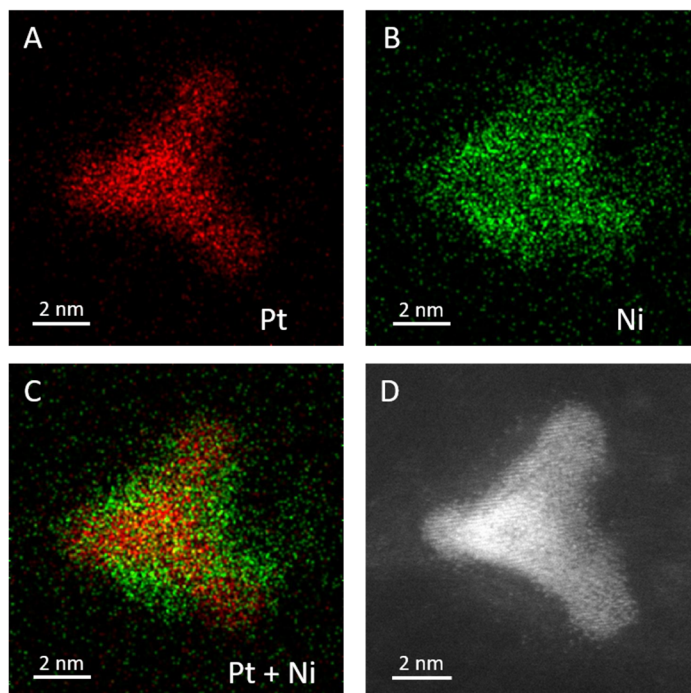
Figure 4.13. (A-C) STEM-EDS mapping images of $Pt_{tet}@Ni(OH)_2$ after chronopotentiometry test and (D) the corresponding HAADF-STEM image.
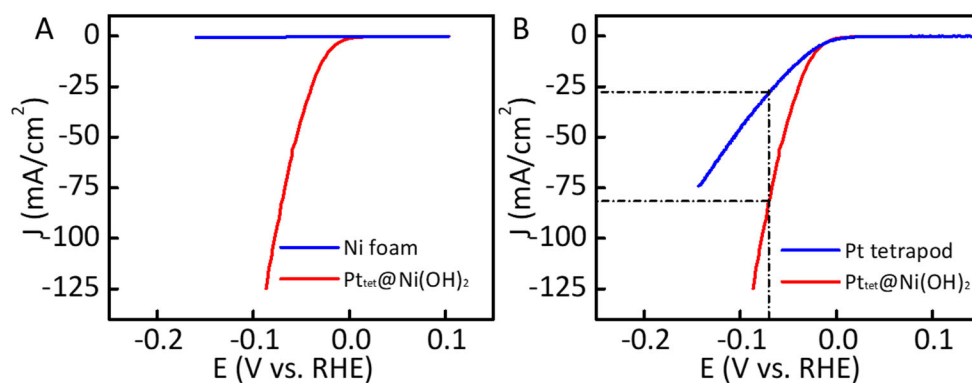
Figure 4.14. (A) The HER polarization curve of Ni foam and $Pt_{tet}@Ni(OH)_2$ in 1 M KOH. (B) HER Polarization curve of Pt tetrapod and $Pt_{tet}@Ni(OH)_2$ in 1 M KOH, scan rate: 5mV/s.

Table 4.1. Comparison of HER performance of the $Pt_{tet}@Ni(OH)_2$ in this work and the state-of-the-art literature.

To properly compare the overpotential at 10 mA/cm^2 (current normalized by electrode geometric surface area), the precious metal loading must be considered. However, the metal loading varies significantly among literature. Therefore, the comparison of the overpotential at fixed current (e.g.10 mA/cm^2) normalized by electrode geometric surface area seems meaningless. To remove the effect from metal loading, we believe the mass activity at certain overpotential (e.g. -70 mV vs. RHE) or the overpotential achieved at a given current density normalized by ECSA are more appropriate for comparing **the practical HER activity** of different noble metal catalysts in literature. Additionally, specific activity (current density normalized by ECSA) can provide a better understanding of the **intrinsic HER activity** of a given catalyst surface. Therefore, in this table, we used mass activity normalized by Pt loading and specific activity normalized by $ECSA_{Hupd}$ when comparing HER activity of our materials with state-of-the-art catalysts in literature (the mass activity values of other reported materials were calculated based on the reported mass loading and the electrode geometric surface area normalized HER polarization curve provided in these literatures).

Catalysts	Mass activity at -70 mV vs. RHE (mA/μg_{Pt})	Specific activity at -70 mV vs. RHE (mA/cm_{Pt}^2)	ECSA (m^2/g) in 1 M KOH	Reference
Pt/C	0.75	0.98	76.4	This work
air $Pt_{tet}@Ni(OH)_2$	14.5	27.6	48.5	This work
SANi-JPtNWs	11.8	10.72	106	Ref # 15
PtNiO octahedra	7.23	14.8	48.8	Ref #8
Pt NWs/ SL-Ni(OH)$_2$	0.68	2.48	27.4	Ref #7
NiO$_x$/Pt$_3$Ni Pt$_3$Ni$_3$-NWs	2.59	NA	NA	Ref #24

Pt$_3$Ni$_2$-NWs/S C	2.48	NA	NA	Ref #25		
Pt$_{3.6}$Ni-S NWs	~2.80	NA	NA	Ref #10		

Table 4.2. Comparison of HER performance of the Pt$_{tet}$@Ni(OH)$_2$ in this work and other state-of-the-art precious-metal-based catalysts from literature.

Catalyst	Metal loading (μg/cm^2)	Overpotential (mV) to reach 10 mA/cm^2 (Geometric surface area normalized)	Mass activity (A/mg$_{noble\ metal}$) in 1 M KOH at 10 mA/cm^2				Ref.
			-13.0 mV vs. RHE	-13.5 mV vs. RHE	-17.0 mV vs. RHE	-50.0 mV vs. RHE	
Pt$_{tet}$@Ni(OH)$_2$	5.6 (Pt)	24.5	**0.65**	**0.70**	**0.98**	**7.35**	This work
Pt/C	5.1 (Pt)	129	**0.17**	**0.17**	**0.19**	**0.51**	This work
Ru@C$_2$N	80 (Ru)	17.0	NA	NA	~0.125	NA	#27
Co-substituted Ru	153 (Ru)	13.0	0.065	NA	NA	NA	#28
Au-Ru-NWs	17 (Ru)	50.0	NA	NA	NA	~0.588	#29
Ir@CON	100 (Ir)	13.5	NA	0.097	NA	NA	30

We have also noticed that there are other precious metals (Ru and Ir) that could achieve a mass activity higher than Pt/C and the smallest overpotential at 10 mA/cm^2 with unique compositions and structures. We choose some state-of-art works and compared the overpotential of our Pt/C and Pt$_{tet}$@Ni(OH)$_2$ at 10 mA/cm^2 together with the mass activity under such overpotential and the mass loading.

4.6 Reference

1   Haryanto, A., Fernando, S., Murali, N. & Adhikari, S. Current Status of Hydrogen Production Techniques by Steam Reforming of Ethanol: A Review. *Energy & Fuels* **19**, 2098-2106 (2005).

2   Narusawa, K., Hayashida, M., Kamiya, Y., Roppongi, H., Kurashima, D. & Wakabayashi, K. Deterioration in fuel cell performance resulting from hydrogen fuel containing impurities: poisoning effects by CO, CH4, HCHO and HCOOH. *JSAE review* **24**, 41-46 (2003).

3   Kopasz, J. P. Fuel cells and odorants for hydrogen. *International Journal of Hydrogen Energy* **32**, 2527-2531 (2007).

4   Cao, Z., Chen, Q., Zhang, J., Li, H., Jiang, Y., Shen, S., Fu, G., Lu, B.-a., Xie, Z. & Zheng, L. Platinum-nickel alloy excavated nano-multipods with hexagonal close-packed structure and superior activity towards hydrogen evolution reaction. *Nature communications* **8**, 15131 (2017).

5   Danilovic, N., Subbaraman, R., Strmcnik, D., Chang, K. C., Paulikas, A., Stamenkovic, V. & Markovic, N. M. Enhancing the alkaline hydrogen evolution reaction activity through the bifunctionality of Ni (OH) 2/metal catalysts. *Angewandte Chemie* **124**, 12663-12666 (2012).

6   Chen, P., Zhou, T., Xing, L., Xu, K., Tong, Y., Xie, H., Zhang, L., Yan, W., Chu, W., Wu, C. & Xie, Y. Atomically dispersed iron–nitrogen species as electrocatalysts for bifunctional oxygen evolution and reduction reactions. *Angewandte Chemie International Edition* **56**, 610-614 (2017).

7   Yin, H., Zhao, S., Zhao, K., Muqsit, A., Tang, H., Chang, L., Zhao, H., Gao, Y. & Tang, Z. Ultrathin platinum nanowires grown on single-layered nickel hydroxide with high hydrogen evolution activity. *Nature communications* **6**, 6430 (2015).

8   Zhao, Z., Liu, H., Gao, W., Xue, W., Liu, Z., Huang, J., Pan, X. & Huang, Y. Surface-engineered PtNi-O nanostructure with record-high performance for electrocatalytic hydrogen evolution reaction. *Journal of the American Chemical Society* **140**, 9046-9050 (2018).

9   Subbaraman, R., Tripkovic, D., Chang, K.-C., Strmcnik, D., Paulikas, A. P., Hirunsit, P., Chan, M., Greeley, J., Stamenkovic, V. & Markovic, N. M. Trends in activity for the water electrolyser reactions on 3d M (Ni, Co, Fe, Mn) hydr (oxy) oxide catalysts. *Nature materials* **11**, 550 (2012).

10   Liu, Z., Qi, J., Liu, M., Zhang, S., Fan, Q., Liu, H., Liu, K., Zheng, H., Yin, Y. & Gao, C. Aqueous Synthesis of Ultrathin Platinum/Non-Noble Metal Alloy Nanowires for Enhanced Hydrogen Evolution Activity. *Angewandte Chemie* **130**, 11852-11856 (2018).

11   Seh, Z. W., Kibsgaard, J., Dickens, C. F., Chorkendorff, I., Nørskov, J. K. & Jaramillo, T. F. Combining theory and experiment in electrocatalysis: Insights into materials design. *Science* **355**, eaad4998 (2017).

12   Leng, Y., Chen, G., Mendoza, A. J., Tighe, T. B., Hickner, M. A. & Wang, C.-Y. Solid-State Water Electrolysis with an Alkaline Membrane. *Journal of the American Chemical Society* **134**, 9054-9057 (2012).

13   Abbasi, R., Setzler, B. P., Lin, S., Wang, J., Zhao, Y., Xu, H., Pivovar, B., Tian, B., Chen, X., Wu, G. & Yan, Y. A Roadmap to Low-Cost Hydrogen with Hydroxide Exchange Membrane Electrolyzers. *Advanced Materials* **0**, 1805876 (2019).

14   Sun, J., Wang, W. & Yue, Q. Review on Microwave-Matter Interaction Fundamentals and Efficient Microwave-Associated Heating Strategies. *Materials* **9**, 231 (2016).

15   Zhang, Z., Liu, G., Cui, X., Chen, B., Zhu, Y., Gong, Y., Saleem, F., Xi, S., Du, Y., Borgna, A., Lai, Z., Zhang, Q., Li, B., Zong, Y., Han, Y., Gu, L. & Zhang, H. Crystal Phase and Architecture Engineering of Lotus-Thalamus-Shaped Pt-Ni Anisotropic Superstructures for Highly Efficient Electrochemical Hydrogen Evolution. *Advanced Materials* **30**, 1801741 (2018).

16   Li, M., Duanmu, K., Wan, C., Cheng, T., Zhang, L., Dai, S., Chen, W., Zhao, Z., Li, P., Fei, H., Zhu, Y., Yu, R., Luo, J., Zang, K., Lin, Z., Ding, M., Huang, J., Sun, H., Guo, J., Pan, X., Goddard, W. A., Sautet, P., Huang, Y. & Duan, X. Single-atom tailoring of platinum nanocatalysts for high-performance multifunctional electrocatalysis. *Nature Catalysis* **2**, 495-503 (2019).

17   Choi, S.-I., Xie, S., Shao, M., Odell, J. H., Lu, N., Peng, H.-C., Protsailo, L., Guerrero, S., Park, J., Xia, X., Wang, J., Kim, M. J. & Xia, Y. Synthesis and characterization of 9 nm Pt–Ni octahedra with a record high activity of 3.3 A/mgPt for the oxygen reduction reaction. *Nano letters* **13**, 3420-3425 (2013).

18   Bu, L., Ding, J., Guo, S., Zhang, X., Su, D., Zhu, X., Yao, J., Guo, J., Lu, G. & Huang, X. A General Method for Multimetallic Platinum Alloy Nanowires as Highly Active and Stable Oxygen Reduction Catalysts. *Advanced Materials* **27**, 7204-7212 (2015).

19   Li, H. B., Yu, M. H., Wang, F. X., Liu, P., Liang, Y., Xiao, J., Wang, C. X., Tong, Y. X. & Yang, G. W. Amorphous nickel hydroxide nanospheres with ultrahigh capacitance and energy density as electrochemical pseudocapacitor materials. *Nature Communications* **4**, 1894 (2013).

20   Huang, W., Wang, H., Zhou, J., Wang, J., Duchesne, P. N., Muir, D., Zhang, P., Han, N., Zhao, F., Zeng, M., Zhong, J., Jin, C., Li, Y., Lee, S.-T. & Dai, H. Highly active and durable methanol oxidation electrocatalyst based on the synergy of platinum–nickel hydroxide–graphene. *Nature Communications* **6**, 10035 (2015).

21   Payne, B. P., Biesinger, M. C. & McIntyre, N. S. The study of polycrystalline nickel metal oxidation by water vapour. *Journal of Electron Spectroscopy and Related Phenomena* **175**, 55-65 (2009).

22   Mansour, A. N. Characterization of β-Ni(OH)2 by XPS. *Surface Science Spectra* **3**, 239-246 (1994).

23   Peck, M. A. & Langell, M. A. Comparison of Nanoscaled and Bulk NiO Structural and Environmental Characteristics by XRD, XAFS, and XPS. *Chemistry of Materials* **24**, 4483-4490 (2012).

24   Su, Y.-Z., Xiao, K., Li, N., Liu, Z.-Q. & Qiao, S.-Z. Amorphous Ni(OH)2 @ three-dimensional Ni core–shell nanostructures for high capacitance pseudocapacitors and asymmetric supercapacitors. *Journal of Materials Chemistry A* **2**, 13845-13853 (2014).

25   Wang, P., Jiang, K., Wang, G., Yao, J. & Huang, X. Phase and interface engineering of platinum–nickel nanowires for efficient electrochemical hydrogen evolution. *Angewandte Chemie International Edition* **55**, 12859-12863 (2016).

26   Wang, P., Zhang, X., Zhang, J., Wan, S., Guo, S., Lu, G., Yao, J. & Huang, X. Precise tuning in platinum-nickel/nickel sulfide interface nanowires for synergistic hydrogen evolution catalysis. *Nature Communications* **8**, 14580 (2017).

27   Xie, Y., Cai, J., Wu, Y., Zang, Y., Zheng, X., Ye, J., Cui, P., Niu, S., Liu, Y., Zhu, J., Liu, X., Wang, G. & Qian, Y. Boosting Water Dissociation Kinetics on Pt–Ni Nanowires by N-Induced Orbital Tuning. *Advanced Materials* **31**, 1807780 (2019).

28   Mahmood, J., Li, F., Jung, S.-M., Okyay, M. S., Ahmad, I., Kim, S.-J., Park, N., Jeong, H. Y. & Baek, J.-B. An efficient and pH-universal ruthenium-based catalyst for the hydrogen evolution reaction. *Nature nanotechnology* **12**, 441 (2017).

29   Mao, J., He, C.-T., Pei, J., Chen, W., He, D., He, Y., Zhuang, Z., Chen, C., Peng, Q., Wang, D. & Li, Y. Accelerating water dissociation kinetics by isolating cobalt atoms into ruthenium lattice. *Nature communications* **9**, 4958 (2018).

30   Lu, Q., Wang, A.-L., Gong, Y., Hao, W., Cheng, H., Chen, J., Li, B., Yang, N., Niu, W., Wang, J., Yu, Y., Zhang, X., Chen, Y., Fan, Z., Wu, X.-J., Chen, J., Luo, J., Li, S., Gu, L. & Zhang, H. Crystal phase-based epitaxial growth of hybrid noble metal nanostructures on 4H/fcc Au nanowires. *Nature chemistry*, 1 (2018).

31   Mahmood, J., Anjum, M. A. R., Shin, S. H., Ahmad, I., Noh, H. J., Kim, S. J., Jeong, H. Y., Lee, J. S. & Baek, J. B. Encapsulating Iridium Nanoparticles Inside a 3D Cage-Like Organic Network as an Efficient and Durable Catalyst for the Hydrogen Evolution Reaction. *Advanced Materials* **30**, 1805606 (2018).

CHAPTER 5. ANISOTROPIC GROWTH OF PT NANOCRYSTALS UNDER KINETIC CONTROL

5.1 Introduction

Pt is the most valuable element due to its unique catalytic properties. So far, Pt and Pt/transition metal (PtM) based materials form a class of superior catalysts for a wide range of clean energy-related reactions such as oxygen reduction reaction (ORR),[1-3] hydrogen evolution reaction (HER),[4-10] alcohol oxidation reaction (AOR),[11-15] and carbon monoxide (CO) oxidation reaction.[16-18] The catalytic properties of Pt-based nanocrystals are determined by a series of parameters, including the geometric structure,[19,20] the surface composition,[5,10,11,13,21-24,] and the electrochemical active surface area (ECSA).[2,20] For example, PtNi {111} enclosed octahedral nanoparticles exhibit higher ORR activity compared with that of PtNi {100} enclosed cubic nanoparticles due to the weaker absorption strength of OH on the PtNi {111} facet.[20,25,26] Thus, the geometrically shape-controlled and composition-controlled synthesis of Pt-based nanostructures is critical for the development of highly efficient electrocatalysts.

$$S = \sqrt{3}a^2$$
$$V = \frac{\sqrt{2}}{12}a^3$$
$$ECSA_{Te} = \frac{S}{\rho V} = \frac{6\sqrt{6}}{a\rho} = 85.6 \; m^2/g_{pt}$$
$$\frac{ECSA_{Tetrahedron}}{ECSA_{Octahedron}} = 2:1$$
Same edge length

$$S = 2\sqrt{3}b^2$$
$$V = \frac{\sqrt{2}}{3}b^3$$
$$ECSA_{Oct} = \frac{S}{\rho V} = \frac{3\sqrt{6}}{b\rho} = 42.8 \; m^2/g_{pt}$$
$$\frac{ECSA_{Tetrahedron}}{ECSA_{Octahedron}} = 1.26:1$$
Same volume

Figure 5.1. The theoretical ECSA of Pt tetrahedron and octahedron with an edge length of 8 nm, and the ECSA ratio of Pt tetrahedron and Pt octahedron with the same edge length and the same volume.

Synthesis strategies of Pt/transition metal (PtM) based nanostructures, including surface capping, templating, oxidative etching, and galvanic exchange reactions, have been extensively investigated and developed through methods[27]. One of the most widely reported {111} facets enclosed Pt-based nanocrystal is PtM alloy octahedra. **However, PtM-based tetrahedra, another typical {111} facets enclosed nanostructure, are rarely explored to date, possibly due to their intrinsically high surface-to-volume ratio and high surface energy when compared with the same {111} facet enclosed octahedrons**. Theoretically, the ECSA of pure Pt tetrahedron nanoparticles is 25% larger than the ECSA of Pt octahedron nanoparticle with the same volume, and 100% larger than that of a Pt octahedral nanoparticle with the same edge length (**Figure 5.1**). Thus, the thermodynamic stability of the octahedral shape is always recognized as the reason for octahedra being the major product rather than the tetrahedra. **However, such thermodynamic analysis only considers the Gibbs free energy difference between the initial state and the final state of the reaction, therefore cannot accurately describe the reaction process with multiple steps.** In recent years, the kinetics study of the growth of PtNi octahedra using *in situ scanning* transmission electron microscope (STEM) suggested that it was the anisotropic growth of the Pt seeds that directed the shape evolution of octahedra. Strasser *et al* revealed that the Pt_3Ni octahedra which used to be believed to have alloy structure were composed of Pt hexapod skeletons and eight Ni-rich {111} facets. Under a slow growth rate, two steps of growth that lead to the final octahedra shape were observed. First, the Pt nuclei start to selectively grow along {100} directions to deliver Cartesian coordinates like hexapod Pt framework, followed by a reduction of Ni(Co) that further fulfill the {111} facets. Therefore, the shape and element distribution of binary nanocrystals is not simply determined by thermodynamic surface free energy. Taking a step further, PtNi tetrahedron could also be achieved by the anisotropic growth of Pt seeds along the four <111>

directions with T_d symmetry. **Then, how to direct such anisotropic growth of the Pt core structure becomes the major problem in synthesizing PtNi tetrahedrons and other unique shapes.** Herein, we report a tunable synthesis of PtNi tetrahedrons (PtNi$_{tet}$) and PtNi octahedrons (PtNi$_{oct}$) by controlling the nucleation and growth of Pt atoms using glucose. Glucose, which is a typical reducing agent in the aqueous synthesis of nanoparticles, is found to be an inhibitor for deposition of Pt adatoms, and hence lead to the growth of Pt cuboctahedra seeds along the four <111> directions with T_d symmetric feature to become the Pt tetrapod skeleton. The simultaneous deposition of Ni on the four {111} facets helps deliver the final PtNi$_{tet}$. Conversely, without glucose, the deposition rate of Pt atoms is enhanced by a factor of four, and hence the PtNi$_{oct}$ with Pt hexapod skeleton and Ni shell becomes the major product.

5.2 Experimental Section

Synthesis of PtNi octahedra (PtNi$_{oct}$) 20 mg Pt(acac)$_2$, 25.6 mg Ni(acac)$_2$, and 32 mg W(CO)$_6$ were mixed in a 20 mL vial with 3 mL oleylamine (OAm) and 2 mL octadecene (ODE). The mixture was sonicated for 1 hour and then heated to 80 °C and kept at 80 °C for 2.5 hours. The temperature was further heated to 140 °C for another 8 hours. To collect the products at different reaction time, the reactions were immediately stopped using cold ethanol when the time reaches the setting number. After the reaction was stopped, the precipitate was centrifuged out at 12100 r.p.m. and washed by ethanol/hexane (25 mL/5 mL) for three times and suspended in 10 mL cyclohexane.

Synthesis of PtNi tetrahedra (PtNi$_{tet}$) 20 mg Pt(acac)$_2$, 25.6 mg Ni(acac)$_2$, 60 mg glucose and 32 mg W(CO)$_6$ were mixed 3 mL oleylamine (OAm) and 2 mL octadecene (ODE) and further heated to 80 °C and kept at 80 °C for 2.5 hours. The temperature was then heated to 140 °C for another 8 hours. To obtain the products at a different stage, the reactions were immediately stopped using

cold ethanol when the time reaches the desired reaction number. After the reaction was finished, the precipitate was centrifuged out at 12100 r.p.m. and washed by ethanol/hexane (25 mL/5 mL) for three times and suspended in 10 mL cyclohexane.

Synthesis of PtNi tetrahedra (PtNi$_{tet}$) with ascorbic acid 20 mg Pt(acac)$_2$, 25.6 mg Ni(acac)$_2$, 60 mg ascorbic acid and 32 mg W(CO)$_6$ were mixed 3 mL oleylamine (OAm) and 2 mL octadecene (ODE) and further heated to 80 °C and kept at 80 °C for 2.5 hours. The temperature was then heated to 140 °C for another 8 hours. To obtain the products at a different stage, the reactions were immediately stopped using cold ethanol when the time reaches the desired reaction number. After the reaction was finished, the precipitate was centrifuged out at 12100 r.p.m. and washed by ethanol/hexane (25 mL/5 mL) for three times, and suspended in 10 mL cyclohexane.

Synthesis of Pt cube 20 mg Pt(acac)$_2$, 60 mg glucose and 32 mg W(CO)$_6$ were mixed 3 mL oleylamine (OAm) and 2 mL octadecene (ODE) and further heated to 80 °C and kept at 80 °C for 2.5 hours. The temperature was then heated to 140 °C for another 8 hours. To obtain the products at a different stage, the reactions were immediately stopped using cold ethanol when the time reaches the desired reaction number. After the reaction was finished, the precipitate was centrifuged out at 12100 r.p.m. and washed by ethanol/hexane (25 mL/5 mL) for three times and suspended in 10 mL cyclohexane.

Synthesis of PtNi multi-pod 20 mg Pt(acac)$_2$, and 32 mg W(CO)$_6$ were mixed 3 mL oleylamine (OAm) and 2 mL octadecene (ODE) in 20 mL vial. The vial was purged with H$_2$ flow for 10 minutes and further heated to 80 °C and kept at 80 °C for 2.5 hours. The temperature was then heated to 140 °C for another 8 hours. To obtain the products at a different stage, the reactions were immediately stopped using cold ethanol when the time reaches the desired reaction number. After

the reaction was finished, the precipitate was centrifuged out at 12100 r.p.m. and washed by ethanol/hexane (25 mL/5 mL) for three times, and suspended in 10 mL cyclohexane.

Characterization: Transmission electron microscopy (TEM) images were taken on an FEI T12 operated at 120 kV. Atomic resolution high-angle annular dark-field scanning transmission electron microscopy (HAADF-STEM) images and X-ray energy dispersive spectroscopy (EDS) mapping were taken on FEI Titan Cubed Themis G2 300 at 200 kV and JEOL Grand ARM 300CF TEM/STEM with double spherical aberration-correctors operated at 300 kV. Samples for TEM measurements were prepared by dropping 10-20 μL nanoparticle dispersion in hexane on a carbon-coated copper grid (Ladd Research, Williston, VT). Powder X-ray diffraction patterns (PXRD) were collected on a Panalytical X'Pert Pro X-ray Powder Diffractometer with Cu-Kα radiation. The composition of catalysts was determined by inductively coupled plasma atomic emission spectroscopy (ICP- AES, Shimadzu ICPE-9000) as well as SEM-EDS (JEOL JSM-6700F FE-SEM). X-ray photoelectron spectroscopy (XPS) tests were done with Kratos AXIS Ultra DLD spectrometer.

5.3 Results and Discussion

Interesting elemental segregation of Pt and Ni was found in both the obtained PtNi$_{tet}$ and PtNi$_{oct}$, as shown by the representative HAADF-STEM and EDS mapping images (**Figure 5.2A-D** and **Figure 5.3A-D**). Instead of an alloy structure, the PtNi$_{tet}$ has composed of a Pt-rich tetrapod skeleton and four Ni-rich {111} facets while the PtNi$_{oct}$ is composed of a Pt-rich hexapod skeleton and eight Ni-rich {111} facets. To further study the detailed crystal structure of Pt tetrapod and hexapod, the as-obtained PtNi$_{tet}$ and PtNi$_{oct}$ were dispersed in 0.5 M sulfuric acid under 60 °C for 2 days to remove the surface Ni species. The representative HAADF-STEM and EDS mapping images of Pt skeletons show that after acid leaching of PtNi$_{tet}$ and PtNi$_{oct}$, the remaining Pt

skeletons are in the shape of tetrapod and hexapod, respectively. (**Figure 5.2G** and **Figure 5.3G**). For Pt tetrapod, the distance between the lattice fringe perpendicular to the Pt pods was measured to be 0.225 nm (**Figure 5.2G**), indicating that the growth direction of pods is the <111> direction. On the contrary, for Pt tetrapod (**Figure 5.3G**), the distance between the lattice fringe perpendicular to the pods in Pt tetrapod structure was measured to be 0.192 nm (**Figure 5.3G**), indicating that these hexapods grow along six <100> directions. Based on the above observation, it is apparent that the shape of PtNi nanocrystals is determined by the anisotropic growth of the Pt nucleates in different directions (<111> for tetrahedron and <100> for octahedron).
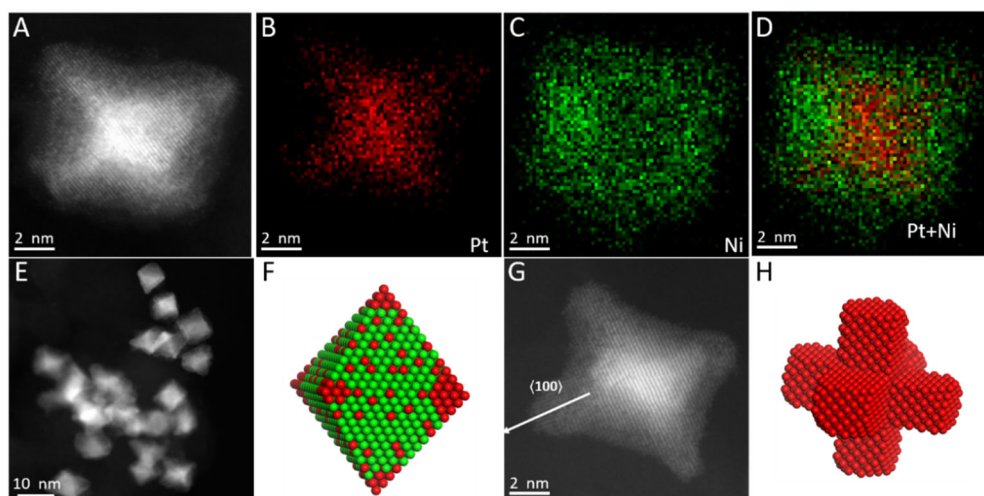

Figure 5.2. (A) HAADF-STEM image of PtNi$_{oct}$. (B) Pt mapping of PtNi$_{oct}$. (C) Nickel mapping of PtNi$_{oct}$. (D) Overlap of Pt and Ni mapping signal. (F) Illustration of PtNi$_{oct}$. (G) HAADF-STEM image of Pt hexapod after acid leaching of PtNi$_{oct}$.
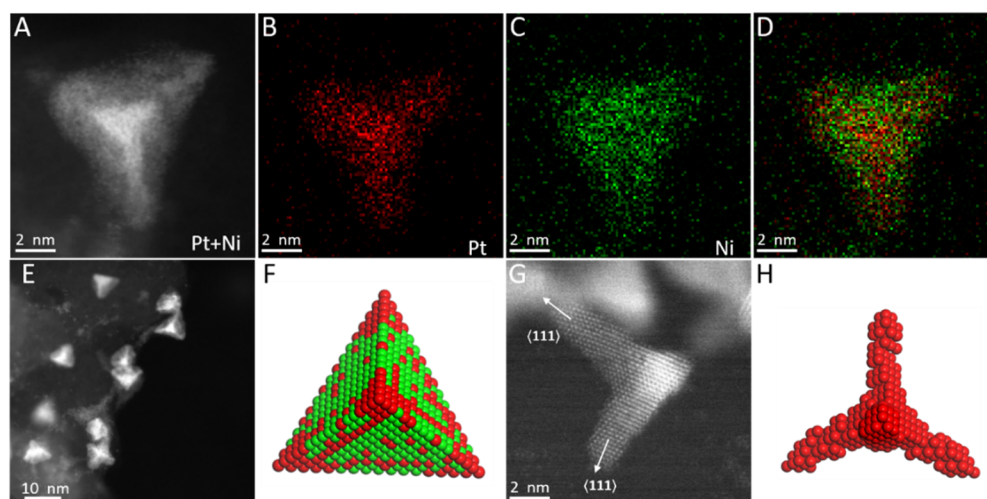
Figure 5.3. (A) HAADF-STEM image of PtNi$_{tet}$. (B) Pt mapping of PtNi$_{tet}$. (C) Nickel mapping of PtNi$_{tet}$. (D) Overlap of Pt and Ni mapping signal. (F) Illustration of PtNi$_{tet}$. (G) HAADF-STEM image of Pt hexapod after acid leaching of PtNi$_{tet}$.

The direction of anisotropic growth is found to be highly sensitive to the concentration of glucose. When increasing the glucose concentration from 0 to 27 mg/mL, an apparent products' shape transformation from octahedron to tetrahedron was observed. Without glucose, high-quality PtNi$_{oct}$ with a narrow distribution of size (8-10 nm) were obtained. When increasing the concentration to 5 mg/mL glucose, a large portion of tetrahedra immediately appeared in the product. Eventually, with an optimized glucose concentration of 27 mg/mL glucose, the high-quality PtNi$_{tet}$ was successfully synthesized. Time-tracking experiments of shape and composition evolution during synthesis were performed to further understand the function of glucose in tuning the anisotropic growth of PtNi$_{tet}$ and PtNi$_{oct}$. The products at different periods of reaction were collected by immediately quenching the reaction and centrifuging out all the products for ICP analysis and further yield calculation. All the supernatants were collected and checked under TEM to ensure the complete collection of products. Interestingly, contradictory to the well-recognized knowledge that glucose is a reductant which can accelerate the reduction rate of metal precursors,

the increased glucose concentration resulted in a decrease of reaction rate.[28] The detailed yield of

Pt and Ni for PtNi$_{tet}$ and PtNi$_{oct}$ were plotted versus their reaction time (**Figure 5.4**), respectively.
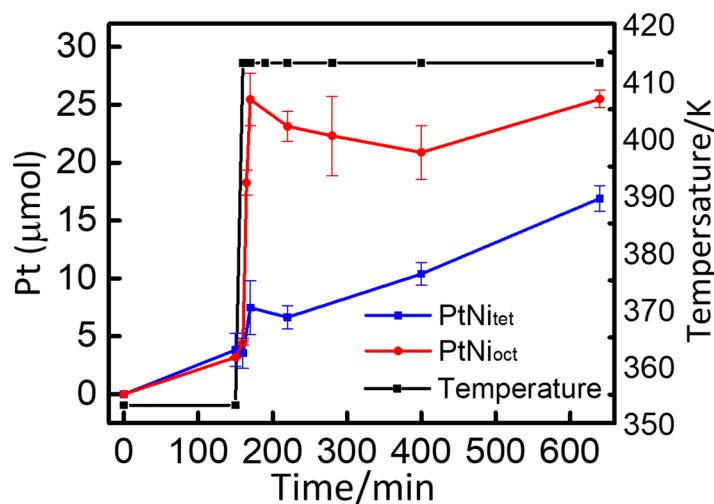

Figure 5.4. The Pt deposition rate of PtNi$_{tet}$ (blue) and Pt$_{oct}$ (red) and the temperature ramp line.

The deposition rate of Pt and Ni of PtNi$_{oct}$ is significantly higher than those of PtNi$_{tet}$ in the

nucleation and growth period. Particularly, in the first 10 mins, the growth rate Pt of PtNi$_{oct}$ is

approximately 4 times higher than that of PtNi$_{tet}$, indicating that the glucose no longer plays the

role of a reductant, and in turn, becomes the reaction inhibitor. However, glucose is a well-

acknowledged reductant used in numerous cases of nanoparticle synthesis for kinetics control in

aqueous conditions. One hypothesis is that the glucose or glucose derivatives may coordinate with

Pt together with Oleylamine. Instead of using reductant with abundant hydroxyl groups, gas-phase

H$_2$ was selected to avoid any ligand effect from hydroxyl groups. A high yield of branched

nanocrystals with irregular shapes (tetrapod, hexapod, pentapod) was obtained, indicating that the

reduction can be indeed accelerated by the reductive H$_2$, which leads to the overgrowth of different

type of branched Pt structures that are not accessible under thermodynamic control (**Figure 5.5A**).

Thus, the reason behind the retarded reaction rate when introducing glucose and other similar organic reductants is probably due to the ligand effect from glucose or its derivatives.
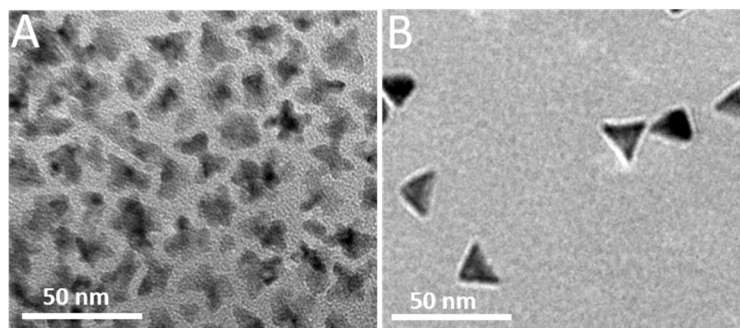

Figure 5.5. (A) The PtNi multi-pod structure was obtained from H_2 assisted reduction and the (B) The PtNi tetrahedron was obtained from AA assisted reduction.

Yin *et al.* in 2017 reported that Pt(acac)$_2$ could undergo ligand exchange reaction in the existence of OAm and form Pt(OAm)$_4$(acac)$_2$ complexes with amine N coordinated with the center Pt atoms.[29] Introducing carboxylic acid, such as oleic acid (OA), into the Pt(OAm)$_4$(acac)$_2$ leaded to the aminolysis of the acetylacetonate molecules and the formation of Pt(OAm)$_2$(OA)$_2$. Slower autocatalytic reduction of Pt(OAm)$_2$(OA)$_2$ to Pt adatoms were observed, compared with that of Pt(OAm)$_2$(acac)$_2$.[29] This is probably due to the higher binding strength of the carboxylic group to the Pt(2+). In the case of synthesis PtNi$_{tet}$, at the nucleation stage (80 °C), Pt atoms reduced by the glucose aggregate into small nucleates which can, in turn, catalyzed the oxidization of glucose to be gluconic acid (GA) and glucaric acid (GLA), two carboxylic acid anions which can provide one -COOH and two-COOH groups respectively. The formed highly stable Pt(OAm)$_2$(GA)$_2$ or Pt(OAm)$_2$GLA explains the low reduction rate of Pt(2+) to Pt(0) under 140 °C. The formation of ultrafine Pt clusters can be observed under 80 °C in the growth of PtNi$_{tet}$ but not in the growth of PtNi$_{oct}$ also prove the hypothesis. A similar PtNi$_{tet}$ was obtained but with a slightly larger size when replacing glucose with ascorbic acid (**Figure 5.5B**). Besides, glucose and their derivatives can bind

the Pt crystal surface to form a packed layer that inhibits the further deposition of Pt atoms on the existed crystal surface, thus decreases the growth rate of each Pt crystals.
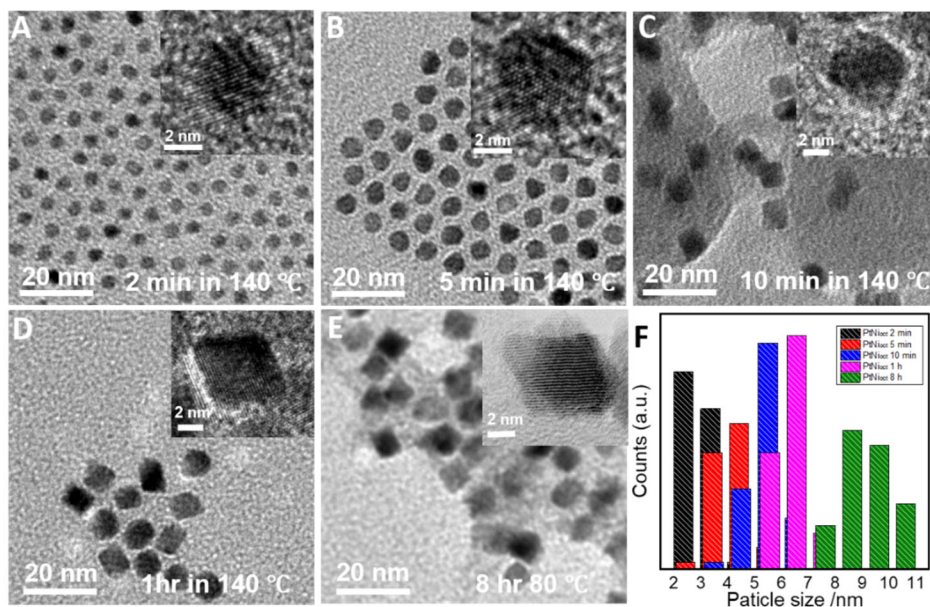

Figure 5.6. (A) TEM image of Pt nucleates after 2 min reaction in 140 °C, inset: representative HRTEM images of a typical cuboctahedron. (B) TEM image of Pt truncated octahedron clusters after 5 min reaction in 140 °C, inset: representative HRTEM images of a typical cuboctahedron shows the increased (111) facets and decreased (100) facts. (C) after 10 minutes, the Pt cuboctahedron has already evolved into Pt_9Ni_{1oct}. The Pt_9Ni_{1oct} gradually grows into (D) Pt_2Ni_{1oct} with 6-7 nm and (E) Pt_1Ni_{3oct} with 9-10 nm. (F) Size the evolution of the product during the reaction.

Furthermore, we monitored the evolution of $PtNi_{oct}$ and $PtNi_{tet}$ as a function of time to elucidate the mechanistic details of the shape growth (**Figure 5.6**). For the synthesis of $PtNi_{oct}$, no reduction of precursors was observed during the incubation time under 80 °C. Once upon the temperature reached 140 °C, small clusters with size from 1.2-2 nm appeared immediately, indicating a rapid decomposition of Pt precursors and a nucleation burst under 140 °C. ICP-AES analysis showed no Ni reduced at this point. Two mins after, the Pt clusters rapidly grew to

cuboctahedra with a size of approximately 2-3 nm, which is a typical thermodynamic stable shape for the seeds (**Figure 5.6A**). Five mins after the temperature reach 140 °C, the cuboctahedra evolved into truncated octahedra with an approximate 4 nm size (**Figure 5.6B**). The truncated octahedra further evolved into octahedra in another 10 min with a size of ~6 nm (**Figure 5.6C**). At this point, only ~11% Ni were alloyed in the $PtNi_{oct}$. **This rapid growth of octahedra is a typical kinetic process because the formation of Pt {111} terminated seeds is not thermodynamically preferred.** After 48 hours of acid wash, no obvious change in the Pt_8Ni_1 octahedra's morphology and no Pt skeleton were observed, indicating that the PtNi core-shell structure with Pt skeleton and Ni shell did not form at the early nucleation stage (**Figure 5.7**).
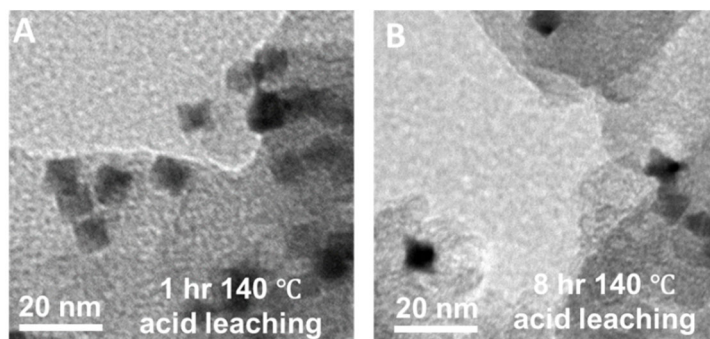

Figure 5.7. (A) 48-hour acid leaching of the $Pt_{2.4}Ni_1$ (1 hour 140 °C) remains an octahedral shape, indicating no anisotropic growth at this period. (B) 48-hour acid leaching of the Pt_1Ni_3 (8 hours 140 °C) remains octahedral shape, indicating the anisotropic growth.

When increasing the reaction time to 30 min, 1 hour (**Figure 5.6D**), 2 hours, 4 hours, and 8 hours (**Figure 5.6E**), the Pt_8Ni_1 octahedra gradually evolve into $Pt_{3.4}Ni_1$, Pt_2Ni_1, $Pt_{0.7}Ni_1$, Pt_1Ni_2, and Pt_1Ni_3, respectively. The Pt hexapod skeleton structure started to appear after increasing the reaction time to 2 hours. The hypothesis of such anisotropic growth is based on the preferred deposition at the corner sites of the nanocrystals. As shown in **Figure 5.7**, after 10 minutes of reaction, the major product was the Pt_8Ni_1 octahedra, which was enclosed with eight {111} facets

and six corners and served as the seed for further growth. In general, two reaction rates affect the directions of anisotropic growth, the deposition rate of adatoms ($R_{deposit}$), and the diffusion rate ($R_{diffuse}$) of Pt atoms from corner sites to facet sites. Because of the higher concentration gradient of adatoms at corner sites compared to that at facet sites, the adatoms tend to first deposit at the six corner sites, leading to overgrowth of Pt pods along the <100> directions from the corner sites. In the meantime, the Ni atoms tended to deposit at the concave {111} facet in the form of NiO to fulfill these concaved sites formed between three of the six pods, which prohibits the diffusion of Pt atoms from the corner to the {111} facets and ensures the continuous growth of Pt pods along <100> directions. A similar tendency of Ni deposition preference was also reported by Strasser at al. Only large Pt cuboctahedra and no Pt hexapod products were obtained without adding Ni(acac)$_2$, and no Pt octahedra were observed during the early growth stage, indicating that the NiO deposition is essential for preventing the Oswald ripening of Pt octahedra seed and induce the anisotropic growth along {111} direction.
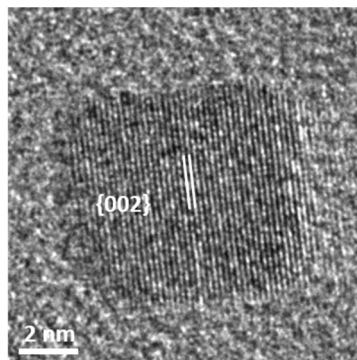

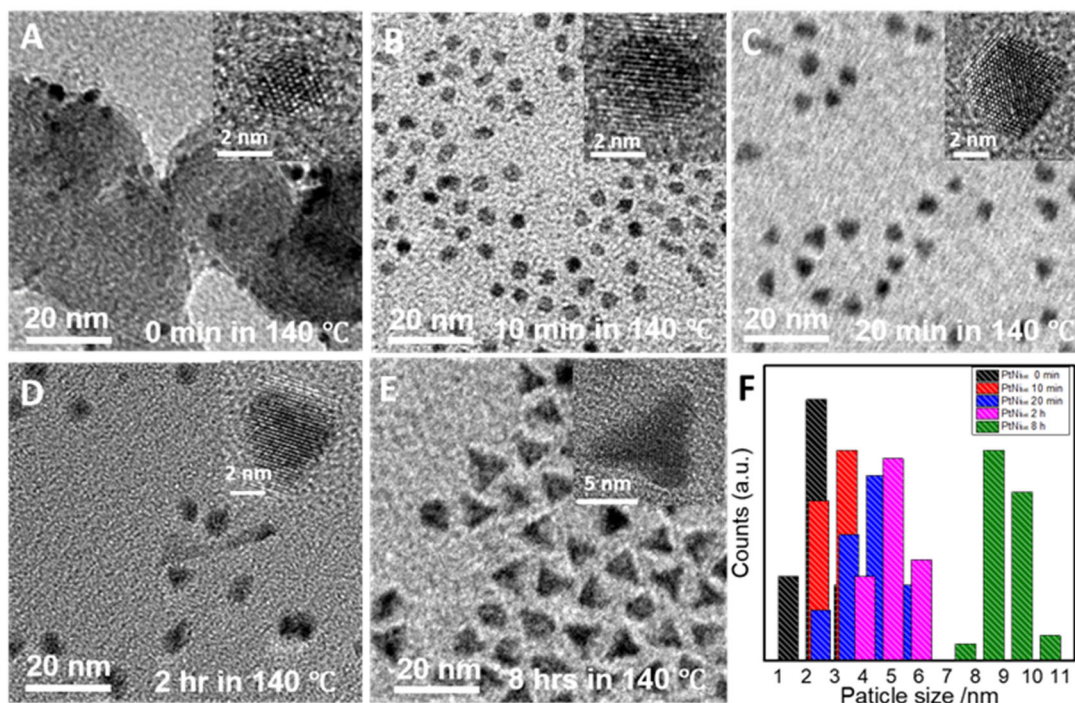**Figure 5.8**. Pt cube terminated with {100} facets.

Figure 5.9. (A) TEM image of Pt nucleates at 0 minutes reaction in 140 ℃, inset: representative HRTEM images of a typical cuboctahedron. (B) TEM image of larger cuboctahedron clusters after 5 min reaction in 140 ℃, inset: representative HRTEM images of a typical cuboctahedron shows the increased (111) facets and decreased (100) facts. (C) after 10 minutes, the Pt cuboctahedron has already evolved into Pt_9Ni_{1oct}. The Pt_9Ni_{1oct} gradually grows into (D) Pt_2Ni_{1oct} with 6-7 nm and (E) Pt_1Ni_{3oct} with 9-10 nm. (F) Size the evolution of the product during the reaction.

The case of $PtNi_{tet}$ is more complicated, because of its significantly slower growth rate, the final structure is under both kinetic and thermodynamic control. Without $Ni(acac)_2$, the Pt cubes enclosed with {100} facets became the major product, indicating that under slow reduction rate, the Pt deposition on the {111} facet is faster than the {100} facets (**Figure 5.8**). When the temperature reached 80 ℃, Pt clusters already formed because the glucose served as the reductant and help the nucleation of Pt. When the temperature increase to 140 ℃, however, the gluconic acid resulted from the oxidation of glucose inhibited the surface autocatalytic growth and leads to

the slow nucleation rate. **Thus, instead of Pt$_8$Ni$_1$ octahedra, the small Pt cluster only evolved into Pt$_9$Ni$_1$ cuboctahedra, a typical thermodynamic stable product that is enclosed with six {100} facets and eight {111} facets** (**Figure 5.8A**). Because the Pt deposition on the {111} facets is faster than the {100} facets, the eight {111} facts at the corner start to grow first. However, If all eight {111} facts start to overgrow, with the co-deposition of Ni on the {100} facets, the final structure should be the PtNi cube with octopod Pt-rich skeleton and Ni-rich cubic shell. Noticing that CO from W(CO)$_6$ can effectively stabilize the PtNi {111} facet, thus, the PtNi cubes with {100} facets exposed are not thermodynamically stable. The only left choice is the overgrow on four of the eight {111} facets with Td symmetry, which can deliver a tetrahedra shape with Pt tetrapod skeleton and four Ni-rich {111} facts (**Figure 5.9B-E**).
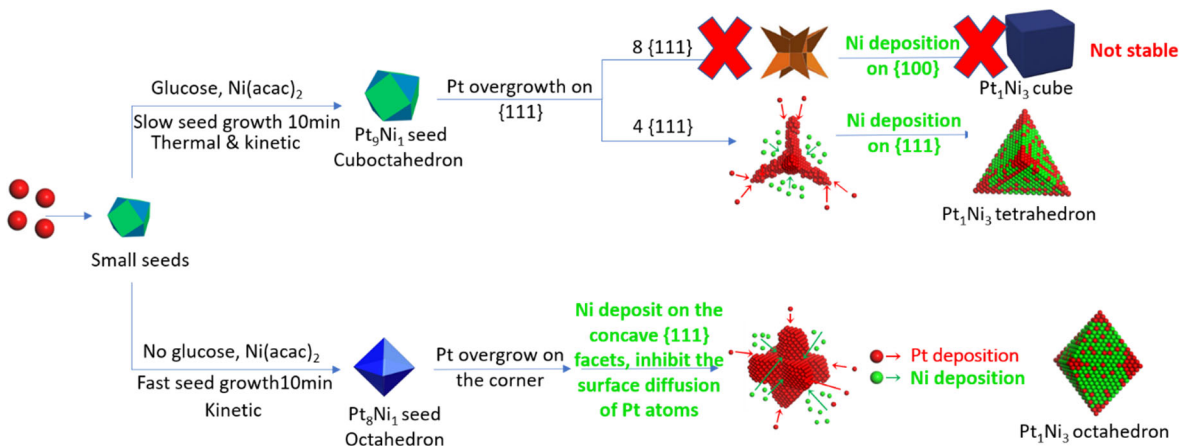
Figure 5.10. Illustration of the reaction mechanism.

5.4 Conclusion

In summary, the shape of the seeds, which determines the shape of the final product, is under the control of its growth rate at the early growth stage. Without glucose, the rapid growth of small cuboctahedra Pt cluster results in the diminish of Pt (100) facts of and deliver the kinetic controlled Pt$_8$Ni octahedra seeds. On the other hand, with glucose, the slow growth of small

cuboctahedra Pt clusters only results in a thermodynamic controlled Pt_9Ni cuboctahedra seed. The further overgrowth of Pt on the corner of Pt_8Ni octahedra seeds and the deposition of NiO on the {111} facets results in the Pt_1Ni_3 octahedra (**Figure 5.10**). And the further overgrowth of Pt on the {111} facets together with NiO deposition on the concave of Pt_9Ni cuboctahedra seed results in the final Pt_1Ni_3 tetrahedra. In the oleylamine system, the control of the growth rate could be achieved using organic molecules with a carboxylic group or ketone group that could be oxidized into the carboxylic group.

5.5 Reference

1   Huang, X., Zhao, Z., Cao, L., Chen, Y., Zhu, E., Lin, Z., Li, M., Yan, A., Zettl, A. & Wang, Y. M. High-performance transition metal–doped Pt3Ni octahedra for oxygen reduction reaction. *Science* **348**, 1230-1234 (2015).

2   Li, M., Zhao, Z., Cheng, T., Fortunelli, A., Chen, C.-Y., Yu, R., Zhang, Q., Gu, L., Merinov, B. V. & Lin, Z. Ultrafine jagged platinum nanowires enable ultrahigh mass activity for the oxygen reduction reaction. *Science* **354**, 1414-1419 (2016).

3   Chen, C., Kang, Y., Huo, Z., Zhu, Z., Huang, W., Xin, H. L., Snyder, J. D., Li, D., Herron, J. A., Mavrikakis, M., Chi, M., More, K. L., Li, Y., Markovic, N. M., Somorjai, G. A., Yang, P. & Stamenkovic, V. R. Highly crystalline multimetallic nanoframes with three-dimensional electrocatalytic surfaces. *Science* **343**, 1339-1343 (2014).

4   Cao, Z., Chen, Q., Zhang, J., Li, H., Jiang, Y., Shen, S., Fu, G., Lu, B.-a., Xie, Z. & Zheng, L. Platinum-nickel alloy excavated nano-multipods with hexagonal close-packed structure and superior activity towards hydrogen evolution reaction. *Nature communications* **8**, 15131 (2017).

5   Danilovic, N., Subbaraman, R., Strmcnik, D., Chang, K. C., Paulikas, A., Stamenkovic, V. & Markovic, N. M. Enhancing the alkaline hydrogen evolution reaction activity through the bifunctionality of Ni (OH) 2/metal catalysts. *Angewandte Chemie* **124**, 12663-12666 (2012).

6   Wang, P., Zhang, X., Zhang, J., Wan, S., Guo, S., Lu, G., Yao, J. & Huang, X. Precise tuning in platinum-nickel/nickel sulfide interface nanowires for synergistic hydrogen evolution catalysis. *Nature Communications* **8**, 14580 (2017).

7   Yin, H., Zhao, S., Zhao, K., Muqsit, A., Tang, H., Chang, L., Zhao, H., Gao, Y. & Tang, Z. Ultrathin platinum nanowires grown on single-layered nickel hydroxide with high hydrogen evolution activity. *Nature communications* **6**, 6430 (2015).

8   Zhao, Z., Liu, H., Gao, W., Xue, W., Liu, Z., Huang, J., Pan, X. & Huang, Y. Surface-engineered PtNi-O nanostructure with record-high performance for electrocatalytic hydrogen evolution reaction. *Journal of the American Chemical Society* **140**, 9046-9050 (2018).

9   Subbaraman, R., Tripkovic, D., Chang, K.-C., Strmcnik, D., Paulikas, A. P., Hirunsit, P., Chan, M., Greeley, J., Stamenkovic, V. & Markovic, N. M. Trends in activity for the water electrolyser reactions on 3d M (Ni, Co, Fe, Mn) hydr (oxy) oxide catalysts. *Nature materials* **11**, 550 (2012).

10   Liu, Z., Qi, J., Liu, M., Zhang, S., Fan, Q., Liu, H., Liu, K., Zheng, H., Yin, Y. & Gao, C. Aqueous Synthesis of Ultrathin Platinum/Non-Noble Metal Alloy Nanowires for Enhanced Hydrogen Evolution Activity. *Angewandte Chemie* **130**, 11852-11856 (2018).

11   Feng, Y.-Y., Bi, L.-X., Liu, Z.-H., Kong, D.-S. & Yu, Z.-Y. Significantly enhanced electrocatalytic activity for methanol electro-oxidation on Ag oxide-promoted PtAg/C catalysts in alkaline electrolyte. *Journal of catalysis* **290**, 18-25 (2012).

12   Fu, X.-Z., Liang, Y., Chen, S.-P., Lin, J.-D. & Liao, D.-W. Pt-rich shell coated Ni nanoparticles as catalysts for methanol electro-oxidation in alkaline media. *Catalysis Communications* **10**, 1893-1897 (2009).

13   Huang, W., Wang, H., Zhou, J., Wang, J., Duchesne, P. N., Muir, D., Zhang, P., Han, N., Zhao, F., Zeng, M., Zhong, J., Jin, C., Li, Y., Lee, S.-T. & Dai, H. Highly active and durable methanol oxidation electrocatalyst based on the synergy of platinum–nickel hydroxide–graphene. *Nature communications* **6**, 10035 (2015).

14   Jiang, Q., Jiang, L., Wang, S., Qi, J. & Sun, G. A highly active PtNi/C electrocatalyst for methanol electro-oxidation in alkaline media. *Catalysis Communications* **12**, 67-70 (2010).

15   Ren, F., Wang, C., Zhai, C., Jiang, F., Yue, R., Du, Y., Yang, P. & Xu, J. One-pot synthesis of a RGO-supported ultrafine ternary PtAuRu catalyst with high electrocatalytic activity towards methanol oxidation in alkaline medium. *Journal of Materials Chemistry A* **1**, 7255-7261 (2013).

16   Chen, M., Cai, Y., Yan, Z., Gath, K., Axnanda, S. & Goodman, D. W. Highly active surfaces for CO oxidation on Rh, Pd, and Pt. *Surface Science* **601**, 5326-5331 (2007).

17   Ko, E. Y., Park, E. D., Lee, H. C., Lee, D. & Kim, S. Supported Pt–Co Catalysts for Selective CO Oxidation in a Hydrogen-Rich Stream. *Angewandte Chemie International Edition* **46**, 734-737 (2007).

18   Qiao, B., Wang, A., Yang, X., Allard, L. F., Jiang, Z., Cui, Y., Liu, J., Li, J. & Zhang, T. Single-atom catalysis of CO oxidation using Pt 1/FeO x. *Nature chemistry* **3**, 634 (2011).

19   Wu, Y., Cai, S., Wang, D., He, W. & Li, Y. Syntheses of water-soluble octahedral, truncated octahedral, and cubic Pt–Ni nanocrystals and their structure–activity study in model hydrogenation reactions. *Journal of the American Chemical Society* **134**, 8975-8981 (2012).

20   Debe, M. K. Electrocatalyst approaches and challenges for automotive fuel cells. *Nature* **486**, 43 (2012).

21   Cui, C., Gan, L., Li, H.-H., Yu, S.-H., Heggen, M. & Strasser, P. Octahedral PtNi nanoparticle catalysts: exceptional oxygen reduction activity by tuning the alloy particle surface composition. *Nano letters* **12**, 5885-5889 (2012).

22   Cui, C., Gan, L., Heggen, M., Rudi, S. & Strasser, P. Compositional segregation in shaped Pt alloy nanoparticles and their structural behaviour during electrocatalysis. *Nature materials* **12**, 765 (2013).

23   Wang, P., Jiang, K., Wang, G., Yao, J. & Huang, X. Phase and interface engineering of platinum–nickel nanowires for efficient electrochemical hydrogen evolution. *Angewandte Chemie International Edition* **55**, 12859-12863 (2016).

24   Xie, Y., Cai, J., Wu, Y., Zang, Y., Zheng, X., Ye, J., Cui, P., Niu, S., Liu, Y., Zhu, J., Liu, X., Wang, G. & Qian, Y. Boosting Water Dissociation Kinetics on Pt–Ni Nanowires by N-Induced Orbital Tuning. *Advanced Materials*, 1807780 (2019).

25   Wu, J., Gross, A. & Yang, H. Shape and composition-controlled platinum alloy nanocrystals using carbon monoxide as reducing agent. *Nano letters* **11**, 798-802 (2011).

26   Stamenkovic, V. R., Fowler, B., Mun, B. S., Wang, G., Ross, P. N., Lucas, C. A. & Marković, N. M. Improved oxygen reduction activity on Pt3Ni (111) via increased surface site availability. *Science* **315**, 493-497 (2007).

27   Xia, Y., Xiong, Y., Lim, B. & Skrabalak, S. E. Shape-controlled synthesis of metal nanocrystals: simple chemistry meets complex physics? *Angewandte Chemie International Edition* **48**, 60-103 (2009).

28   Qian, J., Shen, M., Zhou, S., Lee, C.-T., Zhao, M., Lyu, Z., Hood, Z. D., Vara, M., Gilroy, K. D., Wang, K. & Xia, Y. Synthesis of Pt nanocrystals with different shapes using the same protocol to optimize their catalytic activity toward oxygen reduction. *Materials Today* **21**, 834-844 (2018).

29   Yin, X., Shi, M., Wu, J., Pan, Y.-T., Gray, D. L., Bertke, J. A. & Yang, H. Quantitative Analysis of Different Formation Modes of Platinum Nanocrystals Controlled by Ligand Chemistry. *Nano Letters* **17**, 6146-6150 (2017).

CHAPTER 6. CONCLUSION

In conclusion, the specific activity and the electrochemical active surface area (ECSA) of Pt-based nanostructures towards electrocatalytic reactions can be simultaneously enhanced via surface and interface engineering strategies such as tailoring surface with single-atom promotors and electrolyte permeable shells. We can control surface oxophilicity of Pt surface to facilitate the adsorption/desorption of desired intermediates in the rate-determining step and hence accelerate the final reaction rate.

In our first work, we used a controllable dealloy strategy to achieve the single-atom Ni species tailored Pt nanowires (SANi-PtNWs). The single-atom nature and chemical state of Ni species were further confirmed by EELS spectra, Electron energy loss spectroscopy (EELS). X-ray photoelectron spectroscopy (XPS), and extended X-ray absorption fine structure (EXAFS). Compared with the commercial Pt/C, the SANi-PtNWs exhibit 17 times higher HER mass activity at -0.07 V vs. RHE in 1 M KOH. Density functional theory (DFT) calculations reveal that all Pt atoms around SANi show a reduced hydrogen binding energy and are optimal for HER. We further show that such single atomic modification also greatly enhances the catalytic activity for both MOR and EOR to deliver a mass activity of 7.93 ± 0.45 A/mg$_{Pt}$ and 5.60 ± 0.27 A/mg$_{Pt}$, respectively. These studies demonstrate that the single-atom tailoring approach offers a general strategy for creating highly efficient electrocatalysts for diverse reactions.

In our second work, using the direct synthesis methods, we extend SANi-PtNWs to the SARh-PtNWs. It was revealed by the *in-situ* EXAFS and XANES that the single Rh atoms under 0 V vs. RHE are slightly positively charged and bonded with eight Pt atoms and one OH$_{ads}$/H$_2$O$_\downarrow$. The existence of single-atom Rh-OH$_{ads}$/H$_2$O$_\downarrow$. Under 0 V significantly facilitates the sluggish

Volmer step at the minimal sacrifice of the active Pt sites where H_2 dissociation and H adsorption takes place. By controlling the surface Rh concentration, we found that the HOR activity achieves the maximum value only when the Rh is in the form of a single-atom on the Pt surface and the surface oxophilicity reaches an optimum value, neither too strong nor too weak for adsorption of $OH_{ads}/H_2O_\downarrow$. This supports the bifunctional theory of HOR in alkaline condition and addresses the significance of surface oxophilicity engineering in enhancing HOR under high pH.

In our third work, we have developed a novel synthetic strategy to prepare electrolyte permeable $Ni(OH)_2$ shell on the Pt-tetrapod framework ($Pt_{tet}@Ni(OH)_2$ core-shell framework) to enhance the HER specific activity while maintaining the ECSA to deliver the highest HER mass activity so far ($13.4 \pm 2.8\%$ A/mg$_{Pt}$ and SA of (27.7 mA/cm$^2_{Pt}$), which is 17.8-fold and 28-fold higher than that of the commercial Pt/C).

In the fourth work, we report a facile and tunable synthesis of PtNi tetrahedron and octahedron. We have found that the shape of PtNi nanocrystals is determined by the growth rate of the Pt seeds and the further anisotropic growth on the Pt seeds. The slow nucleation rate leads to thermodynamic stable cuboctahedra seeds on which the further Pt deposition on the four of the eight {111} facets and NiO deposition on concave structure enclosed by the Pt pods along the <111 > direction deliver the final PtNi tetrahedra. On the other hand, the rapid nucleation leads to kinetics controlled octahedra seed and the further overgrowth of Pt on the six corners deliver the final PtNi octahedra.